A&A 615, A8 (2018)
https://doi.org/10.1051/0004-6361/201732470

Astronomy & Astrophysics

Circumstellar environment of the M-type AGB star R Doradus

APEX spectral scan at 159.0–368.5 GHz★, ★★

E. De Beck and H. Olofsson

Department of Space, Earth and Environment, Chalmers University of Technology, Onsala Space Observatory, 43992 Onsala, Sweden
e-mail: elvire.debeck@chalmers.se

Received 15 December 2017 / Accepted 17 January 2018

ABSTRACT

Context. Our current insights into the circumstellar chemistry of asymptotic giant branch (AGB) stars are largely based on studies of carbon-rich stars and stars with high mass-loss rates.
Aims. In order to expand the current molecular inventory of evolved stars we present a spectral scan of the nearby, oxygen-rich star R Dor, a star with a low mass-loss rate ($\sim 2 \times 10^{-7}\ M_{\odot}\ \mathrm{yr}^{-1}$).
Methods. We carried out a spectral scan in the frequency ranges 159.0–321.5 GHz and 338.5–368.5 GHz (wavelength range 0.8–1.9 mm) using the SEPIA/Band-5 and SHeFI instruments on the APEX telescope and we compare it to previous surveys, including one of the oxygen-rich AGB star IK Tau, which has a high mass-loss rate ($\sim 5 \times 10^{-6}\ M_{\odot}\ \mathrm{yr}^{-1}$).
Results. The spectrum of R Dor is dominated by emission lines of SO_2 and the different isotopologues of SiO. We also detect CO, H_2O, HCN, CN, PO, PN, SO, and tentatively TiO_2, AlO, and NaCl. Sixteen out of approximately 320 spectral features remain unidentified. Among these is a strong but previously unknown maser at 354.2 GHz, which we suggest could pertain to H_2SiO, silanone. With the exception of one, none of these unidentified lines are found in a similarly sensitive survey of IK Tau performed with the IRAM 30 m telescope. We present radiative transfer models for five isotopologues of SiO (^{28}SiO, ^{29}SiO, ^{30}SiO, Si^{17}O, Si^{18}O), providing constraints on their fractional abundance and radial extent. We derive isotopic ratios for C, O, Si, and S and estimate that, based on our results for ^{17}O/^{18}O, R Dor likely had an initial mass in the range 1.3–1.6 $M_{\odot}$, in agreement with earlier findings based on models of H_2O line emission. From the presence of spectral features recurring in many of the measured thermal and maser emission lines we tentatively identify up to five kinematical components in the outflow of R Dor, indicating deviations from a smooth, spherical wind.

Key words. stars: AGB and post-AGB – stars: individual: R Dor – stars: mass-loss – astrochemistry

1. Introduction

In order to get a comprehensive view of the physical and chemical properties of the circumstellar envelopes (CSEs) of asymptotic giant branch (AGB) stars and to quantify their return to the interstellar medium, it is necessary to characterise the gas and dust contents of these outflows. The set-up of an inventory of chemical species present in the CSEs of evolved stars has predominantly used, as reference, the nearby, high-mass-loss-rate, carbon-rich AGB star IRC + 10 216 (also commonly referred to as CW Leo), skewing the community's knowledge towards the carbon-rich chemistry, both observationally and theoretically. A similar wealth of observational constraints on the circumstellar chemistry of M-type AGB stars, often called oxygen-rich given their atmospheric C/O < 1, is currently still lacking.

Unbiased spectral surveys, scanning broad frequency ranges without pre-selecting particular molecules of interest, are excellent tools to set up such inventories. Several such surveys using single-dish telescopes have been presented for high-mass-loss-rate, carbon-rich AGB stars: IRC + 10 216 (Cernicharo et al. 2000, 2010), CIT 6 (RW LMi; Zhang et al. 2009a), and CRL 3068 (LL Peg; Zhang et al. 2009b). Patel et al. (2011) presented an interferometric survey of IRC + 10 216 obtained with the Submillimeter Array (SMA). Kamiński et al. (2013b) reported on a similar SMA line-imaging survey of the red supergiant VY CMa, a star with an oxygen-rich composition, an extremely high mass-loss rate of several $10^{-4}\ M_{\odot}\ \mathrm{yr}^{-1}$, and a geometrically and chemically complex CSE (e.g. Humphreys et al. 2007; Richards et al. 2014; Ziurys et al. 2007). De Beck et al. (2015a) presented an overview of an interferometric spectral survey of the Mira-type (SEPIA; Billade et al. 2012; Belitsky et al. 2018), high-mass-loss-rate, M-type star IK Tau in the range 279–355 GHz carried out with the SMA. A forthcoming publication (De Beck et al., in prep.) will report on this survey in its entirety, including a discussion on the extent and geometry of the imaged line emission. Based partially on this survey, De Beck et al. (2013) presented first results on phosphorus-bearing molecules in the CSE of an M-type AGB star and highlighted the need for updated chemical models for these CSEs. Velilla Prieto et al. (2017) recently presented a spectral scan of IK Tau obtained with the IRAM 30 m telescope covering the ranges 79–116, 128–175, and 202–356 GHz. They reported a very rich chemical content, including several carbon-bearing molecules, such as H_2CO and HCO^+, and several nitrogen-bearing molecules, such as NS and

★ This publication is based on data acquired with the Atacama Pathfinder Experiment (APEX). APEX is a collaboration between the Max-Planck-Institut für Radioastronomie, the European Southern Observatory, and the Onsala Space Observatory.
★★ The full APEX spectrum of R Doradus is only available at the CDS via anonymous ftp to cdsarc.u-strasbg.fr (130.79.128.5) or via http://cdsarc.u-strasbg.fr/viz-bin/qcat?J/A+A/615/A8

NO. The abundances they derive for several of the detected species further underscore the need for improved models of the chemistry around oxygen-rich stars.

We present here for the first time a spectral scan of a low-mass-loss-rate M-type AGB star, R Dor, enabling a direct comparison of the chemical contents of CSEs representative of two significantly different density regimes. R Dor is a nearby (59 pc; Knapp et al. 2003) AGB star with a luminosity of about 6500 $L_{\odot}$ (Maercker et al. 2016). It shows a semi-regular pulsation pattern with two periods of 175 and 332 days, respectively (Bedding & Zijlstra 1998). Studies of its circumstellar environment have mainly focussed on CO and H_2O line emission (e.g. Ramstedt & Olofsson 2014; Maercker et al. 2016), constraining its mass-loss rate to 1–2 $\times 10^{-7}$ $M_{\odot}$ yr^{-1}. Recently, Van de Sande et al. (2018) reported on a detailed abundance analysis of SiO and HCN.

We list the details of the observations in Sect. 2, present and discuss the results in Sect. 3, and provide a list of unidentified spectral features in Sect. 3.4. We compare our results to those obtained from other line surveys, in particular of IK Tau, in Sect. 4, discuss possible deviations in the outflow from spherical symmetry in Sect. 5, and present our conclusions in Sect. 6. Appendix A addresses possible time variability of the CO line emission. Appendix B addresses maser line variability and includes a list of detected masers. Appendix C provides an overview of the full survey.

2. Observations

We used the Swedish Heterodyne Facility Instrument (SHeFI; Vassilev et al. 2008) and band 5 of the Swedish-ESO PI Instrument (SEPIA; Billade et al. 2012) on the Atacama Pathfinder Experiment (APEX) telescope to carry out a spectral survey covering the frequency range 159.0–368.5 GHz. Due to excessive interference of water vapour in the atmosphere the survey does not cover the range 321.5–328.0 GHz. The SHeFI observations were carried out over a long period, spanning from May 2011 up to November 2015. All SEPIA observations were carried out on 22 and 23 November 2015.

SHeFI is a single-sideband (sideband-separating), single-polarisation heterodyne receiver, whereas SEPIA is a sideband-separating, dual-polarisation heterodyne receiver. The backends for SHeFI changed during the observing campaign and were extended from an initial 2 × 1.0 GHz bandwidth (FFTS) to 2 × 2.5 GHz (XFFTS), corresponding to instantaneous bandwidths of 1.9 and 4.0 GHz, respectively, significantly increasing the observing efficiency. The SEPIA backends consist of 2 × 2 × 2 × 2.5 GHz, covering both lower and upper sidebands simultaneously, in two polarisations. The SHeFI spectra were recorded at a nominal resolution of 122 kHz when the FFTS was used, and at 76 kHz when the XFFTS was used. The SEPIA spectra were recorded at 38 kHz nominal resolution. Consecutive tunings were separated by 1.5 GHz or 3.5 GHz, depending on the backend in use, to ensure sufficient overlap.

The observations were carried out using wobbler switching with a standard beam throw of 50″. Due to some technical issues with the wobbler, some settings were observed in position switching mode, without compromising the final result. The main beam half power beamwidth of APEX varies in the range 17–39″ over the observed frequency range.

Data reduction is done using the GILDAS/CLASS[1] package. We inspect scans individually and ignore those with very unstable baselines. Bad channels, which commonly appear in the outer 30–50 MHz of the band[2] are blanked. We subtract first-degree polynomial baselines from the individual scans, after masking relevant spectral features, and combine all data into one final spectrum.

In a few cases, we find aliases of strong lines of CO and SiO, in the outer ~60 MHz of the receiver backend. These can occur when the strong signal is very close to the edge of the XXFTS unit and gets folded into the band. Given the proximity to the band edge, and the overlapping observing settings, these aliases are removed from the spectra without losing spectral coverage.

The SHeFI receivers on APEX work in single-sideband mode with reported image-sideband suppression of typically >15 dB. The sideband-separating SEPIA instrument has an average image-sideband suppression of 18.5 dB. Some strong lines can, therefore, leak into the one sideband from the other for some frequency settings. In case there is no overlapping spectral coverage from another frequency tuning available, we do not blank these lines in our spectrum, but clearly mark these leakages in the overview tables and plots. The leakage levels in our survey range from 0.3% (25 dB suppression of an 11 K strong signal) up to 54% (3 dB) in the most extreme case, but are overall well in line with the reported suppression values.

We assume overall calibration uncertainties of 20% on the survey data, but argue in Sect. 3.2.2 that the internal uncertainties, that is, line-to-line uncertainties, are most likely lower than that.

Unless stated otherwise, we show all spectra in $T_{\rm A}^*$, that is, the antenna temperature scale corrected for atmospheric losses and, for example, antenna spillover. Typical rms noise values on this scale vary from 3 to 10 mK at 2 km s^{-1} resolution, with higher rms locally induced by the interference of atmospheric H_2O at 183 and 321 GHz. For conversion into flux units one can employ point-source sensitivities $S_\nu/T_{\rm A}^*$ of 38, 39, and 41 Jy K^{-1} for the SEPIA/band-5 (159–211 GHz), SHeFI-1 (213–275 GHz), and SHeFI-2 (267–378 GHz) observations, respectively. Conversion to main-beam brightness temperature, $T_{\rm mb} = T_{\rm A}^*/\eta_{\rm mb}$, used in this work for comparison to modelling results, uses main-beam efficiencies $\eta_{\rm mb}$ of 0.68, 0.75, and 0.73 for the different bands, respectively. The values for SEPIA/band-5 are preliminary, but currently the most up-to-date (Immer et al. 2016).

We claim detection of a spectral feature at signal-to-noise ratios (S/Ns) of at least 3 at a spectral resolution that leaves a minimum of five spectral bins covering the line. Additionally, tentative detections of lines at low S/N can be claimed in the case where a stacked spectrum reaches this S/N criterion (e.g. for PN, see below) or if one, or more, other emission lines of the same molecule are present elsewhere in the spectrum.

3. Results

Figure 1 shows a low-resolution overview of the APEX line survey of R Dor. Figure C.1 in the Appendix shows the entire survey at 3 MHz frequency resolution. Table C.1 gives an overview of all emission features in the scan, while Table 1 gives an overview of the identified lines per molecule. The spectrum is dominated by emission lines of SO_2 (134 lines), SiO (50 lines), and SO (28 lines), including isotopologues.

For line identification we use the Cologne Database for Molecular Spectroscopy[3] (CDMS; Müller et al. 2001, 2005) and the catalogue[4] for molecular line spectroscopy hosted by the Jet

[1] http://www.iram.fr/IRAMFR/GILDAS/

[2] http://www.apex-telescope.org/backends/ffts/

[3] https://www.astro.uni-koeln.de/cdms/

[4] http://spec.jpl.nasa.gov/

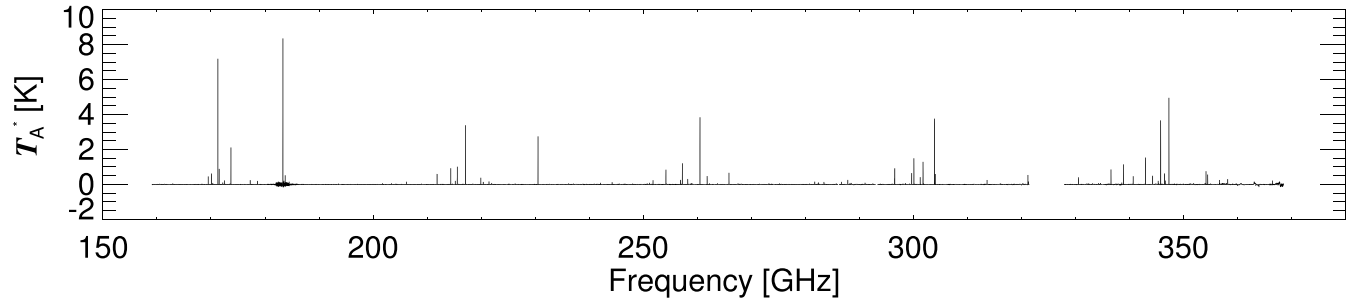

Fig. 1. APEX survey of R Dor in the range 159.0–368.5 GHz.

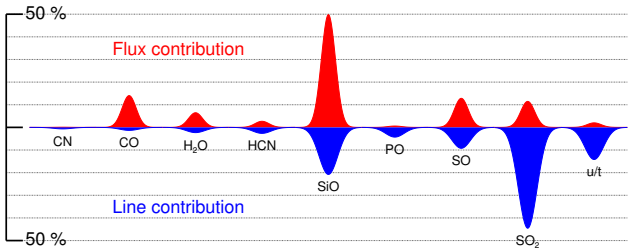

Fig. 2. Overview of the relative contribution per molecule (including isotopologues) to the survey in terms of flux (*top*) and number of lines (*bottom*). Unidentified and tentatively identified spectral features are grouped under the label "u/t".

Propulsion Laboratory (JPL; Pickett et al. 1998) as primary reference catalogues, with priority given to CDMS when entries are present in both.

3.1. Molecular line luminosity

The molecular line emission observed in the survey is dominated by only a few molecules. Approximately 50% of the total line flux comes from SiO and its isotopologues, which accounts for 21% of the emission features. Another 14% of the flux comes from the four (1.3%) CO lines. SO accounts for 13% of the flux and 9% of the lines. SO_2 accounts for another 12% of the flux and 45% of the lines. H_2O accounts for 6% of the flux and 2% of the lines. Other species each contribute less than 3% of the total flux. Figure 2 presents a visual summary of this.

3.2. Molecular species

Throughout the paper, we assume that the source's systemic velocity, v_{LSR}, is 6.5 km s^{-1}, and plot profiles with respect to the stellar v_{LSR}, that is, centered around 0.0 km s^{-1}. This value for the systemic velocity corresponds to individual peaks in, for example, the CO lines, the 321 GHz H_2O maser, and many of the SO_2 lines already presented by Danilovich et al. (2016). It also matches the central depression in the 183 GHz H_2O maser and appears appropriate based on, for example, the selection of emission features pertaining to different molecules and spanning a large range of excitation conditions as discussed in Sect. 5. Finally, it is also in agreement with the radiative-transfer modelling efforts from earlier publications (e.g. Maercker et al. 2016).

3.2.1. Carbon monoxide

The estimated radial extent of the CO envelope of R Dor, that is, the *e*-folding radius of the CO abundance profile, is

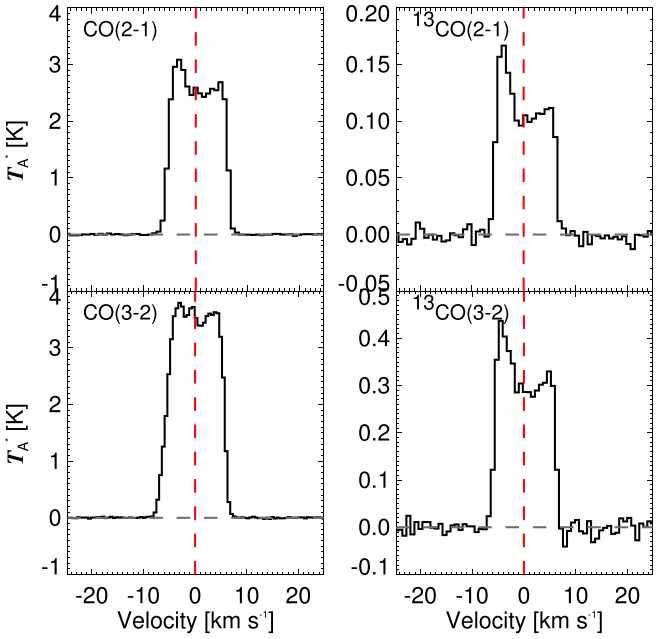

Fig. 3. CO line emission. *Left*: ^{12}CO; *right*: ^{13}CO.

1.6×10^{16} cm, corresponding to an angular (diametric) size of 36″ at a distance of 59 pc (Maercker et al. 2016). The ^{12}CO and ^{13}CO emission lines measured towards R Dor in this survey are hence slightly spatially resolved (see e.g. Fig. 21) and the spectra do not recover all of the emission as these are single-pointing observations. On the contrary, for all the other molecular line emissions the loss of flux is estimated to be small.

Our observations of the ^{12}CO(J=2–1, 3–2) and ^{13}CO(J=2–1, 3–2) line emission (Fig. 3) agree within 15% (in intensity) with the independently performed APEX observations of Ramstedt & Olofsson (2014). We discuss possible variability over time of the CO line emission in Appemdix A. We refer to Ramstedt & Olofsson (2014) and Maercker et al. (2016) for detailed radiative transfer models of CO.

3.2.2. Silicon monoxide

We detect 50 transitions of SiO and its isotopologues. Figures 4–8 show the spectra for the transitions J=4–3, ..., 9–8 in the vibrational states v=0, ..., 5 for the isotopologues ^{28}SiO, ^{29}SiO, ^{30}SiO, Si^{17}O, and Si^{18}O. The intensity-weighted mean velocity of the lines (in v = 0) of the different isotopologues shifts slightly to the red with increasing J. This could be explained by an increasing optical thickness that causes stronger self-absorption

Table 1. Overview of molecules in the APEX survey of R Dor.

Molecule	Number of lines	Line numbers
CN	2	268, 270
CO	2	86, 289
^{13}CO	2	80, 243
H_2O	2	37, 239
H_2O, $v_2 = 1$	5	87, 141, 192, 202, 256
H_2O, $v_2 = 2$	1	149
HCN	3	34, 144, 303
H^{13}CN	3	27, 134, 286
PO	12	48, 49, 50, 51, 94, 95, 96, 97, 173, 174, 175, 176
SiO	5	29, 78, 136, 220, 295
SiO, $v = 1$	5	26, 75, 132, 216, 284
SiO, $v = 2$	3	22, 127, 212
SiO, $v = 3$	4	20, 68, 203, 269
SiO, $v = 5$	1	115
^{29}SiO	5	23, 71, 129, 213, 280
^{29}SiO, $v = 1$	4	21, 123, 205, 272
^{29}SiO, $v = 2$	2	120, 262
^{29}SiO, $v = 3$	2	193, 254
^{30}SiO	5	19, 67, 121, 200, 265
^{30}SiO, $v = 1$	3	18, 118, 257
Si^{17}O	5	16, 65, 112, 190, 251
Si^{18}O	5	5, 56, 100, 169, 331
^{29}Si^{18}O	1	161
SO	16	25, 36, 63, 74, 79, 117, 130, 138, 199, 215, 221, 226, 266, 273, 281, 293
^{34}SO	12	32, 57, 76, 108, 119, 126, 195, 206, 250, 260, 267, 306
SO_2	116	1, 4, 9, 11, 13, 14, 31, 43, 45, 46, 47, 52, 54, 55, 58, 60, 61, 64, 69, 72, 77, 81, 82, 83, 85, 88, 90, 91, 92, 98, 99, 102, 105, 106, 109, 111, 113, 114, 122, 124, 125, 128, 131, 133, 135, 140, 142, 145, 146, 152, 157, 158, 163, 164, 165, 167, 168, 171, 179, 186, 197, 198, 208, 211, 214, 217, 223, 227, 228, 229, 230, 231, 235, 236, 240, 244, 248, 252, 255, 258, 263, 264, 271, 274, 275, 276, 277, 279, 285, 292, 294, 296, 298, 299, 304, 305, 309, 311, 312, 313, 315, 316, 317, 318, 319, 320, 321, 323, 325, 327, 328, 329, 332, 333, 334, 336
SO_2, $v_2 = 1$	1	297
$^{34}SO_2$	5	7, 30, 104, 310, 330
SO^{17}O	2	233, 290
SO^{18}O	9	177, 178, 183, 184, 185, 218, 219, 283, 291
u	16	28, 44, 59, 84, 148, 156, 162, 172, 196, 201, 207, 225, 234, 237, 245, 302

Notes. The columns list the molecule (vibrational states and isotopologues are listed separately), the number of lines per species, and the line numbers from Table C.1 corresponding to the identified lines. Tentative identifications (e.g. of PN and TiO_2) and features resulting from data issues or image contamination are not listed in this table.

in the blue wing with increasing J, shifting the peak of the emission redwards. This effect is reproduced by our radiative transfer models discussed below.

Emission in transitions in the vibrational ground state ($v = 0$) is most often assumed to be of non-maser nature. However, recently, de Vicente et al. (2016) showed that the SiO($v = 0$, $J = 1$–0) transition exhibits clear (and variable) signatures of maser nature in many of the oxygen-rich and S-type AGB stars in their sample. These maser components are thought to be excited in the very inner layers of the CSE, where no dust is present yet. de Vicente et al. (2016) further state that higher-J transitions are typically of thermal nature. We note, however, that time-variable features are occasionally seen in the $J = 2$–1 emission and that these are likely of maser nature, see Nyman & Olofsson (1985). Judging from the appearance of the emission features in this survey and in the HIFI data (Fig. 3; $J = 4$–3 and higher) thermal excitation indeed seems to be likely for the observed $v = 0$ lines.

For vibrationally excited states ($v \neq 0$) the emission is clearly of maser nature, often with multiple peaks in the line profiles. These complex shapes are furthermore not constant across the excitation ladder within one vibrational state. We plot a selection of the highest-S/N maser lines of SiO (any isotopologue) in Fig. 22. As discussed in Sect. 5, several of the individual maser peaks correspond to the velocities where peaks or bumps also appear in thermal emission lines. Overall, it is clear that the SiO maser emission can differ substantially between different transitions, even within the same vibrationally excited state of a given isotopologue. Some maser lines are composed of several peaks over the entire velocity range (e.g. ^{28}SiO($v = 1$, $J = 4$–3)), some are limited to only blue or red-shifted velocities (e.g. ^{28}SiO($v = 3$, $J = 4$–3) and ^{28}SiO($v = 2$, $J = 7$–6)), and some appear as very broad emission lines with barely discernible maser components (e.g. ^{28}SiO($v = 1$, $J = 7$–6)). This is in line with both observations and simulations of SiO masers in the CSEs of red

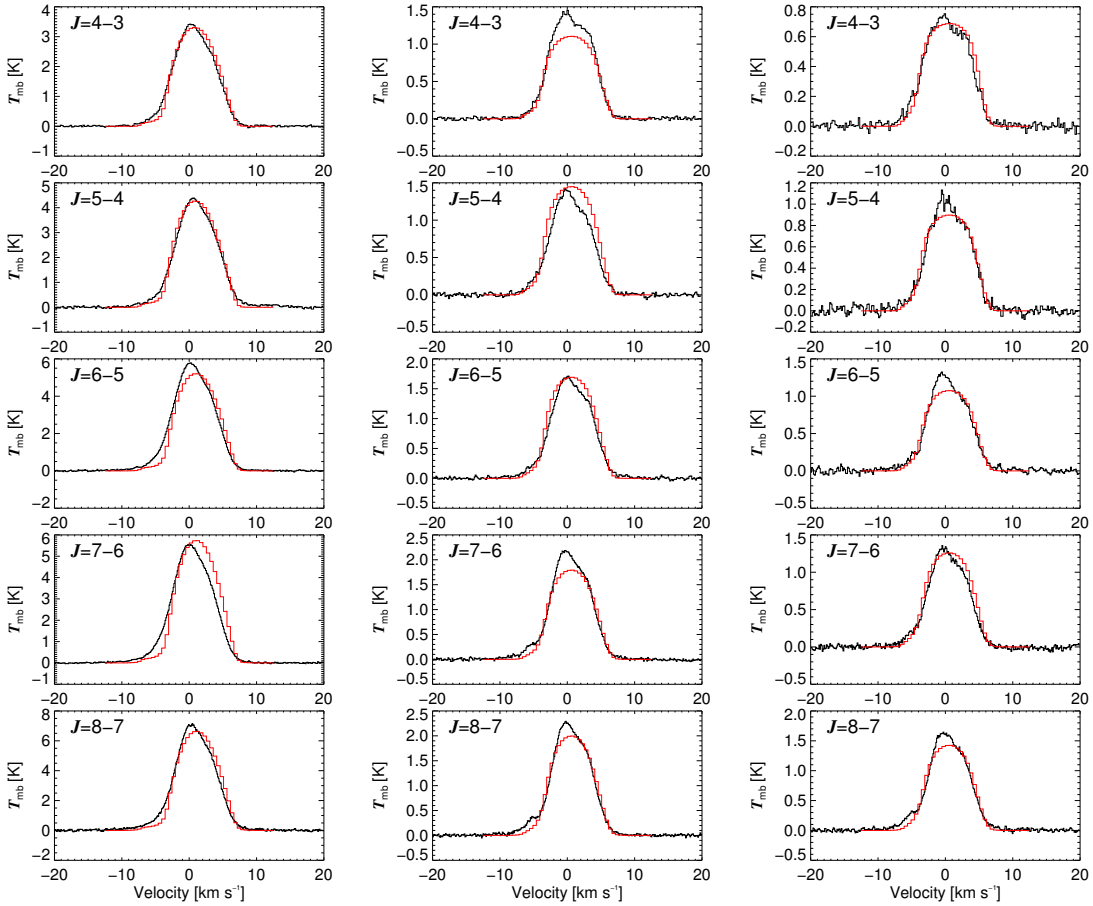

(a) $^{28}Si^{16}O$ (b) $^{29}Si^{16}O$ (c) $^{30}Si^{16}O$

Fig. 4. SiO isotopologue ($^{28,29,30}Si^{16}O$) $v = 0$ line emission (black) and the predictions from our best-fit radiative transfer models (red). We note that the line intensity is given as main-beam brightness temperature T_{mb}.

Table 2. Radiative transfer modelling results for SiO isotopologues.

Isotopologue	$\log(f_0)$			$\log(R_e$[cm])		
	Grid range (step)	Best-fit value	1σ-range	Grid range (step)	Best-fit value	1σ-range
$^{28}Si^{16}O$	[−5.5, −4.0] (0.1)	−4.7	[−5.2, −4.0]	[15.00, 16.20] (0.15)	15.60	[15.15, 16.20]
$^{29}Si^{16}O$	[−6.8, −5.3] (0.1)	−5.8	[−5.9, −5.4]	[15.00, 16.20] (0.15)	15.90	[15.30, 16.20]
$^{30}Si^{16}O$	[−6.8, −5.3] (0.1)	−6.0	[−6.2, −5.5]	[15.00, 16.20] (0.15)	15.75	[15.15, 16.20]
$^{28}Si^{17}O$	[−8.5, −7.0] (0.1)	−7.3	[−7.5, −7.1]	[15.00, 16.20] (0.15)	15.45	[15.15, 15.90]
$^{28}Si^{18}O$	[−8.0, −6.5] (0.1)	−7.1	[−7.2, −7.0]	[15.00, 16.20] (0.15)	15.60	[15.45, 16.20]

giant and supergiant stars (e.g. Humphreys et al. 1997, 2002; Desmurs et al. 2014), from which it is apparent that the excitation of different rotational transitions within the same vibrational state is not necessarily co-spatial. This, in combination with non-simultaneity of the observations, explains the variety in the profiles we observe towards R Dor. We therefore add Table B.1 listing the observing dates of these lines in Appendix B.

The wealth of emission lines from different SiO isotopologues, spanning the entire frequency range of the survey, motivates a deeper investigation through modelling. We base the radiative transfer modelling of the SiO $v = 0$ line emission on the CSE model reported by Maercker et al. (2016). Our molecular input covers the rotational levels for $J = 0, \ldots, 40$ of the $v = 0, 1$ states of ^{28}SiO, ^{29}SiO, ^{30}SiO, Si^{17}O, and Si^{18}O. Collisional rates are included for SiO–H_2, adapted from the collisional rates for SiO–He of Dayou & Balança (2006). The modelling is performed using the accelerated lambda iteration (ALI) radiative transfer code described and implemented by Maercker et al. (2008, 2016), and Danilovich et al. (2014).

We assume a centrally peaked Gaussian fractional abundance distribution

$$f(r) = f_0 \exp\left(-\left(\frac{r}{R_e}\right)^2\right), \quad (1)$$

with f_0 the molecular abundance (w.r.t. H_2) at the inner radius of the CSE (at $5\,R_\star$, following Danilovich et al. 2016), also referred to as peak abundance in the rest of the paper, and R_e the e-folding

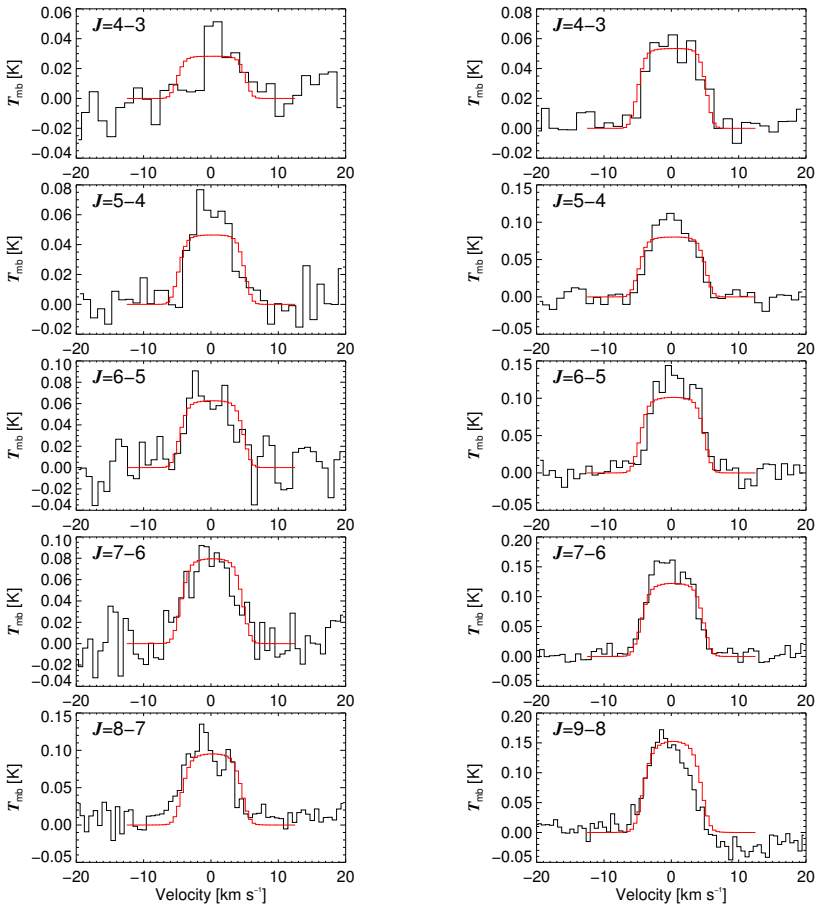

(a) ^{28}Si^{17}O (b) ^{28}Si^{18}O

Fig. 5. SiO isotopologue (^{28}Si^{17,18}O) $v = 0$ line emission (black) and the predictions from our best-fit radiative transfer models (red). We note that the line intensity is given as main-beam brightness temperature $T_{\rm MB}$.

radius of the Gaussian profile. We set up a model grid for these two free parameters, f_0 and R_e, as summarised in Table 2. We minimise the reduced-χ^2

$$\chi^2_{\rm red} = \frac{1}{N-p}\sum_{i=1}^{N}\left(\frac{I_{\rm mod}-I_{\rm obs}}{\sigma}\right)^2, \quad (2)$$

with N being the number of modelled transitions (five for each isotopologue), p the number of free parameters (two), $I_{\rm mod}$ and $I_{\rm obs}$ the modelled and observed integrated line intensities, respectively, and σ the uncertainty on $I_{\rm obs}$. We assume uncertainties on the data at a 20% level, accounting for predominantly the calibration uncertainties, given the high S/Ns in the modelled lines. Table 2 lists the best-fit values of f_0 and R_e with their 1σ-uncertainties for each of the isotopologues. We show the reduced-χ^2 maps in Fig. 9 and the comparison of the best-fit models to the survey data in Figs. 4 and 5. In general, we find that there is a rather large degeneracy in the radiative transfer modelling between the two free parameters, f_0 and R_e, visible as the elongated 1σ-confidence intervals. This degeneracy is most significant for the main isotopologue, ^{28}Si^{16}O, where abundances in the range $0.6–10\times10^{-5}$ can reproduce the emission to within the uncertainties, according to the very clear trend that a lower f_0 requires a larger R_e (Fig. 9a). This is a consequence of the high optical depth involved in the radiative transfer of this molecule. Natural upper limits to R_e and f_0 can in this case be set by the size of the CO envelope and the Si abundance (Si/H $\approx 3.2\times10^{-5}$; Asplund et al. 2009) which implies SiO/H$_2$ $\lesssim 6.4\times10^{-5}$ or $\log$(SiO/H$_2$) $\lesssim -4.2$ if all silicon is comprised in SiO and all H is in molecular form.

González Delgado et al. (2003) and Schöier et al. (2004) modelled thermal SiO emission ($J = 2–1$, 3–2, 5–4, 6–5) from the CSE of R Dor. More recently, Van de Sande et al. (2018) additionally modelled several high-J transitions (up to $J = 38–37$). Based on interferometric observations of SiO ($J = 2–1$), Schöier et al. (2004) found that the SiO abundance profile of R Dor is possibly better represented by a compact component with a high, constant, abundance of 4×10^{-5} out to $r = 1.2\times10^{15}$ cm and a component with a low abundance (3×10^{-6} and declining according to a Gaussian profile) at larger radii. The discontinuity in the abundance is thought to reflect the signature of depletion of SiO onto dust. Since we restrict our modelling to higher-excitation transitions, ignoring the possible depletion signature as derived by Schöier et al. (2004) is not expected to pose a problem. Our best-fit value of f_0 falls in between those of the previous models and our uncertainties cover both the low-lying values of González Delgado et al. (2003) and Schöier et al. (2004) and the high f_0 found by Van de Sande et al. (2018). The range of acceptable values of R_e we find is also in agreement with the results of both González Delgado et al. (2003), Schöier et al. (2004), and Van de Sande et al. (2018, as presented in their Fig. 6).

We are not aware of any earlier efforts to model the thermal emission of the less abundant isotopologues ^{29}SiO, ^{30}SiO, Si^{17}O, and Si^{18}O, except for the modelling by Decin et al.

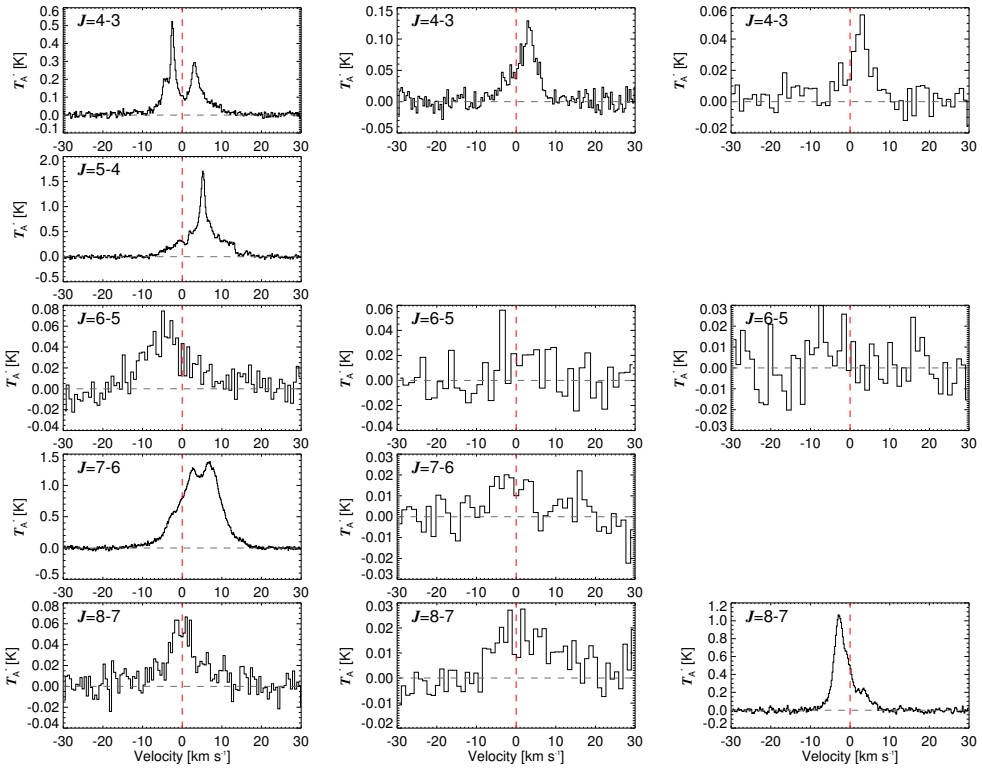

(a) ^{28}Si^{16}O (b) ^{29}Si^{16}O (c) ^{30}Si^{16}O

Fig. 6. SiO isotopologue $v = 1$ line emission. We point out that the ^{30}SiO ($v = 1$, $J = 8$–7) emission is blended with emission from SO_2 ($v_2 = 1$, $J_{K_a,K_c} = 6_{5,1}$–$7_{4,4}$) centred at ~3 km s^{-1} in the rest frame of the SiO line.

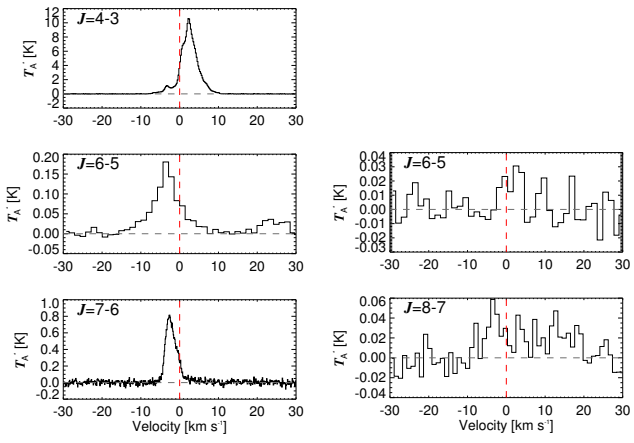

(a) ^{28}Si^{16}O (b) ^{29}Si^{16}O

Fig. 7. SiO isotopologue $v = 2$ line emission.

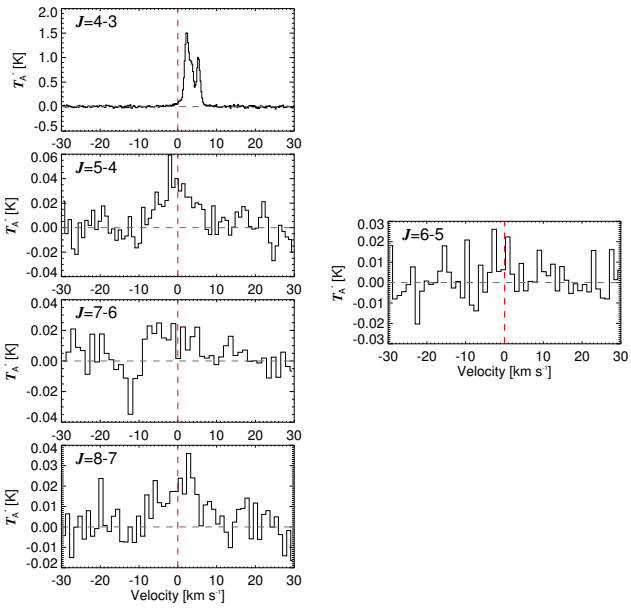

(a) $v = 3$ (b) $v = 5$

Fig. 8. ^{28}Si^{16}O line emission in higher excited states.

(2010) of two ^{29}SiO transitions measured towards IK Tau. We set up our model grids based on the one for ^{28}SiO, covering the same values for R_e and scaling those for f_0 with a reasonable value for the appropriate isotopic ratio. See Table 2 for the grid specifications and model results. Figures 4 and 5 show that our model predictions reproduce the observed data very well. We note that the remarkable quality of the fit to all emission lines simultaneously, for each of the modelled isotopologues, demonstrates that the survey's internal data calibration uncertainty is actually (significantly) lower than the 20% we quote as absolute uncertainty in Sect. 2. To assess the variability in SiO line emission as a consequence of stellar variability, we calculated a radiative transfer model (for ^{28}SiO) based on our best-fit model, but decreasing the luminosity to 4500 $L_\odot$. This significant change in luminosity leads to changes in intensity within 20% and in integrated line intensity within 15% for the observed

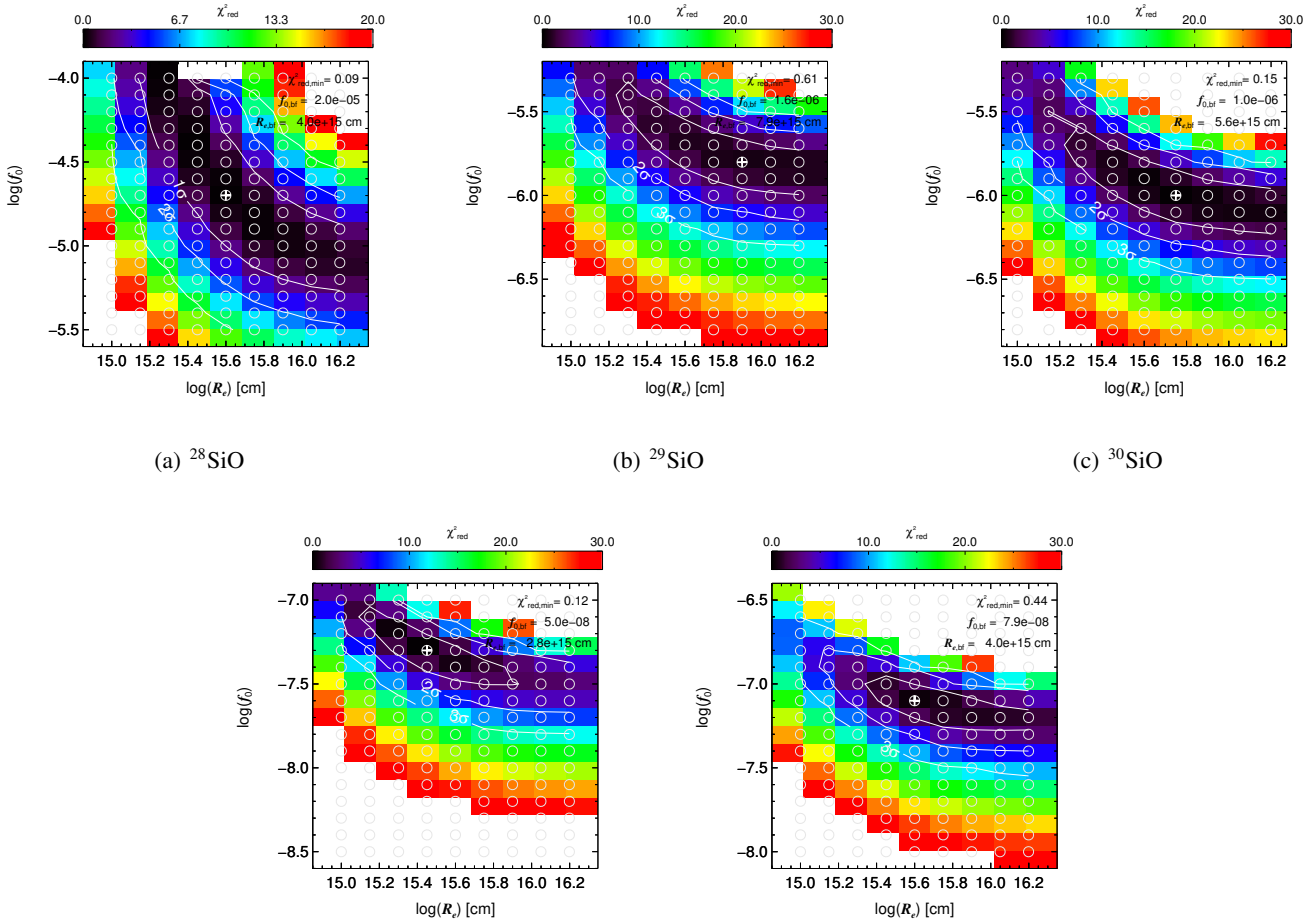

Fig. 9. Reduced-χ^2 maps of the model grids for the $v = 0$ state of five SiO isotopologues. Circles indicate the grid points and white crosses indicate the best-fit models. Contours are given at the ~68%, ~95%, and 99.7% confidence intervals (1σ, 2σ, and 3σ, respectively).

lines. Such line variability would hence not be significant with respect to the observational uncertainties in the selection of our models.

To obtain isotopologue abundance ratios from these results, we consider all models, that is, combinations of f_0 and R_e, that fall within 1σ of the best-fit model for a given isotopologue. Additionally, assuming that all isotopologues are photodissociated by the interstellar radiation field at the same radius and, hence, have the same e-folding radius R_e, we can reduce the uncertainties on these ratios by only considering the abundance ratios at a given R_e. This approach leads to the values and uncertainties listed in Table 3 and discussed in Sect. 3.3.

3.2.3. Water

We detect eight emission features of H_2O: the well-known masers at 183 and 321 GHz in the vibrational ground state, and five and one lines in the vibrationally excited states v_2 and $2v_2$, respectively, see Fig. 10. The maser at 325 GHz was not observed. Maercker et al. (2016) carried out a detailed radiative transfer study of the H_2O line emission observed with HIFI towards a sample of oxygen-rich stars, including R Dor. A similar study of the vibrationally excited H_2O lines in this survey and of several more oxygen-rich AGB stars is forthcoming and will be based on these results.

3.2.4. Hydrogen cyanide, cyanide

We detect emission from the $J = 2$–1,3–2, and 4–3 transitions of both $H^{12}CN$ and $H^{13}CN$; see Fig. 11. Our observation of the $H^{12}CN$(3–2) line is consistent within 10% with the spectrum presented by Schöier et al. (2013). For the $H^{12}CN$(4–3) line the latter authors only listed an integrated intensity and did not show the spectrum. The integrated intensity in our survey is 77% of that reported by Schöier et al. (2013). This is within reasonable calibration uncertainties. We are not aware of earlier observations of the $J = 2$–1 line or of any previously reported detections of $H^{13}CN$ for R Dor. We do not include radiative transfer modelling of $H^{12}CN$ and $H^{13}CN$ in this paper.

We do not detect CN(2–1) emission, but we do detect two clear components of the CN(3–2) line; see Fig. 12. These components coincide with the intrinsically brightest hyperfine structure components of the transition. We do not detect ^{13}CN, in line with the intensity of the ^{12}CN emission and the $^{12}C/^{13}C$ isotopic ratio derived by Ramstedt & Olofsson (2014).

3.2.5. Sulphur-bearing species

We identify 16 lines of ^{32}SO and 12 of ^{34}SO. We identify 118 lines of $^{32}SO_2$ in the vibrational ground state, and 1 in the $v_2 = 1$ state (Fig. 13), 5 lines of $^{34}SO_2$, 10 lines of $SO^{18}O$, and 2 lines of $SO^{17}O$.

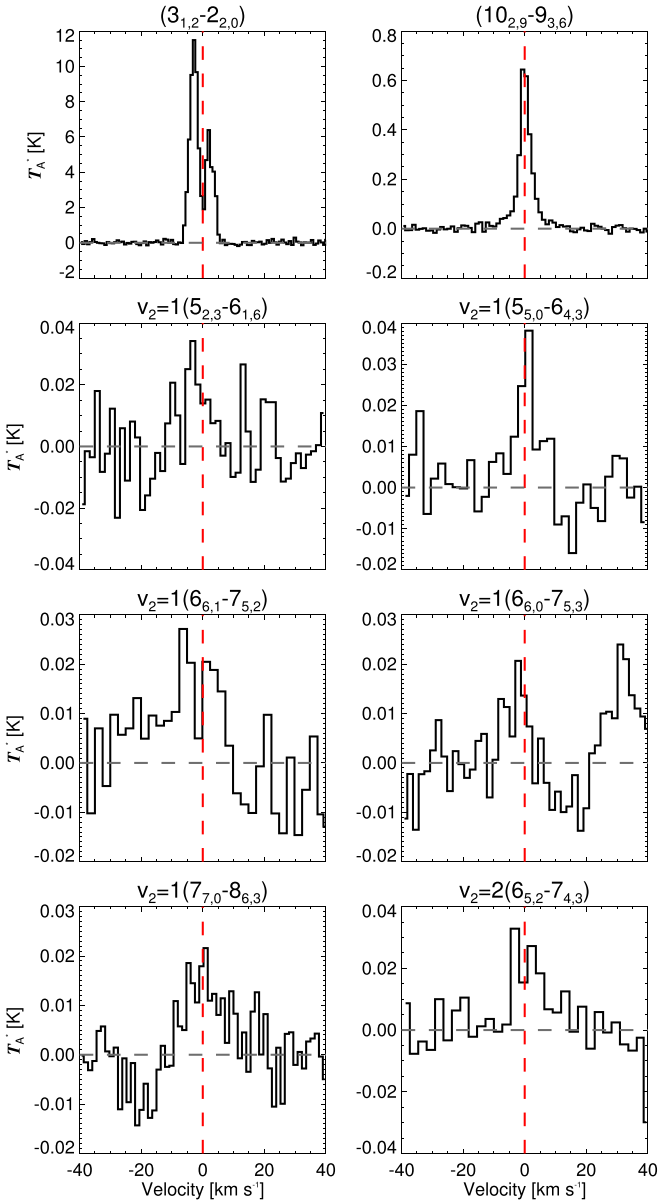

Fig. 10. H_2O emission in the vibrational ground state and the vibrationally excited states $v_2 = 1, 2$.

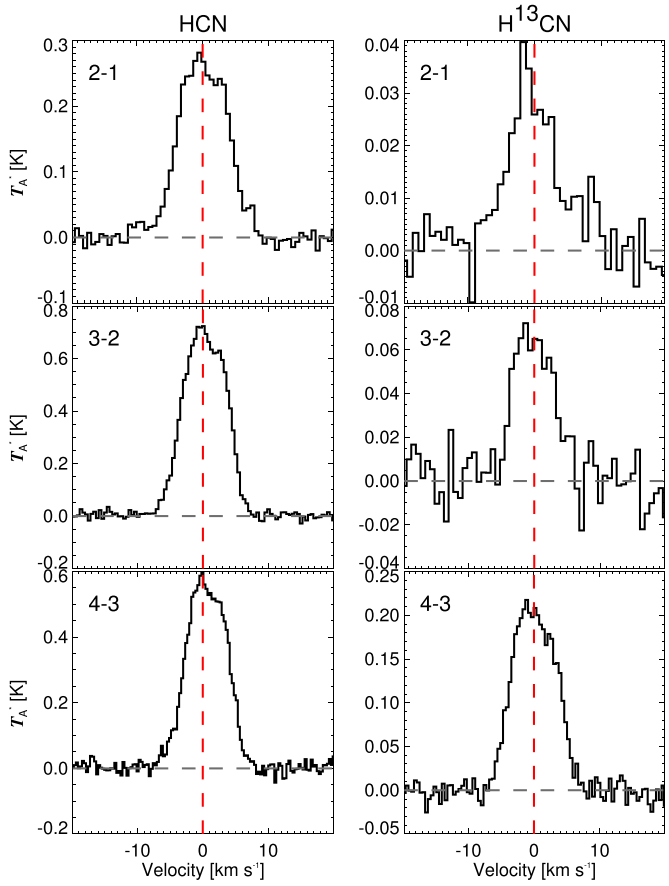

Fig. 11. HCN emission in the survey: $H^{12}CN$ (*left*) and $H^{13}CN$ (*right*).

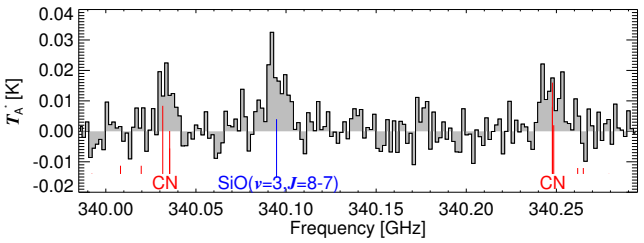

Fig. 12. CN(3–2) emission. The positions of the red vertical lines indicate the rest frequencies of the hfs components, and their lengths are proportional to the relative component strengths in LTE.

Danilovich et al. (2016) presented detailed radiative transfer models of both the SO and SO_2 emission we observe towards R Dor, as well as towards several other oxygen-rich AGB stars. At the time of that publication, the survey had not been completed, and we have in the mean time identified more SO and SO_2 lines than were available then. A careful check between the lines observed in the range 159–211 GHz and the model predictions shows an excellent agreement for 17 SO_2 and 3 SO lines, and an overprediction of the SO_2 lines $5_{2,4}$–$5_{1,5}$ at 165.1 GHz and $3_{2,2}$–$2_{1,1}$ at 208.7 GHz by about a factor of 2. We note here that the $SO_2(12_{4,8}–12_{3,9})$ transition at 355.05 GHz modelled by Danilovich et al. (2016) has a peak-T_A^* of ∼0.05 K, whereas in additional data obtained in June 2016, it is 0.07 K. This indicates possible time variability in the excitation of SO_2, as is also mentioned by Danilovich et al. (2016).

We detect emission from SiS and CS only tentatively, consistent with the idea that SO and SO_2 are the main sinks of sulphur in low-mass-loss-rate M-type AGB stars (Danilovich et al. 2016). We refer to the latter study for details on the modelled abundance distributions and the implications for the chemical networks.

3.2.6. Phosphorus-bearing molecules

We detect multiple transitions of PO and PN, making R Dor the second oxygen-rich AGB star, after IK Tau (De Beck et al. 2013; Velilla Prieto et al. 2017), for which these species are detected.

Our observations cover three transitions of PO in the Ω = 1/2 lower-spin component: $^2\Pi_{1/2}$ J = 9/2–7/2, $^2\Pi_{1/2}$ J = 11/2–9/2, and $^2\Pi_{1/2}$ J = 13/2–11/2; see Fig. 14. The tentative detection of the first two is strengthened by the definite detection of the third transition. We detect none of the higher-energy Ω = 3/2 upper spin component transitions. Even though the strengths of the doublets in each transition reflect excitation in, or close to, LTE, the derivation of reliable values of excitation temperature

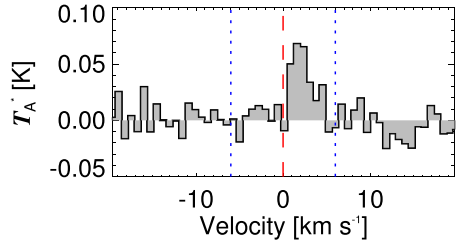

Fig. 13. SO_2, $v_2 = 1$ ($J_{K_a,K_c} = 69_{9,61}$–$70_{6,64}$) emission.

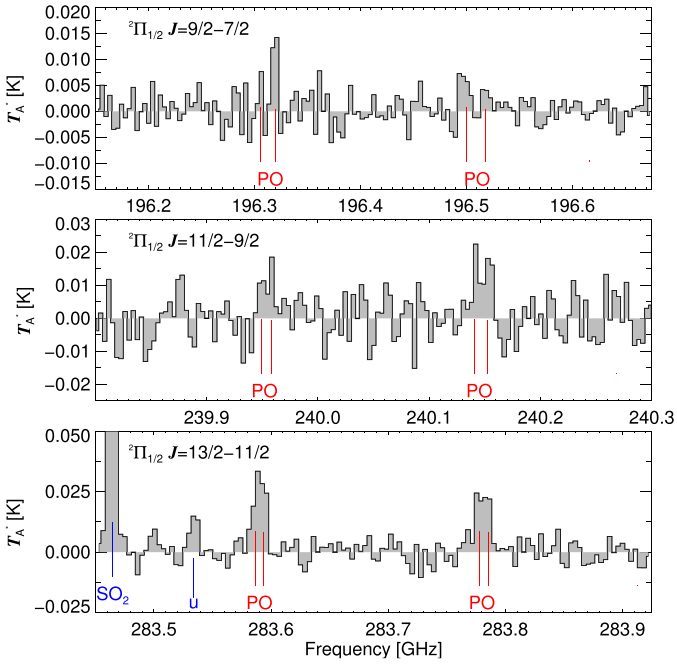

Fig. 14. PO line emission. Vertical red lines mark the rest frequencies of the different hfs components of each rotational transition.

and column density through a rotational-diagram analysis is hindered by the limited sensitivity reached in the observations and the lack of spatial information.

The survey covers four transitions of PN: $J = 4$–$3, \ldots, 7$–6. We show spectra for all four in Fig. 15 and show the result of stacking these using the statistical weights of the upper levels, $2J + 1$, as the weights for the transitions $J - J'$. The resulting spectrum, stacked in velocity space at a velocity resolution of 1.5 km s^{-1}, shows emission at peak-S/N = 3.6. We could not identify any other species that would contribute to the velocity range $[-10; 10]$ km s^{-1} in this stacked spectrum. The best-fit Gaussian profile to the stacked spectrum has a full width at half maximum of 6.8 km s^{-1}, comparable to what we see for high-S/N line emission in the survey. We hence claim the presence of PN in the CSE of R Dor.

Although the peak flux densities for PO and PN for R Dor are higher than those for IK Tau for similar transitions by factors of a few, the sensitivity of our survey is unfortunately not sufficient to compare these detections of PO and PN directly to the results obtained for IK Tau by De Beck et al. (2013) and Velilla Prieto et al. (2017) using the SMA and the IRAM 30 m telescope. Dedicated single-tuning observations at high sensitivity are needed to further investigate the phosphorus-bearing molecules in R Dor.

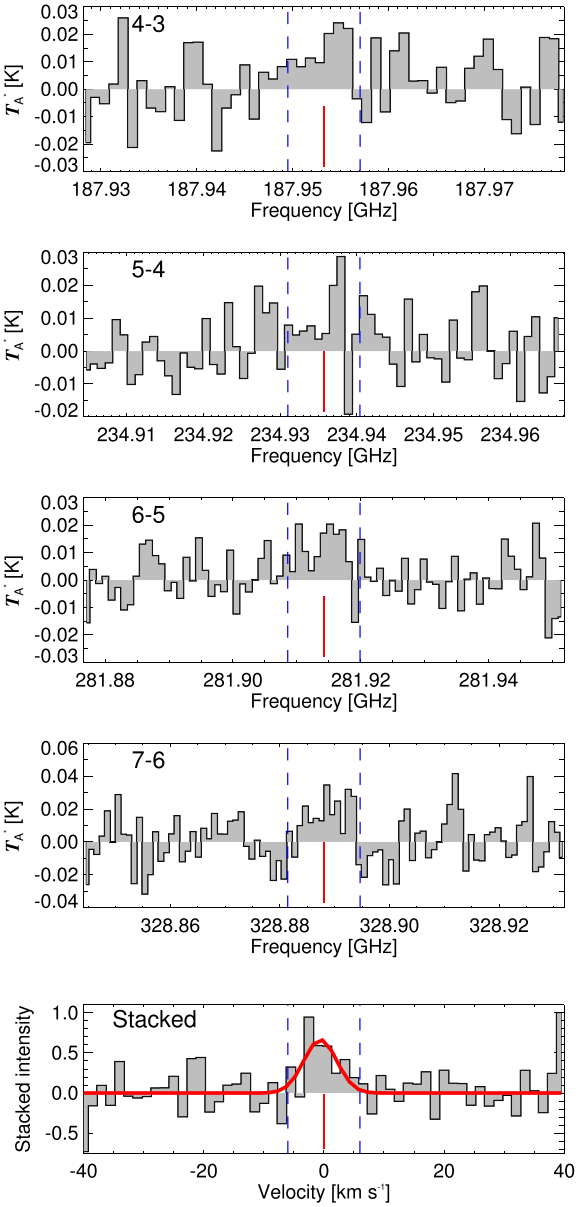

Fig. 15. PN line emission. The first *four panels* show the spectra of the $J = 4$–$3, \ldots, 7$–6 transitions; the *bottom panel* shows the peak-normalised result of stacking these at a velocity resolution of 1.5 km s^{-1}, weighted with the upper level statistical weights, $2J + 1$ of the respective transitions. Red lines indicate the rest frequency (or $v = 0$ km s^{-1} in the *bottom panel*) of each transition, blue lines indicate velocities ± 6 km s^{-1} with respect to the stellar $v_{\rm LSR}$. The red curve in the *bottom panel* represents a Gaussian fit to the stacked data.

We do not conclusively detect any other P-bearing molecules in our survey, but point out a tentative, and, if true, also first, detection of PNO. At 309.4 GHz we detect an emission feature that coincides with the rest frequency of PNO($J = 25$–24); see Fig. 16. We can rule out image band contamination and spectrometer issues, leading to the conclusion that this is an actual emission feature. However, we cannot confirm a detection for any of the other transitions of PNO covered by the survey ($J = 13$–$12, \ldots, 29$–28) and cannot find a stacked spectrum with a significant S/N. Therefore, this tentative detection should be regarded with caution.

We do not detect the ground-state PH_3($J_K = 1_0$–0_0) line at 266.9 GHz. Based on the NH_3 brightness reported by

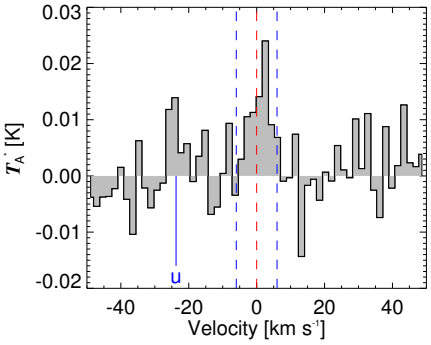

Fig. 16. Tentative identification of PNO line emission. The red dashed line corresponds to the rest frequency of the PNO($J = 25$–24) transition and the blue dashed lines indicate the stellar $v_{\rm LSR}$ ±6 km s^{-1}. In blue we indicate an unidentified emission feature.

Justtanont et al. (2012) and a P/N abundance ratio of ∼0.004 (Asplund et al. 2009), we estimate its peak intensity at < 2 mK, whereas the sensitivity of our survey reaches 5.6 mK rms noise at a 2 km s^{-1} resolution at this frequency. However, this is a zeroth-order estimate which assumes similar behaviour of NH_3 and PH_3, and an analogous estimate for IK Tau leads to a peak antenna temperature of ∼30 mK for the IRAM 30 m telescope, which is invalidated by the observations presented by Velilla Prieto et al. (2017).

We have successfully applied for ALMA Cycle 5 observations to observe PO, PN, and PH_3 in the CSEs of R Dor and IK Tau, but at the date of submission of this manuscript, no data have been obtained yet.

3.2.7. Heavy metal species: titanium, aluminium, sodium

Titanium- and aluminium-bearing molecules could be critical in the dust-condensation process, and much effort has recently gone into searching for such species (De Beck et al. 2015b, 2017; Decin et al. 2017; Kamiński et al. 2013a, 2016, 2017).

We do not detect any emission from TiO in this survey, but claim a possible detection of TiO_2, based on a peak S/N of ∼3 in the stacked spectrum of a set of 18 low-S/N tentative detections; see Fig. 17. The sensitivity of the observations is, however, not sufficient to set up a relevant abundance or rotational-diagram analysis. One emission feature in the spectrum agrees with a component of TiN (8–7), which, if confirmed, would be a first detection of this molecule in space. However, if true, we only detect one of the two doublet components of the 8–7 transition at 297.4 GHz clearly, although their theoretical strengths are identical. Furthermore, we do not detect emission of any other TiN transition in this survey (5–4, . . . , 9–8). Image sideband contamination is ruled out and we can identify no other candidate carrier for this feature. Additionally, investigation of the survey of IK Tau from Velilla Prieto et al. (2017) shows a low-level peak at the same position, 297.4 GHz, further supporting that this is a genuine spectral feature (Sect. 3.4).

We detect no emission from the aluminium-bearing species AlO, AlOH and AlCl with certainty, although 4, 6, and 14 transitions, respectively, are covered by the survey (AlO: 6–5, . . . , 9–8; AlOH: 6–5, . . . , 11–10; AlCl: 11–10, . . . , 25–24). In the case of AlO, only a tentative detection could possibly be claimed for the 9–8 transition (De Beck et al. 2017). Stacking of these lines is difficult owing to the hyperfine structure of the individual transitions not lining up in velocity space. Recent ALMA observations at much higher sensitivity detect these species in the CSEs of R Dor and IK Tau (Decin et al. 2017), with peak flux densities consistent with the non-detections in our APEX observations.

We tentatively detect emission from NaCl in the vibrational ground state $v = 0$ ($J = 19$–18, 23–22) and in the $v = 2$ vibrationally excited state ($J = 19$–18) at S/N of about 3, 2.5, and 5, respectively; see Fig. 18. The part of the spectrum with the $v = 2$ emission was observed at two different dates, one time in September 2011 and the other in November 2015. We see a change in both the intensity and width of the measured profile between the two observations. The aforementioned S/N is for the combined spectrum. Given the likely radiative excitation of such vibrationally excited transitions, this line variability is possibly linked to stellar variability. Given the sensitivity of our survey data we cannot conclusively identify other lines of NaCl in the spectrum at an acceptable S/N. Figure 18 additionally shows a stacked spectrum combining all parts of the spectrum where NaCl (in the vibrational ground state $v = 0$) has rotational transitions and that are not obviously contaminated by line emission from other species or by high noise. The resulting Gaussian fit has a $S/N \approx 3$, further supporting the tentative identification of NaCl emission in the spectrum. Multiple emission lines of NaCl, in the vibrational ground state as well as in vibrationally excited states, have been detected towards IK Tau and VY CMa (Milam et al. 2007; Decin et al. 2016; Velilla Prieto et al. 2017).

3.3. Isotopes

Our survey covers emission from isotopologues containing different isotopes of carbon (^{12}C, ^{13}C), oxygen (^{16}O, ^{17}O, and ^{18}O), silicon (^{28}Si, ^{29}Si, ^{30}Si), and sulphur (^{32}S, ^{34}S).

Accurate isotopic ratios of different elements carry information on the evolutionary stage and/or the initial mass of an AGB star, based on the assumption that the circumstellar (molecular) isotopologue ratios are representative of the atmospheric (elemental) isotopic ratios. This assumption is reasonable, since the only currently known chemical processes involved in changing the isotopologue ratio are fractionation in the very coldest parts of the CSE and isotope-selective photodissociation, for example, of CO (Visser et al. 2009). Saberi et al. (2017) discuss the difference between ^{12}CO/^{13}CO and H^{12}CN/H^{13}CN in the CSE of the AGB star R Scl as a result of isotope-selective photodissociation in the case of CO, and how, consequently, H^{12}CN/H^{13}CN is likely more representative of the stellar ^{12}C/^{13}C in certain cases. Since the dissociation of SiO is in the continuum, we expect our derived isotopologue ratios to be representative also for the elemental isotopic ratios of silicon and oxygen.

We summarise intensity ratios for a large set of isotopologue emission lines in our survey in Table 3. These transition-specific values, $R_{\rm a/b,J-J'}$, are obtained as

$$R_{\rm a/b,J-J'} = \frac{I_{\rm a,J-J'}}{I_{\rm b,J-J'}} \times \left(\frac{\nu_{\rm a,J-J'}}{\nu_{\rm b,J-J'}}\right)^{-3}, \quad (3)$$

where $\nu_{J-J'}$ is the rest frequency of each rotational transition $J - J'$, $I_{J-J'}$ is its integrated line intensity, and "a" and "b" denote the different isotopic variations. The cubic frequency-dependent correction factor accounts for the difference in beam-filling (when all lines are assumed spatially unresolved) and in intrinsic line strength (see e.g. Schöier & Olofsson 2000; De Beck et al. 2010). We also list approximate isotopologue ratios $R_{\rm a/b}$, calculated as the weighted average of the transition-specific values,

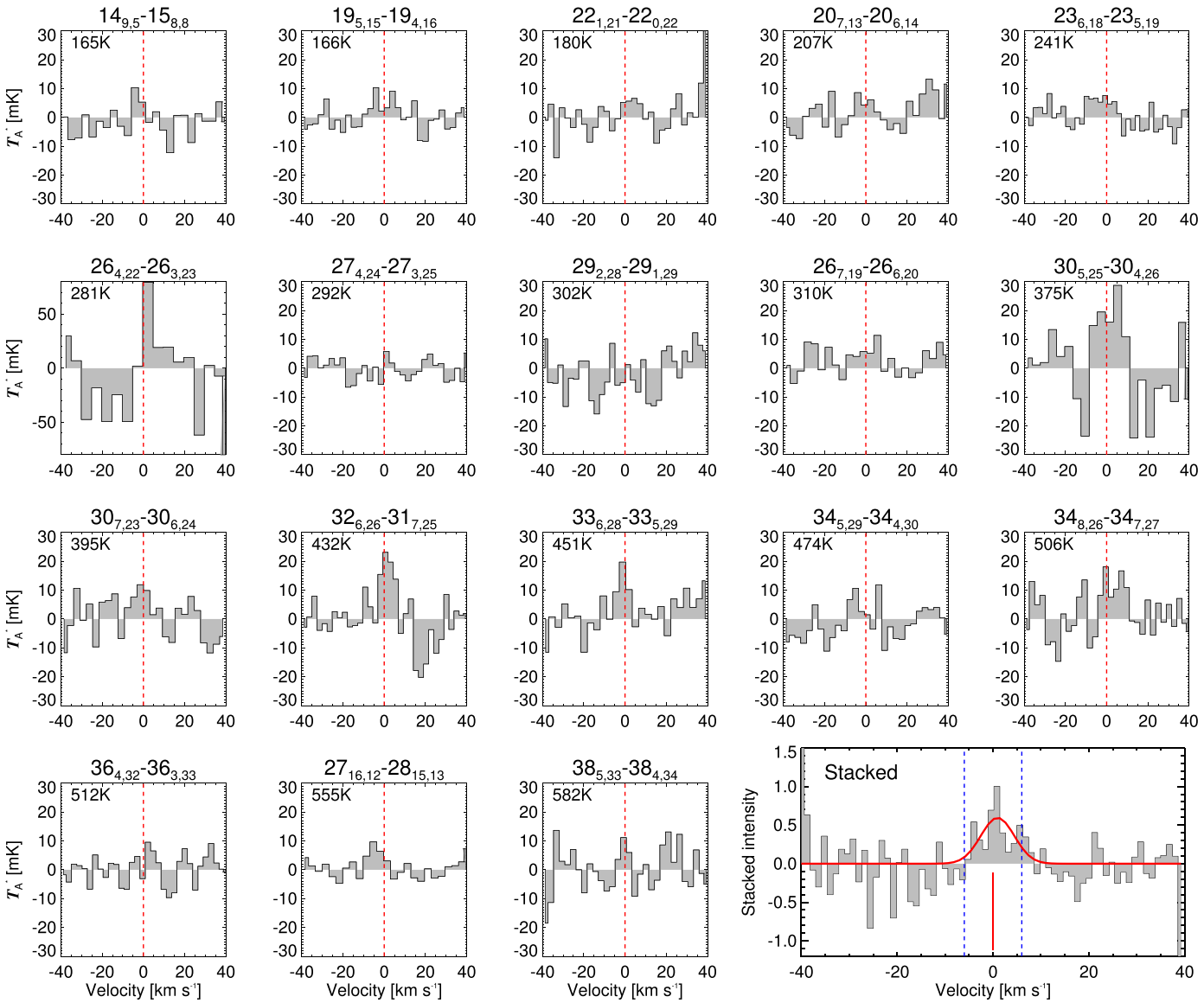

Fig. 17. Tentative identification of TiO_2 line emission. Quantum numbers for each transition and upper-level energies E_{up}/k are given for each panel. The last panel shows the spectrum that results from stacking (in velocity space, at 1.2 km s^{-1} resolution) the spectra in the other 18 panels, assuming equal weights. The red line represents a best-fit Gaussian curve to the stacked spectrum.

assuming the uncertainties as the inverse weights. We note that these ratios are sometimes obtained from optically thick line emission, which is likely when a highly abundant isotopologue is considered and is very clear in the case of ^{28}SiO, so in these cases the obtained ratio should be considered a limiting value. Only the isotopologue ratios obtained from detailed radiative transfer modelling (R_{RT}) and those derived from exclusively optically thin line emission are representative of the actual isotopic ratio in the CSE. All calculations of line ratios in this section are based on a 15% uncertainty on the line intensities. This is reasonable, and maybe rather conservative, given that most lines that are compared directly have been observed (quasi-)simultaneously and are almost always observed with the same instrument.

3.3.1. Carbon: CO, HCN

Ramstedt & Olofsson (2014) determine ^{12}CO/^{13}CO to be ~10 for R Dor, based on radiative transfer modelling of CO. Although optical depth could affect the line ratios for both CO and HCN, the values we find from line intensity ratios are consistent with the value derived by Ramstedt & Olofsson (2014). We do not re-model the CO line emission, nor model the HCN line emission here, but plan a detailed radiative transfer analysis of the H^{12}CN and H^{13}CN line emission in the future.

The derived ^{12}C/^{13}C is significantly lower than any values predicted by theoretical models, an issue also discussed by Ramstedt & Olofsson (2014).

3.3.2. Oxygen: SiO

From the line intensity ratios we find an isotopologue abundance ratio ^{28}Si^{17}O/^{28}Si^{18}O ≈ 0.5 ± 0.1 (Table 3). From the radiative transfer modelling presented in Sect. 3.2.2, we derive ^{28}Si^{17}O/^{28}Si^{18}O = 0.6 ± 0.2. Assuming that the isotopologue abundance ratio derived for the CSE is equal to the elemental ^{17}O/^{18}O isotopic ratio at the stellar surface we find that ^{17}O/^{18}O = 0.6 ± 0.2, implying an initial mass, M_i for R Dor

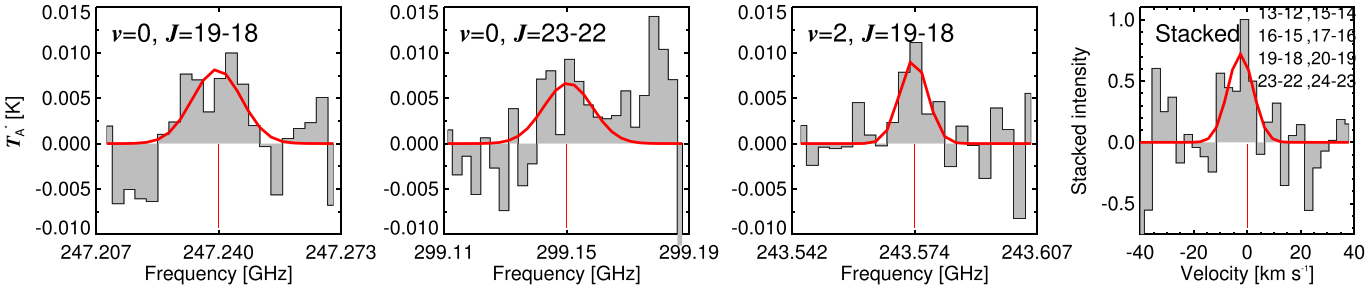

Fig. 18. Tentative detection of NaCl line emission. The *first three panels* show tentative detections; for the $v = 2$, $J = 19$–18 spectrum, this is the combination of observations obtained at two different epochs (see text). The *last panel* shows a stacked spectrum using all rotational transitions (in $v = 0$) marked in the *top right-hand corner*.

of $1.4^{+0.2}_{-0.1}\,M_\odot$ (Karakas & Lugaro 2016; Cristallo et al. 2015, assuming solar metallicity).

Independently from the study presented here, Danilovich et al. (2017a) model the emission of several transitions of $H_2^{17}O$ and $H_2^{18}O$ towards R Dor and derive isotopologue abundance ratios o-$H_2^{17}O$/o-$H_2^{18}O = 0.54 \pm 0.26$ and p-$H_2^{17}O$/p-$H_2^{18}O = 0.30 \pm 0.10$ for ortho-H_2O and para-H_2O, respectively, from which they derive an initial mass in the range 1.0–1.3 $M_\odot$, although a slightly larger range of 1.0–1.6 $M_\odot$ seems to better reflect their results. These results are in agreement with our findings based on the SiO emission, increasing the reliability of the derived $^{17}O/^{18}O$ for the CSE and of the inital mass estimate, under the assumptions made.

We do not detect $C^{17}O$ or $C^{18}O$ in our survey. Assuming the abundance ratios $Si^{16}O/Si^{17}O$ and $Si^{16}O/Si^{18}O$ to be representative of $C^{16}O/C^{17}O$ and $C^{16}O/C^{18}O$, we run radiative transfer models for $C^{17}O$ and $C^{18}O$. The predictions for the $J = 2$–1 and $J = 3$–2 transitions are in agreement with formal non-detections in the survey, with peak intensities well below 10 and 20 mK for the respective transitions, for both $C^{17}O$ and $C^{18}O$ for peak abundances $f_0 < 10^{-6}$. Such high values of f_0 were considered only because of the large uncertainties on the SiO isotopologue abundance ratios. This upper limit to the abundances means that the uncertainty on $^{18}O/^{16}O$ is smaller than given by our radiative-transfer modelling results in Table 3, and can be constrained to a lower limit of 200.

Based on the evolutionary models of Karakas & Lugaro (2016) and Cristallo et al. (2015), our estimate of $M_i = 1.3$–1.6 $M_\odot$ implies that if R Dor becomes a carbon-rich AGB star it will only do so in its final phases with a C/O ratio only slightly above 1. During its lifetime of ∼1.6 Myr on the thermally pulsing AGB (TP-AGB), the star would dredge up $\lesssim 0.01\,M_\odot$. According to Karakas & Lugaro (2016), this would happen over the course of ∼16 TP cycles, whereas Cristallo et al. (2015) quote only 5 TP cycles for a star with $M_i = 1.5\,M_\odot$.

3.3.3. Silicon: SiO

From the radiative transfer modelling described in Sect. 3.2.2 we derive isotopologue abundance ratios $^{28}SiO/^{29}SiO = 12.6^{79.4}_{1.6}$, $^{28}SiO/^{30}SiO = 20.0^{79.4}_{2.0}$, and $^{29}SiO/^{30}SiO = 1.6^{6.3}_{0.4}$. The latter is in good agreement with the line intensity ratio $R_{^{29}SiO/^{30}SiO} = 1.4 \pm 0.1$ (Table 3). These derived ratios are in agreement with the solar isotopic ratios $^{29}Si/^{30}Si = 1.5$ and $^{28}Si/^{30}Si = 29.9$ (Asplund et al. 2009). The models of Karakas & Lugaro (2016) indeed show no, or insignificant, changes in $^{28}Si/^{29}Si$ and $^{28}Si/^{30}Si$ as a consequence of AGB evolution for initial masses $\leq 2\,M_\odot$.

3.3.4. Sulphur: SO, SO_2

Danilovich et al. (2016) derived $^{32}S/^{34}S = 22 \pm 9$ from detailed radiative transfer models of SO and SO_2. This is in good agreement with the solar value $^{32}S/^{34}S = 22.1$ (Asplund et al. 2009) and the model results that sulphur does not show significant changes in its isotopic ratios throughout AGB evolution.

3.3.5. Evolutionary stage

In order to constrain not only the initial mass of R Dor, but also its evolutionary stage, we need observationally determined isotopic ratios for, for example, nitrogen ($^{14}N/^{15}N$) and aluminium ($^{26}Al/^{27}Al$), based on highly sensitive observations. Furthermore, there is a strong need for better constrained theoretical models for the variation of $^{12}C/^{13}C$ throughout the AGB evolution. We refer to Ramstedt & Olofsson (2014) for an in-depth discussion on the low $^{12}C/^{13}C$ found for oxygen-rich AGB stars compared to stellar evolution models.

3.4. Unidentified lines

We list the unidentified features in Table 4 with the rest frequencies, peak intensities, and FWHMs obtained from a Gaussian line profile fitting and show the spectra and their fits in Fig. 19. The listed velocity resolution gives a $S/N \geq 3$ for the Gaussian fit in all cases. For all unidentified features we are able to rule out instrumental effects and image contamination, thanks to the coverage of our survey. None of these lines are reported for the SMA and IRAM 30 m surveys of IK Tau, VY CMa , or IRC + 10 216 (De Beck et al. 2013; Kamiński et al. 2013b; Patel et al. 2011; Velilla Prieto et al. 2017). One unidentified feature, at 297.4 GHz, seems to be present in the IRAM 30 m survey of IK Tau, but was not explicitly reported by Velilla Prieto et al. (2017). The fully independent detections of this feature towards two significantly different CSEs and using two different telescopes suggests that it is genuine.

3.4.1. A new maser at 354.2 GHz

The most striking unidentified feature appears at 354.2 GHz and is markedly maser-like in its shape. The emission reaches a peak antenna temperature of ∼1.6 K (∼66 Jy; peak-$S/N \approx 55$ at 0.1 km s^{-1} resolution), and a total integrated intensity of 4.7 K km s^{-1} (∼193 Jy km s^{-1}). A detailed check of the collected data reveals that this feature is present in all consecutively obtained individual scans and that its distinct shape is repeated in

Table 3. Isotopic ratios retrieved from line-intensity ratios, with R_c the frequency-corrected ratio: per transition this corresponds to $R_c = R_{a/b,J-J'}$ and overall to $R_c = R_{a/b}$, the error-weighted mean ratio.

	Isotopologues	Transition	R_c	R_{RT}	$R_\odot$	Remarks
C	$^{12}CO/^{13}CO$	2–1	17.0 ± 3.6			
		3–2	9.1 ± 1.9			
			10.9 ± 1.7	10		R_{RT} from Ramstedt & Olofsson (2014).
	$H^{12}CN/H^{13}CN$	2–1	8.4 ± 1.8			
		3–2	9.0 ± 1.9			
		4–3	2.4 ± 0.5			$H^{13}CN(J=4–3)$ is blended.
			8.7 ± 1.3			Excluding the 4–3 transitions.
					$^{12}C/^{13}C = 89.40$	
Si	$^{28}SiO/^{29}SiO$	4–3	2.3 ± 0.5			
		5–4	3.2 ± 0.7			
		6–5	3.2 ± 0.7			
		7–6	2.5 ± 0.5			
		8–7	3.1 ± 0.7			
			2.8 ± 0.3	$12.6^{39.8}_{3.98}$	$^{28}Si/^{29}Si = 19.69$	
	$^{28}SiO/^{30}SiO$	4–3	4.0 ± 0.8			
		5–4	4.3 ± 0.9			
		6–5	4.2 ± 0.9			
		7–6	4.1 ± 0.9			
		8–7	4.0 ± 0.8			
			4.1 ± 0.4	$20.0^{63.1}_{6.31}$	$^{28}Si/^{30}Si = 29.87$	
	$^{29}SiO/^{30}SiO$	4–3	1.7 ± 0.4			
		5–4	1.4 ± 0.3			
		6–5	1.3 ± 0.3			
		7–6	1.6 ± 0.3			
		8–7	1.3 ± 0.3			
			1.4 ± 0.1	$1.58^{2.51}_{1.00}$	$^{29}Si/^{30}Si = 1.517$	
O	$^{28}Si^{16}O/^{28}Si^{17}O$	4–3	76.3 ± 16.2			
		5–4	65.7 ± 13.9			
		6–5	54.0 ± 11.5			
		7–6	57.1 ± 12.1			
		8–7	61.6 ± 13.1			
			61.2 ± 5.8	398^{2000}_{200}	$^{16}O/^{17}O = 2632$	
	$^{28}Si^{16}O/^{28}Si^{18}O$	4–3	38.1 ± 8.1			
		5–4	47.9 ± 10.1			
		6–5	30.6 ± 6.5			
		7–6	24.9 ± 5.3			
			31.5 ± 3.4	251^{1000}_{100}	$^{16}O/^{18}O = 498.8$	
	$^{28}Si^{17}O/^{28}Si^{18}O$	4–3	0.5 ± 0.1			
		5–4	0.7 ± 0.2			
		6–5	0.6 ± 0.1			
		7–6	0.4 ± 0.1			
			0.5 ± 0.1	$0.631^{0.794}_{0.398}$	$^{17}O/^{18}O = 0.190$	
	$C^{16}O/C^{17}O$	2–1	–			
		3–2	–			
			–	>200		Non-detection of $C^{17}O$ emission.
	$C^{16}O/C^{18}O$	2–1	–			
		3–2	–			
			–	>200		Non-detection of $C^{18}O$ emission.
S	$^{32}SO_2/^{34}SO_2$	Overall spectrum		21.6 ± 8.5	$^{32}S/^{34}S = 22.1$	R_{RT} from Danilovich et al. (2016)

Notes. When available, we also list the isotopologue abundance ratios R_{RT} obtained from radiative transfer modelling. Solar (elemental) isotopic ratios $R_\odot$ are taken from Asplund et al. (2009, see their Table 3). See text for details.

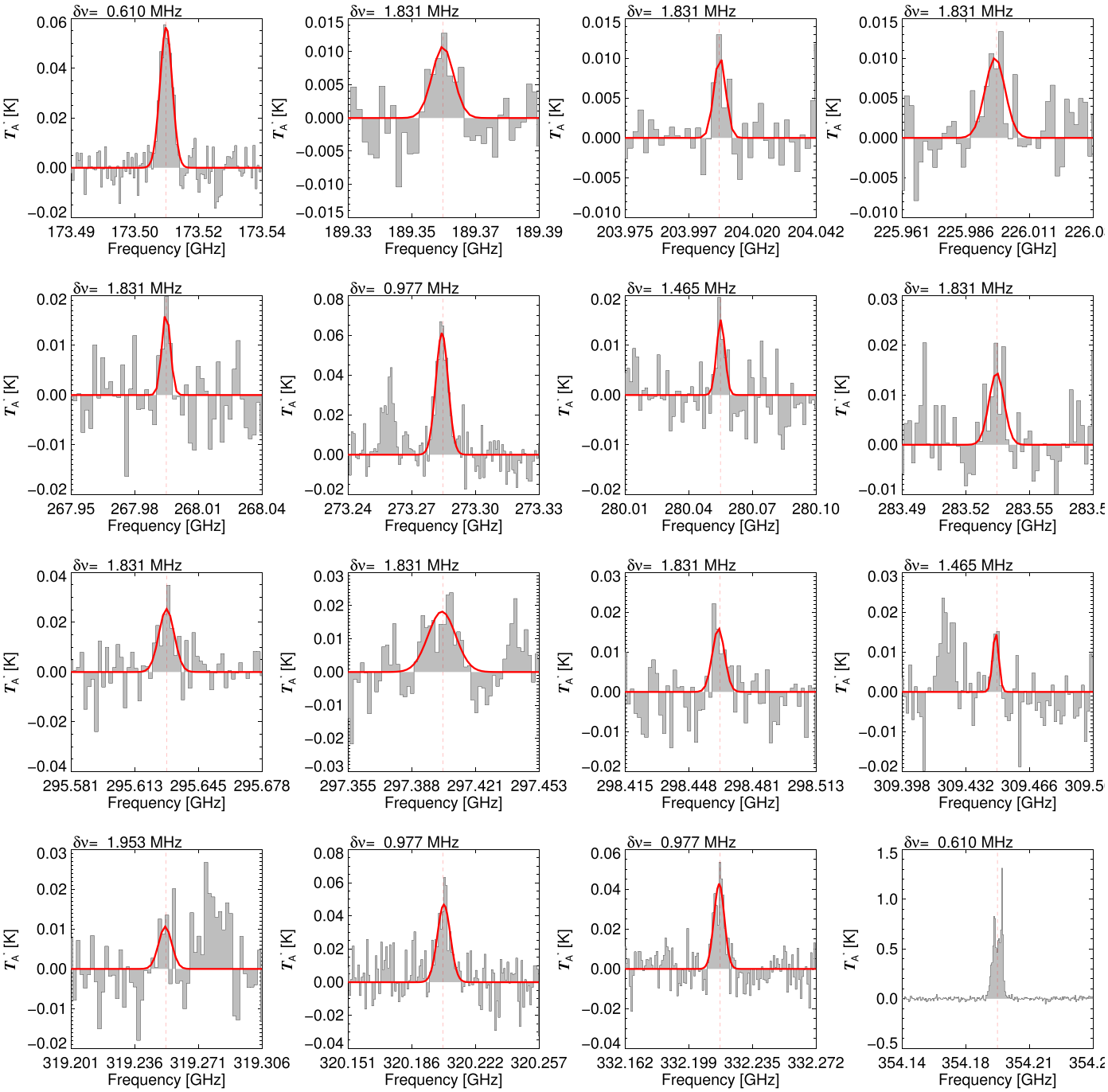

Fig. 19. Unidentified line emission features. We fit a single Gaussian line profile to each of these, except the suspected maser line at 354 GHz, and list the retrieved central frequency, peak intensity, and FWHM at the given velocity resolution in Table 4. The corresponding frequency resolution $\delta\nu$ of the spectra is given at the *top left of each panel*.

all of these. In combination with the resemblance to other spectral lines in the survey (see discussion below) this leads us to believe that this feature is a real spectral emission line.

We compare the emission feature to three maser lines in our survey with a similar shape, H_2O ($J = 3_{1,2}$–$2_{2,0}$) at 183.3 GHz, SiO($v = 3$, $J = 4$–3) at 170.1 GHz, and SiO($v = 1$, $J = 7$–6) at 301.8 GHz, in Fig. 20. In order to align the peaks in the unidentified feature with those of the former two, we need to centre the line at 354.195 and 354.200 GHz, respectively. This shift is due to the fact that the H_2O line emission originates in both the blue and red sides of the wind, whereas this particular SiO maser seems to originate almost exclusively from the redshifted part of the wind. From the comparison in Fig. 20, it seems that the emission could be "H_2O-like", rather than "SiO-like" when one considers that the reddest emission in the profile has no counterpart in the SiO maser emission. However, the closest known H_2O maser to this frequency lies at 354.8 GHz (Gray et al. 2016) and none of the listed transitions of the isotopologues $H_2^{17}O$ and $H_2^{18}O$ coincide with this frequency, either.

Searching the spectroscopic catalogues we found only the ortho-H_2SiO (silanone) doublet $J_{K_a,K_c} = 10_{4,7}$–$9_{4,6}$ and $J_{K_a,K_a} = 10_{4,6}$–$9_{4,5}$ to be a potential candidate (Bailleux et al. 1994).

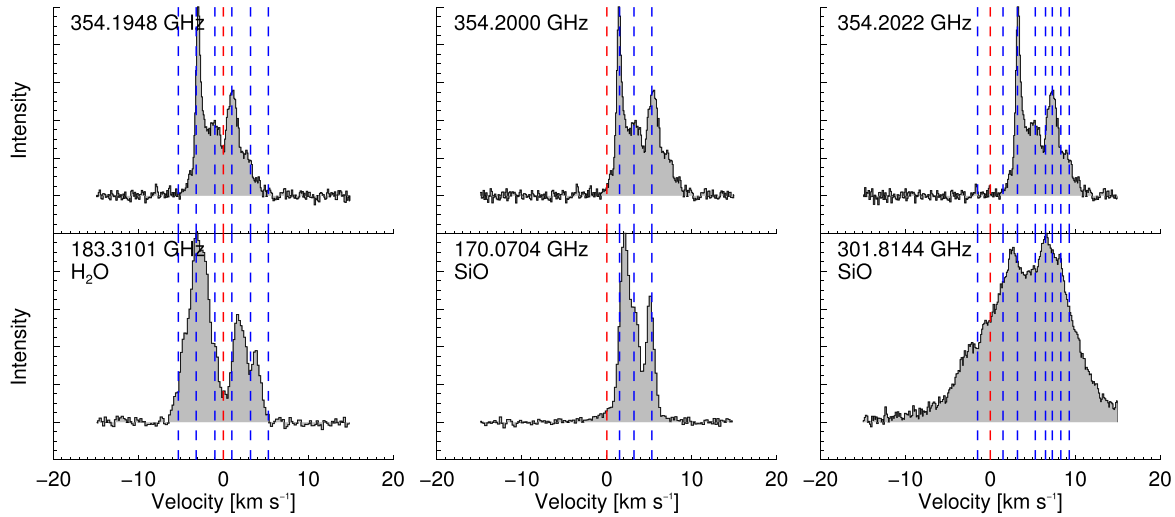

Fig. 20. Alignment in velocity space of unidentified emission at ~354.2 GHz (*top*) with known maser emission (*bottom*). The spectra shown in the top panels, from left to right, assume rest frequencies of 354.1948, 354.2000, and 354.2022 GHz, respectively. The bottom panels show, from *left* to *right*, H_2O (J_{K_a,K_c} = $3_{1,3}$–$2_{2,0}$) at 183.3 GHz, SiO (v = 3, J = 4–3) at 170.1 GHz, and SiO (v = 1, J = 7–6) at 301.8 GHz. Vertical dashed lines indicate emission components similar to those mentioned in the discussion in Sect. 3.

Table 4. Unidentified emission features.

Frequency (MHz)	$T^*_{A,\mathrm{peak}}$ (mK)	FWHM (km s^{-1})	δv (km s^{-1})	Remarks
173 514	56	7.4	1.1	
189 362	10	13.2	2.9	
204 008	9	8.2	2.7	
225 998	10	11.1	2.4	
267 993	16	5.1	2.0	
273 284	61	7.6	1.1	
280 051	14	5.0	1.6	
283 535	13	9.3	1.9	
295 629	25	9.0	1.9	
297 404	17	16.0	1.8	Also seen towards IK Tau. TiN only tentative candidate.
298 464	16	7.5	1.8	
309 449	13	3.9	1.4	
319 253	10	8.0	1.8	
320 204	46	7.8	0.9	
332 217	42	6.3	0.9	
354 195	1600	–[†]	0.5	Maser. H_2SiO? See Sect. 3.4.1.

Notes. The listed frequency, peak temperature, and FWHM are obtained from fitting a Gaussian line profile at the velocity resolution δv – see Fig. 19. [†] We do not fit a Gaussian line profile to this emission feature.

The doublet is located at 354 202.1540 MHz, with lower and upper level energies of 191 K and 208 K, respectively. The upper limit on the uncertainty on this rest frequency listed in CDMS is 0.02 MHz. If confirmed, this is, to our knowledge, the first detection of this molecule in space. Assuming this as the rest frequency moves the emission entirely to the red velocities, with little or no resemblance with the H_2O maser and the first SiO maser in Fig. 20. However, the maser emission of the SiO (v = 1, J = 7–6) line at 301.8 GHz (rightmost bottom panel in Fig. 20) is also dominated by redshifted emission and shows some distinct peaks that might very well correspond to those seen in the new feature. Recently, Gobrecht et al. (2016) predicted that H_2SiO can reach abundances of up to 10^{-6}–10^{-5} in the inner wind of the oxygen-rich, high-mass-loss-rate Mira-type variable IK Tau. H_2SiO, together with HSiO, is thought crucial in the nucleation of silicate dust clusters. Whether or not these predictions can be used as representative of the low-mass-loss-rate, semi-regular variable R Dor is not clear. We do not detect any other emission from H_2SiO in our survey, even though transitions over a large range of excitation energies are covered. Given the maser nature of the emission line tentatively identified as H_2SiO, it is difficult to assess whether the non-detections are consistent with this detection.

Additional observations at this frequency, carried out on 9 June 2016, unfortunately do not reveal any trace of the emission at a ~10 mK rms noise level at 2 km s^{-1} resolution. Archival observations of R Dor, obtained with APEX on 26 March 2008, equally show no detectable emission at 354.2 GHz, however at a much worse rms noise of ~400 mK. We point out that the survey observations at this particular frequency were carried out on 1 September 2011, when the light curve variations of R Dor were quite regular. Currently, however, R Dor's light curve is much more chaotic and shows smaller overall amplitude changes (source: AAVSO). Considering the maser nature of the line, this change might very well significantly affect the excitation of this unidentified line.

Observations at this frequency and other frequencies of likely observable line emission in the H_2SiO spectrum should also be obtained for a larger sample of AGB stars, with an initial focus on M-type stars in order to understand the physical conditions under which this maser line could be excited.

4. Comparison to other line surveys

Spectral surveys of CSEs of M-type evolved stars have been published only in recent years. This includes the AGB stars IK Tau and OH 231.8+4.2 (De Beck et al. 2013, 2015a; Sánchez Contreras et al. 2011, 2015; Velilla Prieto et al. 2015, 2017), the red supergiant VY CMa Kamiński et al. (2013b), and the yellow

hypergiant IRC + 10 420 (Quintana-Lacaci et al. 2016). All of these stars lose mass at high rates (roughly $\gtrsim 0.5 \times 10^{-5}\,M_\odot\,\mathrm{yr}^{-1}$; e.g. De Beck et al. 2010; Velilla Prieto et al. 2015, and references therein), leading to significantly higher densities in their CSEs than is the case for R Dor, with its low mass-loss rate and low expansion velocity ($\dot{M} = 1\text{–}2 \times 10^{-7}\,M_\odot\,\mathrm{yr}^{-1}$, $v_\mathrm{exp} = 5.7\,\mathrm{km\,s}^{-1}$; Maercker et al. 2016). Apart from IK Tau and R Dor, all of these sources have been shown to have outflows that very strongly deviate from smooth, spherical, constant winds (e.g. Bujarrabal et al. 2002; Castro-Carrizo et al. 2007; Richards et al. 2014, and references therein). Given all of the above, we only compare our results to those obtained for IK Tau.

Figure C.1 shows a direct comparison of our APEX data of R Dor with the IRAM 30 m data of IK Tau from Velilla Prieto et al. (2017) scaled to account for the difference in intensity that would be an effect of the different mass-loss rate and distance of the two objects and for the difference in point-source sensitivity between the telescopes (see Appendix C). The sensitivity reached in the spectral scan of IK Tau is better than that of the R Dor spectral scan presented here. However, the ratio of the rms noise to the peak intensity of the closest CO emission lines is similar when assuming a spectral resolution (2 MHz and 0.6 MHz for IK Tau and R Dor, respectively) that results in the same number of spectral elements covering the full line width of twice the expansion velocity (v_exp is 18.5 and 5.7 km s^{-1} for IK Tau and R Dor, respectively). This allows us, to a certain degree, to compare the two surveys.

Both surveys show many spectral features pertaining to SO_2 and SiO, including isotopologues and multiple vibrational states, with strong emission lines from SiS and CS notably missing from the R Dor spectrum. The observations of IK Tau reveal several other molecules that we do not detect towards R Dor: H_2S, NS, HNC, NO, H_2CO, and HCO^+. We do not detect any molecules towards R Dor that are not seen towards IK Tau, apart from (tentatively) some specific, low-abundance isotopologues. At the same time, it is remarkable that none of the R Dor u-lines (except for possibly one) are seen in the IK Tau spectrum.

Danilovich et al. (2016) already reported that SO and SO_2 are the main reservoirs of S in the CSE of R Dor and that their abundances roughly decrease with increasing mass-loss rate when also studying other M-type CSEs (including IK Tau). Danilovich et al. (2017b) reported that H_2S is unlikely to play any significant role at mass-loss rates $\lesssim 5 \times 10^{-6}\,M_\odot\,\mathrm{yr}^{-1}$. This is consistent with the lack of CS, SiS, and H_2S in R Dor.

Assuming the simple scale factor quoted above, we find that all HNC, NO, H_2CO, or HCO^+ emission lines would fall below the detection limit of our observations. Additionally, assuming that the HNC/HCN intensity ratios found for IK Tau also hold for R Dor, further supports the non-detection of all observed HNC transitions ($J = 2\text{–}1$, 3–2, 4–3). Considering this, we cannot rule out that R Dor would show emission from these molecules in more sensitive observations and cannot claim, from our survey results, a difference in chemistry to be at the base of the absence of emission from these in the case of R Dor. However, this difference is clearly at the base of the differences seen between the sulphur-bearing species in the two CSEs. Stacking did not lead to tentative detections for any of these molecules.

The H_2O isotopologue model results of Danilovich et al. (2017a) imply $M_\mathrm{i} = 1.0\text{–}1.6\,M_\odot$ for both R Dor and IK Tau. The integrated line intensities of $Si^{17}O$ and $Si^{18}O$ reported by Velilla Prieto et al. (2017), unfortunately, do not constrain very well the ratio $Si^{17}O/Si^{18}O$, making an independent estimate of $^{17}O/^{18}O$ impossible. The fact that the two stars appear so different in terms of pulsational and mass-loss properties (IK Tau is a Mira, R Dor is an SRb variable; their mass-loss rates differ by 1–2 orders of magnitude) leads us to hypothesise that IK Tau could be in a later stage of its AGB evolution than R Dor, considering the trend of increasing mass-loss rate, expansion velocity, luminosity, and pulsation period with evolution along the TP-AGB (e.g. Vassiliadis & Wood 1993).

5. Outflow kinematics

In case of a smooth, spherical wind described by a constant mass-loss rate, one expects a smooth line profile in the range flat-topped to parabolic for spatially unresolved emission, while spatially resolved emission leads to enhanced (in a relative sense) emission at the extreme velocities, where the lines may even become double-horned. The line profiles in the survey are largely represented by this range of profiles, indicating that the outflow of R Dor can, most likely, be approximated by a spherical wind. However, we do find multiple peaks in several line profiles, indicative of deviations from this simple structure. The CO emission lines observed with APEX and HIFI (Justtanont et al. 2012) show a small bump at the stellar v_LSR and several features at other velocities. In Fig. 21 we show the presence of a distinct emission feature in several lines, pertaining to different species, at $-5.2\,\mathrm{km\,s}^{-1}$ with respect to the systemic velocity. This is clearest for the SiO lines, in particular for ^{29}SiO and ^{30}SiO ($J = 4\text{–}3, \ldots, 8\text{–}7$; Fig. 21i and j), and for ^{28}SiO observed with HIFI ($J = 12\text{–}11, \ldots, 28\text{–}27$; Fig. 21h). An analogous red-shifted component at $5.2\,\mathrm{km\,s}^{-1}$ is marginally visible in the HIFI observations of CO($J = 10\text{–}9$ and 16–15; Fig. 21b) and is more clearly seen in the emission of, for example, SO_2 ($7_{2,6\text{–}6_{1,5}}$, $16_{0,16}\text{–}15_{1,15}$, $12_{4,8}\text{–}12_{3,9}$, $25_{3,23}\text{–}25_{2,24}$; Fig. 21l). These lines have E_up/k of 36, 121, 111, and 326 K, tracing a large range of excitation energies. Based on the above, the features at $v_\mathrm{LSR} \pm 5.2\,\mathrm{km\,s}^{-1}$ are probably real. We additionally propose the existence of features at ± 2.0 and $\pm 3.5\,\mathrm{km\,s}^{-1}$ with respect to the stellar v_LSR . We show a selection of SiO maser emission lines in Fig. 22 and indicate the ± 2.0, ± 3.5, and $\pm 5.2\,\mathrm{km\,s}^{-1}$ positions. These velocities in many cases correspond to individual maser peaks, or have peaks that fall exactly in between them, strengthening the idea that these velocities are linked to some physical structure in the outflow.

Furthermore, the o-$H_2O(1_{1,0}\text{–}1_{0,1})$ line observed with HIFI and shown by Maercker et al. (2016) shows clear bumps in the profile on both the red- and blue-shifted sides of the main emission component, at about $\pm 10\,\mathrm{km\,s}^{-1}$. We see similar bumps for different lines in our survey, for example HCN(2–1) and SO(6_5–5_4), albeit at a low intensity level. At $\pm 10\,\mathrm{km\,s}^{-1}$ we also detect maser emission in, for example, SiO($v = 1$, $J = 5\text{–}4$, 7–6) and SiO($v = 2$, $J = 6\text{–}5$); see Fig. 22.

We conclude that the spectrally resolved emission lines of R Dor show signs of tracing up to five components in the CSE of R Dor: (1) a dominant component centred at the stellar v_LSR ($6.5\,\mathrm{km\,s}^{-1}$), and components that arise at (2) $\pm 2.0\,\mathrm{km\,s}^{-1}$, (3) $\pm 3.5\,\mathrm{km\,s}^{-1}$, (4) $\pm 5.2\,\mathrm{km\,s}^{-1}$, and (5) $\pm \sim 10\,\mathrm{km\,s}^{-1}$ with respect to the stellar v_LSR . From our spatially unresolved observations, we cannot readily draw conclusions on the geometry of these extra components. Their apparent symmetry around the v_LSR likely excludes that they are "random" inhomogeneities in the outflow and might imply that they are spatially confined in, for example, rings, shells, or spiral arms, but this is not an entirely straightforward explanation. The components are traced by line emissions of various molecular species that do not necessarily

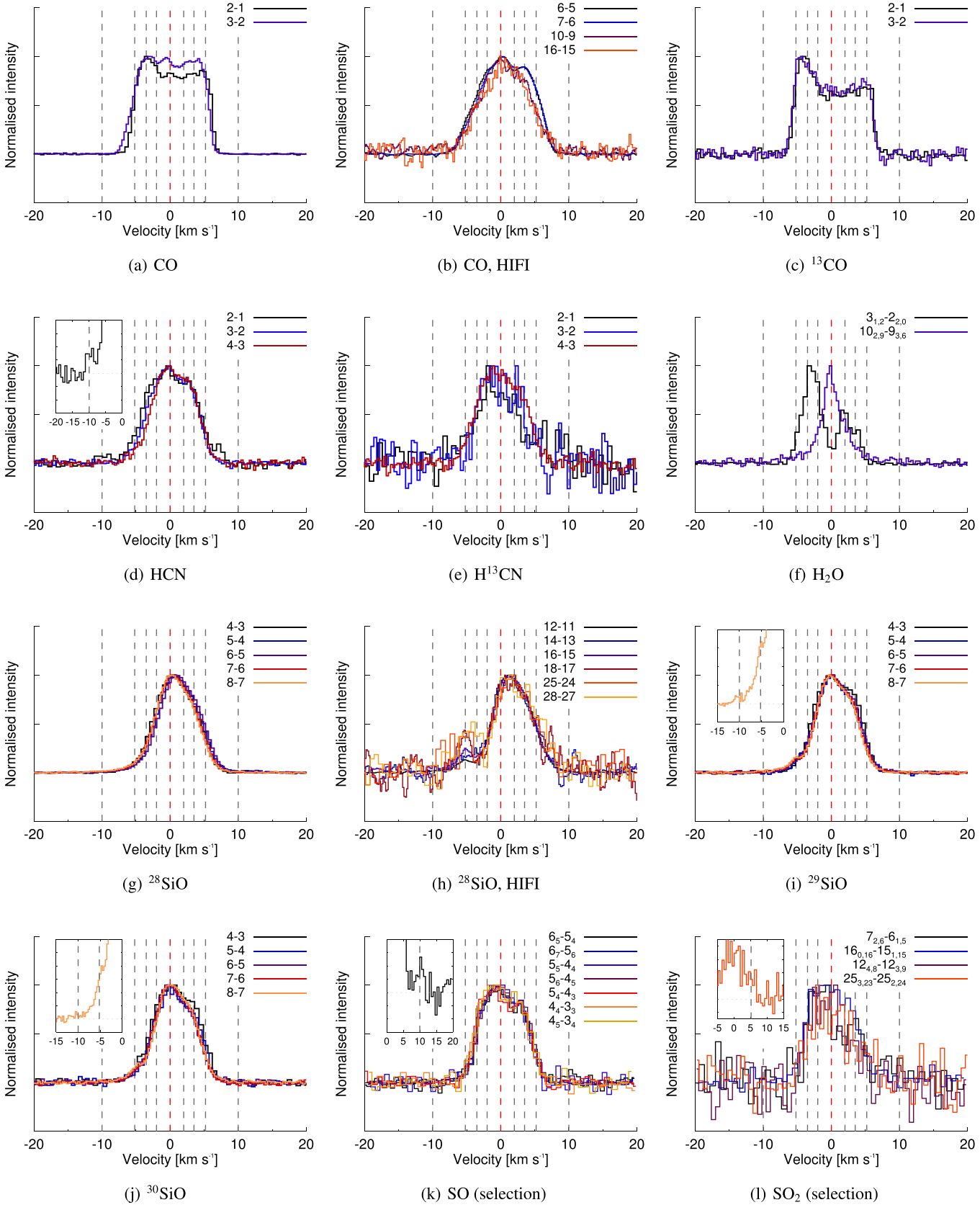

(a) CO (b) CO, HIFI (c) ^{13}CO

(d) HCN (e) H^{13}CN (f) H_2O

(g) ^{28}SiO (h) ^{28}SiO, HIFI (i) ^{29}SiO

(j) ^{30}SiO (k) SO (selection) (l) SO_2 (selection)

Fig. 21. Line shapes. Vertical dashed lines correspond to velocities 0, ±2.0, ±3.5, and ±5.2 km s^{-1} with respect to the stellar v_{LSR}, where distinct emission features appear in multiple of the presented lines. Insets (with the same colour coding as the main plots) are added to several of the panels for increased visibility of these substructures.

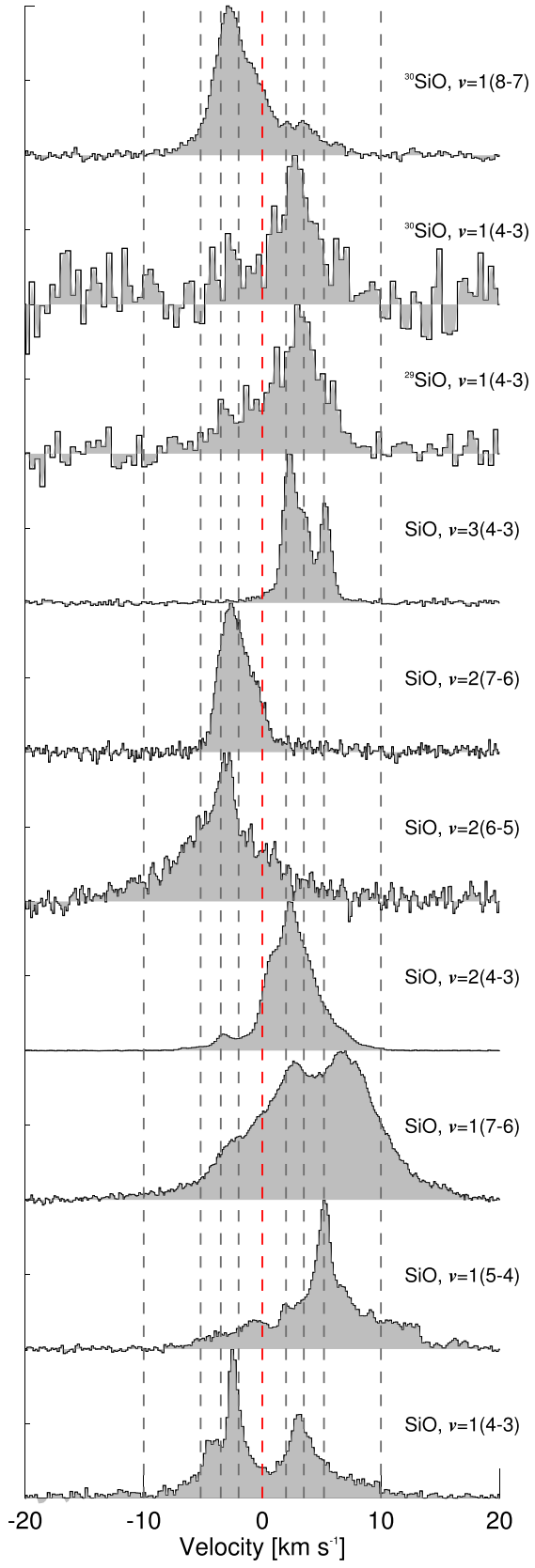

Fig. 22. Selected SiO maser emission lines. Vertical dashed lines correspond to the velocities (relative to the stellar $v_{\rm LSR}$) 0.0, ±2.0, ±3.5, ±5.2, and ±10.0 km s^{-1}. Intensities are normalised to the peak and vertical offsets are added for visibility. We note that the observations are not coeval; see Appendix B.

reside in the same parts of the CSE, and by transitions with very different excitation properties. Also, since the main wind has an expansion velocity of 5.7 km s^{-1} (e.g. Maercker et al. 2016) the extra emission at ∼10 km s^{-1} poses a problem in a smooth, monotonously accelerating wind. We very carefully speculate that this could be a higher-velocity outflow component very close to the star, given that we see it in SiO maser line emission and H_2O line emission, both believed to originate close to the star. Observations that resolve the emission both spectrally and spatially are clearly necessary to constrain the kinematics and geometry of the outflow and its possible components.

6. Conclusions

We present a spectral scan of the circumstellar environment of the oxygen-rich AGB star R Dor over the range 159.0–368.5 GHz, interrupted at 321.5–338.5 GHz. We carried out the observations with the APEX telescope, using the new SEPIA/Band-5 and the SHeFI facility instruments. This is the first survey of the circumstellar emission from this nearby, low-mass-loss-rate star over a large frequency range and is only the second such survey published in its entirety for an oxygen-rich AGB star after the one for IK Tau by Velilla Prieto et al. (2017). Thus far, efforts have mainly been targeted at carbon-rich and high-mass-loss rate objects such as IRC + 10 216 or red supergiants such as VY CMa .

The survey exhibits roughly 320 spectral features (omitting those linked to instrumental effects). The flux in the spectrum is heavily dominated by thermal and maser emission from the different SiO isotopologues. In numbers, the SO_2 emission lines dominate by far. We detect several lines of CO(^{12}CO and ^{13}CO), HCN (H^{12}CN and H^{13}CN), SiO (^{28}SiO, ^{29}SiO, ^{30}SiO, Si^{17}O, Si^{18}O), CN, H_2O, SO, and SO_2. We detect PO and PN, the latter through a stacked spectrum, for the first time towards this source, but cannot claim the conclusive detection of any other P-bearing molecules. We note that ALMA observations will be performed to study in more detail the phosphorous chemistry in the CSEs of R Dor and IK Tau. We suggest the tentative detection of TiO_2, also from a stacked spectrum, AlO, and NaCl in the spectrum. These species are considered potentially important in the dust-condensation process. Sixteen features are currently still unidentified. Of these, one is a very strong maser at 354.2 GHz, which is possibly identifiable as H_2SiO (silanone). We could not confirm the presence of this emission in R Dor's spectrum at a later time, but are positive that we are dealing with a real spectral feature and not an instrumental effect of any type.

We present radiative transfer models for the thermal emission in the vibrational ground state (v = 0) of five silicon monoxide isotopologues: ^{28}SiO, ^{29}SiO, ^{30}SiO, Si^{17}O, and Si^{18}O. Radiative transfer models of the SO and SO_2 emission in a large part of the survey was already presented by Danilovich et al. (2016).

We provide estimates for isotopic ratios for C, O, Si, and S, both from line-intensity ratios and from radiative transfer models. Using the derived circumstellar Si^{17}O/Si^{18}O as a proxy for the stellar ^{17}O/^{18}O we constrain the initial mass of R Dor to the range 1.3–1.6 $M_\odot$.

We find detailed features in the emission line profiles that arise in many of the emission lines, both thermal and maser emission, spread throughout the full spectrum and also in several emission lines measured with Herschel/HIFI. We suggest that these could trace up to five components in the CSE of R Dor: (1) a dominant smooth component centred at the stellar $v_{\rm LSR}$, and components that arise at (2) ±2.0 km s^{-1}, (3) ±3.5 km s^{-1},

(4) $\pm 5.2\,\mathrm{km\,s^{-1}}$, and (5) $\pm\ \sim 10\,\mathrm{km\,s^{-1}}$ with respect to the stellar v_{LSR} . The presence of these indicates possible deviations in the wind of R Dor from a smooth, spherical outflow. Spatially and spectrally resolved observations are needed to decipher what these components could be.

Acknowledgements. EDB acknowledges financial support from the Swedish National Space Board. HO acknowledges financial support from the Swedish Research Council. The APEX observations were obtained under project numbers O-087.F-9319A-2011, O-094.F-9318A-2014, O-096.F-9336A-2015. The authors acknowledge John H. Black for his input to the molecular description of SiO used in the radiative transfer modelling.

References

Asplund, M., Grevesse, N., Sauval, A. J., & Scott, P. 2009, ARA&A, 47, 481
Bailleux, S., Bogey, M., Demuynck, C., et al. 1994, ApJ, 101, 2729
Bedding, T. R. & Zijlstra, A. A. 1998, ApJ, 506, L47
Belitsky, V., Lapkin, I., Fredrixon, M., et al. 2018, A&A, 612, A23
Billade, B., Nyström, O., Meledin, D., et al. 2012, IEEE Trans. Terahertz Sci. Technol., 2, 208
Bujarrabal, V., Alcolea, J., Sánchez Contreras, C., & Sahai, R. 2002, A&A, 389, 271
Castro-Carrizo, A., Quintana-Lacaci, G., Bujarrabal, V., Neri, R., & Alcolea, J. 2007, A&A, 465, 457
Cernicharo, J., Guélin, M., & Kahane, C. 2000, A&AS, 142, 181
Cernicharo, J., Waters, L. B. F. M., Decin, L., et al. 2010, A&A, 521, L8
Cristallo, S., Straniero, O., Piersanti, L., & Gobrecht, D. 2015, ApJS, 219, 40
Danilovich, T., Bergman, P., Justtanont, K., et al. 2014, A&A, 569, A76
Danilovich, T., De Beck, E., Black, J. H., Olofsson, H., & Justtanont, K. 2016, A&A, 588, A119
Danilovich, T., Lombaert, R., Decin, L., et al. 2017a, A&A, 602, A14
Danilovich, T., Van de Sande, M., De Beck, E., et al. 2017b, A&A, 606, A124
Dayou, F. & Balança, C. 2006, A&A, 459, 297
De Beck, E., Decin, L., de Koter, A., et al. 2010, A&A, 523, A18
De Beck, E., Kamiński, T., Patel, N. A., et al. 2013, A&A, 558, A132
De Beck, E., Kamiński, T., Menten, K. M., et al. 2015a, in Why Galaxies Care about AGB Stars III: A Closer Look in Space and Time, eds. F. Kerschbaum, R. F. Wing, & J. Hron, ASP Conf. Ser., 497, 73
De Beck, E., Vlemmings, W., Muller, S., et al. 2015b, A&A, 580, A36
De Beck, E., Decin, L., Ramstedt, S., et al. 2017, A&A, 598, A53
Decin, L., De Beck, E., Brünken, S., et al. 2010, A&A, 516, A69
Decin, L., Richards, A. M. S., Millar, T. J., et al. 2016, A&A, 592, A76
Decin, L., Richards, A. M. S., Waters, L. B. F. M., et al. 2017, A&A, 608, A55
Desmurs, J.-F., Bujarrabal, V., Lindqvist, M., et al. 2014, A&A, 565, A127
de Vicente, P., Bujarrabal, V., Díaz-Pulido, A., et al. 2016, A&A, 589, A74
Gobrecht, D., Cherchneff, I., Sarangi, A., Plane, J. M. C., & Bromley, S. T. 2016, A&A, 585, A6
González Delgado, D., Olofsson, H., Kerschbaum, F., et al. 2003, A&A, 411, 123
Gray, M. D., Baudry, A., Richards, A. M. S., et al. 2016, MNRAS, 456, 374
Humphreys, E. M. L., Gray, M. D., Yates, J. A., & Field, D. 1997, MNRAS, 287, 663
Humphreys, E. M. L., Gray, M. D., Yates, J. A., et al. 2002, A&A, 386, 256
Humphreys, R. M., Helton, L. A., & Jones, T. J. 2007, AJ, 133, 2716
Immer, K., Belitsky, V., Olberg, M., et al. 2016, The Messenger, 165, 13
Justtanont, K., Khouri, T., Maercker, M., et al. 2012, A&A, 537, A144
Kamiński, T., Gottlieb, C. A., Menten, K. M., et al. 2013a, A&A, 551, A113
Kamiński, T., Gottlieb, C. A., Young, K. H., Menten, K. M., & Patel, N. A. 2013b, ApJS, 209, 38
Kamiński, T., Wong, K. T., Schmidt, M. R., et al. 2016, A&A, 592, A42
Kamiński, T., Müller, H. S. P., Schmidt, M. R., et al. 2017, A&A, 599, A59
Karakas, A. I. & Lugaro, M. 2016, ApJ, 825, 26
Khouri, T., de Koter, A., Decin, L., et al. 2014, A&A, 561, A5
Knapp, G. R., Pourbaix, D., Platais, I., & Jorissen, A. 2003, A&A, 403, 993
Maercker, M., Schöier, F. L., Olofsson, H., Bergman, P., & Ramstedt, S. 2008, A&A, 479, 779
Maercker, M., Danilovich, T., Olofsson, H., et al. 2016, A&A, 591, A44
Milam, S. N., Apponi, A. J., Woolf, N. J., & Ziurys, L. M. 2007, ApJ, 668, L131
Morris, M. 1980, ApJ, 236, 823
Müller, H. S. P., Thorwirth, S., Roth, D. A., & Winnewisser, G. 2001, A&A, 370, L49
Müller, H. S. P., Schlöder, F., Stutzki, J., & Winnewisser, G. 2005, J. Mol. Struct. 742, 215
Nyman, L.-A. & Olofsson, H. 1985, A&A, 147, 309
Patel, N. A., Young, K. H., Gottlieb, C. A., et al. 2011, ApJS, 193, 17
Pickett, H. M., Poynter, R. L., Cohen, E. A., et al. 1998, J. Quant. Spec. Rad. Transf., 60, 883
Quintana-Lacaci, G., Agúndez, M., Cernicharo, J., et al. 2016, A&A, 592, A51
Ramstedt, S. & Olofsson, H. 2014, A&A, 566, A145
Richards, A. M. S., Impellizzeri, C. M. V., Humphreys, E. M., et al. 2014, A&A, 572, L9
Saberi, M., Maercker, M., De Beck, E., et al. 2017, A&A, 599, A63
Sánchez Contreras, C., Velilla Prieto, L., Cernicharo, J., et al. 2011, in IAU Symp., 280, The Molecular Universe, Poster I.75
Sánchez Contreras, C., Velilla Prieto, L., Agúndez, M., et al. 2015, A&A, 577, A52
Schöier, F. L. & Olofsson, H. 2000, A&A, 359, 586
Schöier, F. L., Olofsson, H., Wong, T., Lindqvist, M., & Kerschbaum, F. 2004, A&A, 422, 651
Schöier, F. L., Ramstedt, S., Olofsson, H., et al. 2013, A&A, 550, A78
Van de Sande, M., Decin, L., Lombaert, R., et al. 2018, A&A, 609, A63
Vassilev, V., Meledin, D., Lapkin, I., et al. 2008, A&A, 490, 1157
Vassiliadis, E. & Wood, P. R. 1993, ApJ, 413, 641
Velilla Prieto, L., Sánchez Contreras, C., Cernicharo, J., et al. 2015, A&A, 575, A84
Velilla Prieto, L., Sánchez Contreras, C., Cernicharo, J., et al. 2017, A&A, 597, A25
Visser, R., van Dishoeck, E. F., & Black, J. H. 2009, A&A, 503, 323
Zhang, Y., Kwok, S., & Dinh-V-Trung. 2009a, ApJ, 691, 1660
Zhang, Y., Kwok, S., & Nakashima, J.-i. 2009b, ApJ, 700, 1262
Ziurys, L. M., Milam, S. N., Apponi, A. J., & Woolf, N. J. 2007, Nature, 447, 1094

Appendix A: CO monitoring

We show observations of CO emission with single-dish facilities in Fig. A.1. The CO($J = 1$–0, 2–1, 3–2) emission was observed 1990–2000 using the Swedish-ESO Submillimetre Telescope (SEST). The CO($J = 2$–1, 3–2, 4–3) emission was repeatedly observed with APEX in the time frame 2005–2014. The spectra at different epochs can be used to investigate possible variability in the CO emission of R Dor. Unfortunately, we do not have any recent observations of the $J = 1$–0 line, whereas we mainly have recent observations for the higher-J lines, and only a few or none from the 1990s, complicating a coherent time-variability study of the CO emission.

The $J = 1$–0 spectra from the two earliest epochs (1991, 1992) agree very well. The third epoch (1993) shows the presence of an emission feature at 2–5 km s^{-1} red-shifted with respect to the systemic velocity, which is not seen in the earlier epochs. This "extra" peak matches quite well in velocity the features seen in, for example, the CO emission in our APEX survey data (Figs. 3 and 21a) or in any of the $J = 2$–1, 3–2, 4–3 spectra shown in Fig. A.1. We do not have a straightforward explanation for this change in the emission feature of the $J = 1$–0 line. We remind the reader that the e-folding radius for the CO abundance distribution is about 1.6×10^{16} cm (36″ in diameter; Maercker et al. 2016) and that the emitting region of this transition covers a large part of the envelope. For this "extra" spectral feature to be a consequence of a morphological change in the emitting region, a large change within the emitting volume would be required when we assume collisional excitation of CO. The low expansion velocity of ∼6 km s^{-1} leads to only ∼1 AU radial motion over an entire year, the time between the second and third epoch of the observations, too little to cause a significant change at large radii. Unless a very strong, yet relatively small-scale, inhomogeneity started contributing significantly to the $J = 1$–0 emission, a morphological argument seems hard to defend in the case of collisional excitation. However, as argued by Morris (1980) and Khouri et al. (2014), low-density winds like that of R Dor could give rise to a CO envelope that is not dominantly collisionally excited, but where the pumping of CO to its vibrationally excited state by the 4.6 μm radiation from the star plays an important role. Another possible explanation would be that there is variable, weak maser emission in an inhomogeneous envelope (Morris 1980). However, as above, it seems unlikely that the properties of the emitting region would change very drastically within a year.

It is harder to make a case for any observed variability in the case of the $J = 2$–1, 3–2, 4–3 lines. Although small changes do seem to occur between different epochs, it is less clear whether these are real or still within the general observational uncertainties. However, it does seem that the $J = 3$–2 emission has been showing more prominent blue or red bumps depending on the epoch of observation.

We cannot draw any firm conclusions on possible variability based on the single-dish spectra. Spatially resolved observations for one or multiple of these emission lines will be crucial to understand what could possibly be the cause of these changes, along with the origin of the components identified in Sect. 5.

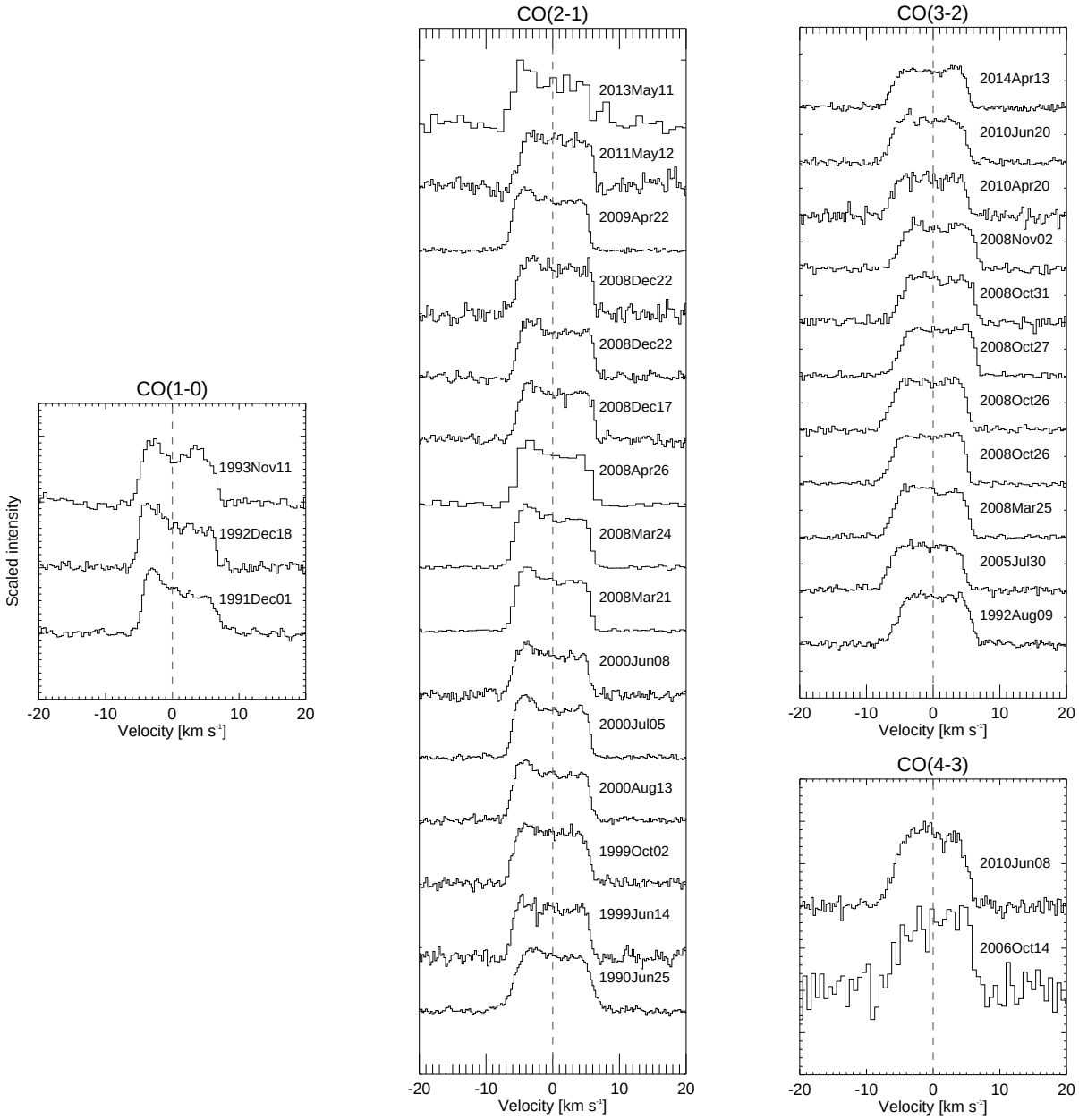

Fig. A.1. CO line emission from R Dor at different observing epochs: emission from $J = 1$–0, 2–1, 3–2 measured by SEST in 1990–2000, and from $J = 2$–1, 3–2, 4–3 by APEX in 2005–2014. The y-axis shows the line intensity at an arbitrary scale, chosen to optimise the visibility of the possible variations.

Appendix B: Maser observations

With this paper we do not aim to study the maser excitation, but rather wish to report on the presence of the lines in the spectrum of R Dor. This is why all presented maser spectra in the main body of the paper are averages over all observations of that particular frequency. However, maser emission around AGB stars is known to significantly vary with time and we did not obtain all observations simultaneously. We therefore list the dates of observation for all maser lines in Table B.1. Figure B.1 presents the date-separated spectra of the maser lines observed on multiple days with significant S/N. We do not discuss any differences or implications of these in this paper. We note that we did not consider variations in those masers observed on consecutive days. If so wished, reduced spectra for separate dates of the other, much weaker, masers can be provided upon request.

Table B.1. Observation dates for all maser lines in the survey, ordered according to increasing rest frequency.

Molecule	Transition	Frequency (MHz)	Observation date
^{30}SiO, $v = 2$	4–3	167 160.943	22, 23 NOV 2015†
^{30}SiO, $v = 1$	4–3	168 323.353	22, 23 NOV 2015†
SiO, $v = 3$	4–3	170 070.348	22, 23 NOV 2015†
^{29}SiO, $v = 1$	4–3	170 328.321	22, 23 NOV 2015†
SiO, $v = 2$	4–3	171 275.165	22, 23 NOV 2015†
SiO, $v = 1$	4–3	172 481.117	22, 23 NOV 2015†
H_2O	$3_{1,2}$–$2_{2,0}$	183 310.087	22, 23 NOV 2015†
^{30}SiO, $v = 2$	5–4	208 946.055	22, 23 NOV 2015†
SiO, $v = 4$	5–4	211 077.906	18 AUG 2014
SiO, $v = 3$	5–4	212 582.550	18 AUG 2014
SiO, $v = 2$	5–4	214 088.575	18 AUG 2014
SiO, $v = 1$	5–4	215 596.018	15 MAY 2011
H_2O, $v_2 = 1$	$5_{5,0}$–$6_{4,3}$	232 686.700	03 SEP 2011
SiO, $v = 5$	6–5	251 481.622	29 JUN 2015
^{30}SiO, $v = 1$	6–5	252 471.372	29 JUN 2015
^{29}SiO, $v = 2$	6–5	253 703.479	30 JUN 2015
^{29}SiO, $v = 1$	6–5	255 478.495	30 JUN 2015
SiO, $v = 2$	6–5	256 898.396	19 NOV 2011, 06 JUN 2012†
SiO, $v = 1$	6–5	258 707.324	19 NOV 2011, 06 JUN 2012†
H_2O, $v_2 = 2$	$6_{5,2}$–$7_{4,3}$	268 149.117	13 JUN 2012, 22 NOV 2012†
H_2O, $v_2 = 1$	$6_{6,1}$–$7_{5,2}$	293 664.491	25 NOV 2011
^{29}SiO, $v = 3$	7–6	293 907.859	25 NOV 2011
H_2O, $v_2 = 1$	$6_{6,0}$–$7_{5,3}$	297 439.276	25 NOV 2011
SiO, $v = 3$	7–6	297 595.467	25 NOV 2011
^{29}SiO, $v = 1$	7–6	298 047.637	25 NOV 2011
SiO, $v = 2$	7–6	299 703.909	25 NOV 2011
SiO, $v = 1$	7–6	301 814.332	17 AUG 2014, 29 NOV 2014†
H_2O	$10_{2,9}$–$9_{3,6}$	321 225.677	24 NOV 2011
^{29}SiO, $v = 3$	8–7	335 880.695	23 NOV 2011
^{30}SiO, $v = 1$	8–7	336 603.002	23 NOV 2011
SiO, $v = 4$	8–7	337 687.290	23 NOV 2011
^{29}SiO, $v = 2$	8–7	338 245.183	23 NOV 2011
SiO, $v = 3$	8–7	340 094.734	22 NOV 2011, 27 JUN 2015†
^{29}SiO, $v = 1$	8–7	340 611.884	22 NOV 2011, 27 JUN 2015†
SiO, $v = 2$	8–7	342 504.383	11 NOV 2011, 26, 27 JUN 2015†
SiO, $v = 1$	8–7	344 916.332	11 NOV 2011, 26, 27 JUN 2015†
u	?	~354 200	01 SEP 2011 09 JUN 2016‡

Notes. $^{(\dagger)}$ Since we are currently not studying the detailed maser variability, observations carried out on multiple dates were averaged in the spectra presented in Fig. C.1 and throughout the paper. If wanted, date-separated spectra can be provided by us or retrieved from the ESO archive. $^{(\ddagger)}$ Maser emission not detected on this date. Data not combined with original survey data.

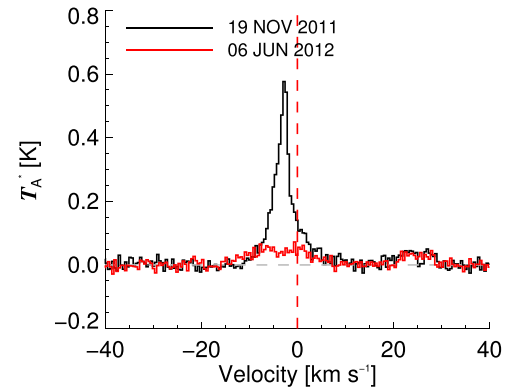

(a) SiO, $v = 2$ ($J = 6 - 5$) at 256.9 GHz

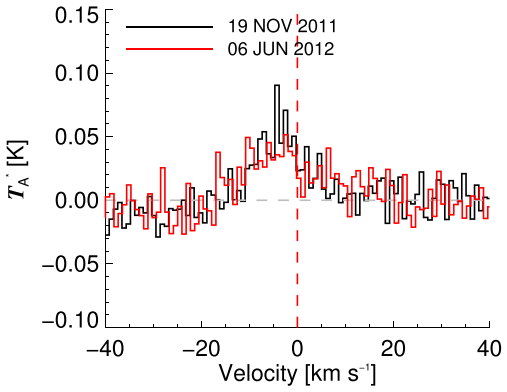

(b) SiO, $v = 1$ ($J = 6 - 5$) at 258.7 GHz

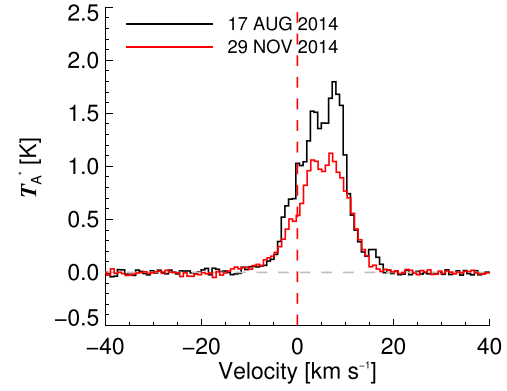

(c) SiO, $v = 1$ ($J = 7 - 6$) at 301.8 GHz

Fig. B.1. Maser variability in our survey data. The rest frequency of each line agrees with a 0 km s^{-1} velocity in these plots.

Appendix C: APEX survey data

We provide a complete overview of the survey in Table C.1 and Fig. C.1.

To facilitate a direct comparison to the spectrum of IK Tau, Fig. C.1 also shows the IRAM 30 m observations (in orange) of Velilla Prieto et al. (2017). We multiply the IK Tau spectrum with a factor A to account for the difference in distance (d) and mass-loss rate ($\dot{M}$) between the two targets, and for the frequency-dependent difference in point-source sensitivity (σ_ν) between the two telescopes:

$$A = \frac{\dot{M}_{\rm RDor}}{\dot{M}_{\rm IKTau}} \times \left(\frac{d_{\rm RDor}}{d_{\rm IKTau}}\right)^{-2} \times \left(\frac{\sigma_{\nu,\rm APEX}}{\sigma_{\nu,\rm IRAM}}\right)^{-1} = 0.65 \times \left(\frac{\sigma_{\nu,\rm APEX}}{\sigma_{\nu,\rm IRAM}}\right)^{-1}. \quad \text{(C.1)}$$

The distances and mass-loss rates are those reported by Maercker et al. (2016). The point-source sensitivities $\sigma_{\nu,\rm APEX}$ are those listed in Sect. 2; the values for $\sigma_{\nu,\rm IRAM}$ are taken from Velilla Prieto et al. (2017).

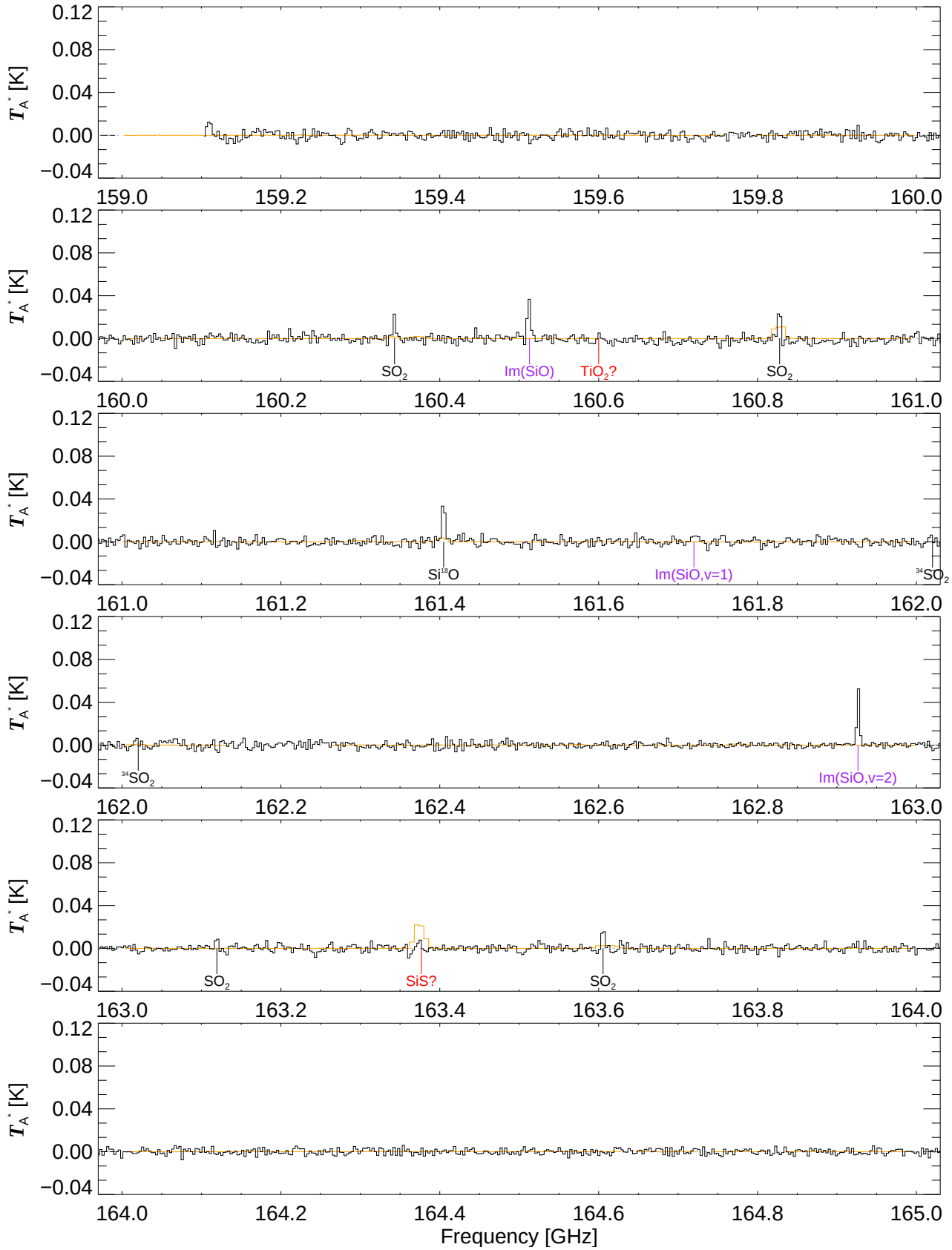

Fig. C.1. APEX line survey of R Dor (black). Labels show the carrier molecule of the indicated emission. Red labels indicate tentative or unidentified detections. Purple labels (Im(...)) pertain to emission contaminating the signal from the image sideband (see Sect. 2). For visibility, some parts of the survey were rescaled to fit the vertical scale. The colour coding of the spectrum corresponds to the following scale factors: (black) 1; (green) 1/5; (blue) 1/25; (red) 1/125. Note the gap in the range 321.5–328.0 GHz. We also show the IRAM 30 m survey of IK Tau (orange; Velilla Prieto et al. 2017) for direct comparison of the two data sets. The IK Tau spectrum has been scaled according to the description in Appendix C.

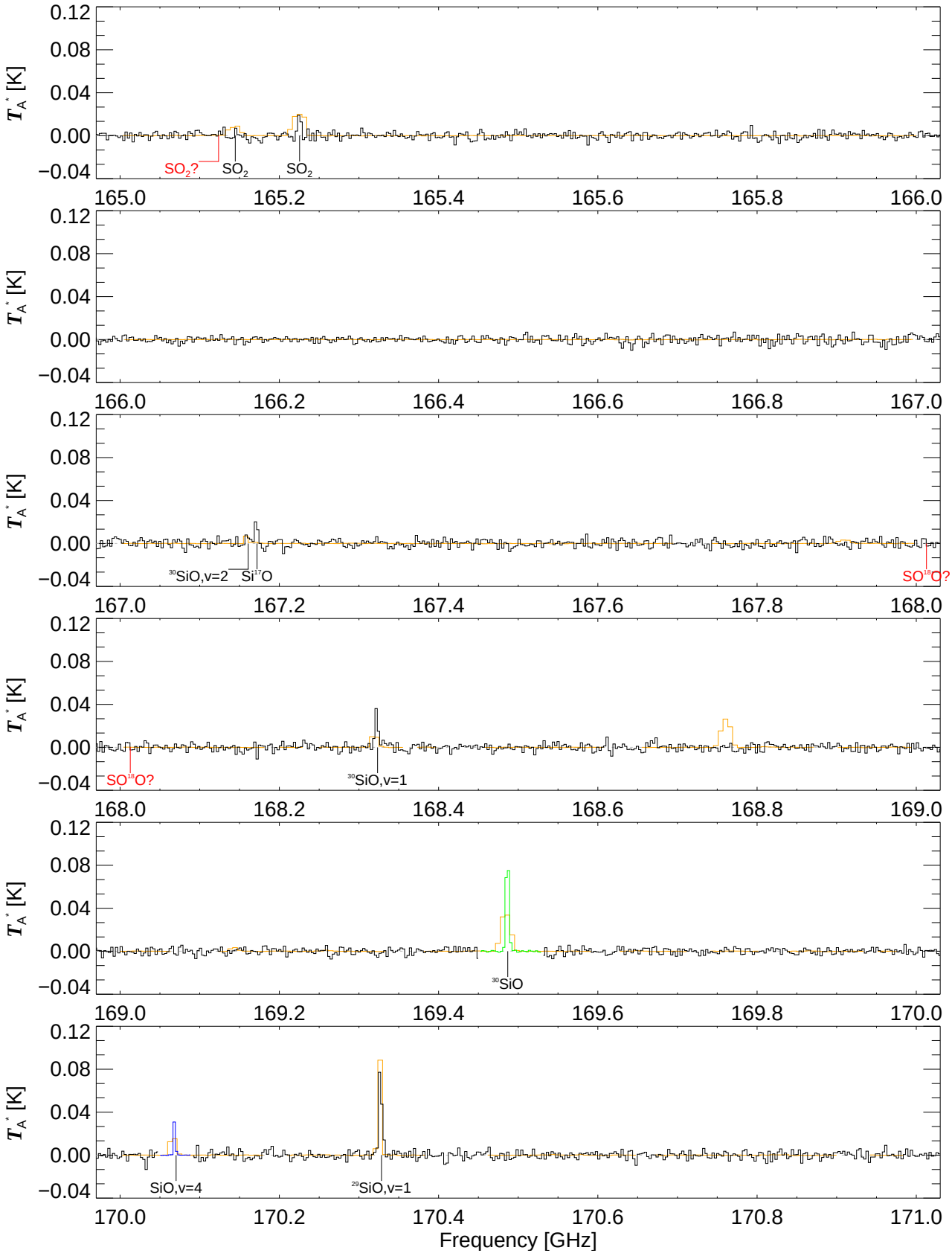

Fig. C.1. continued.

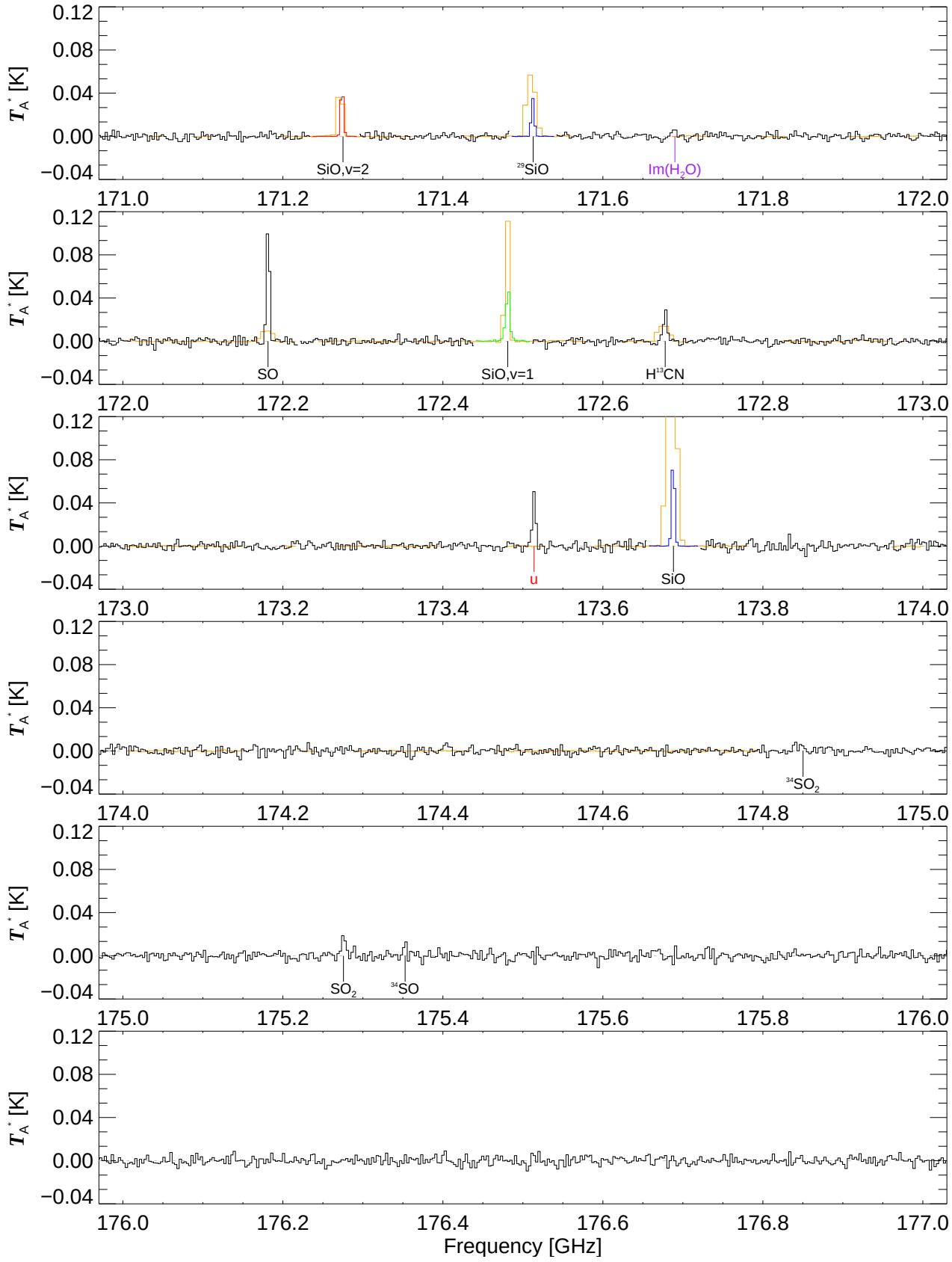

Fig. C.1. continued.

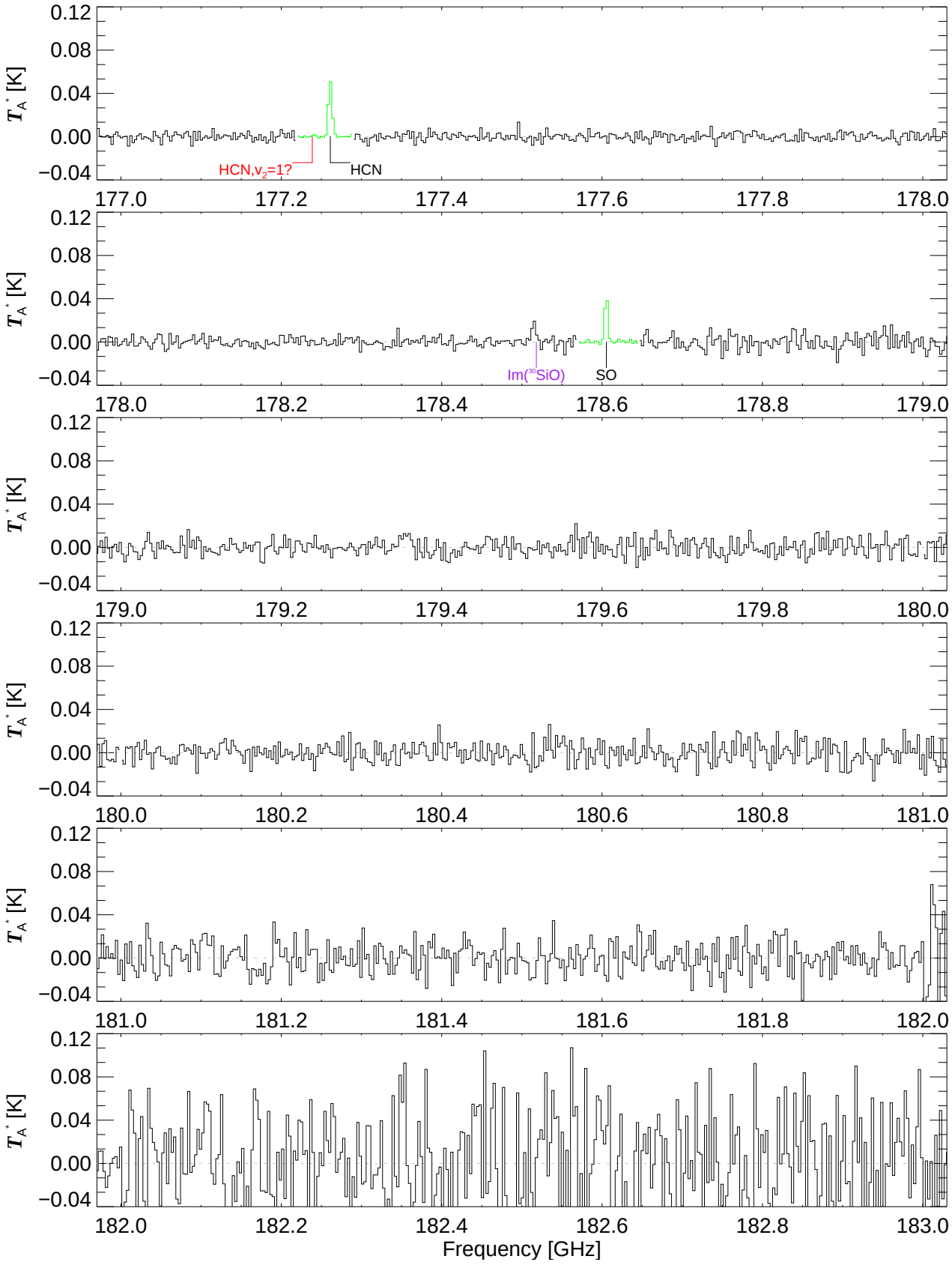

Fig. C.1. continued.

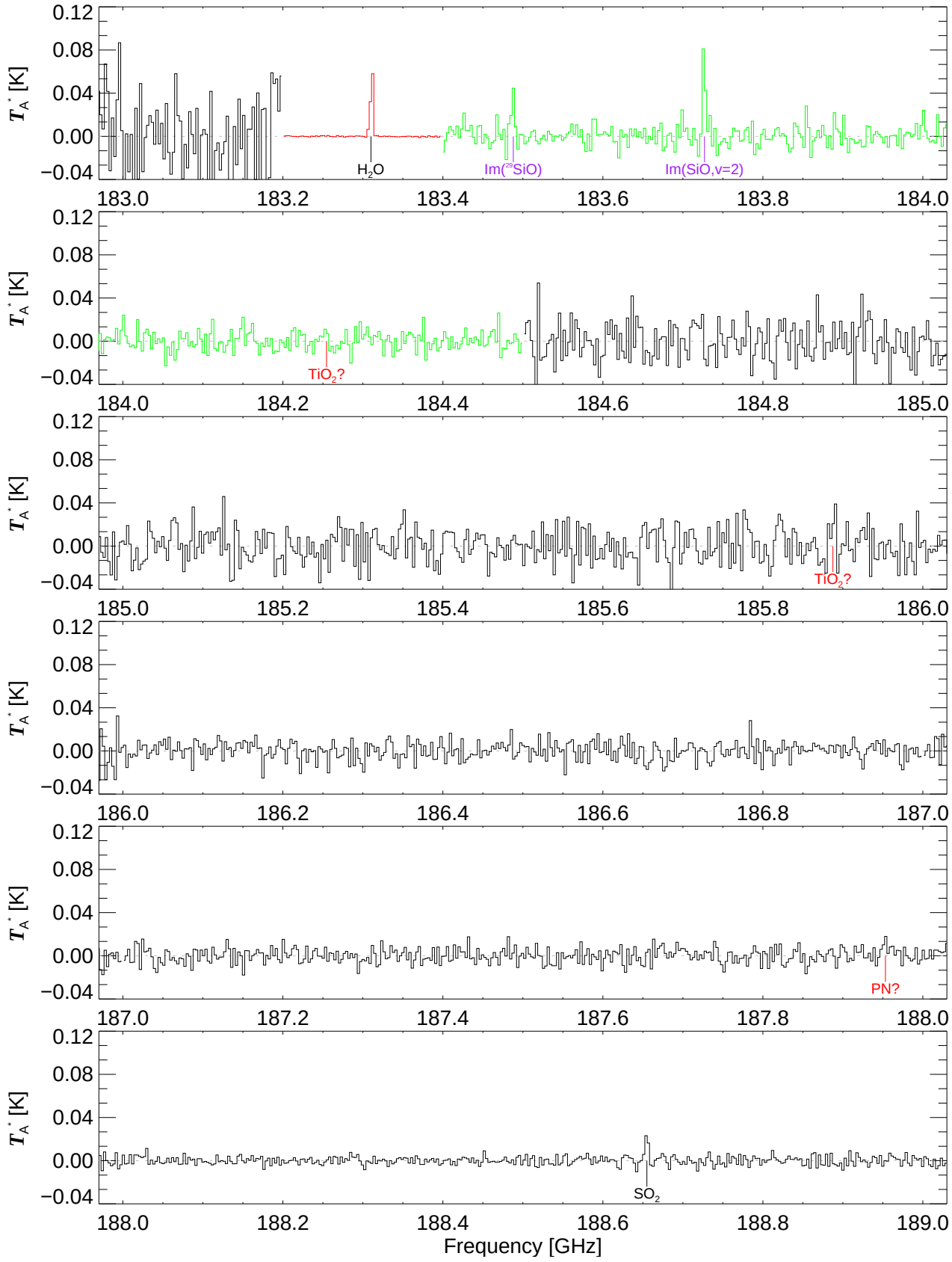

Fig. C.1. continued.

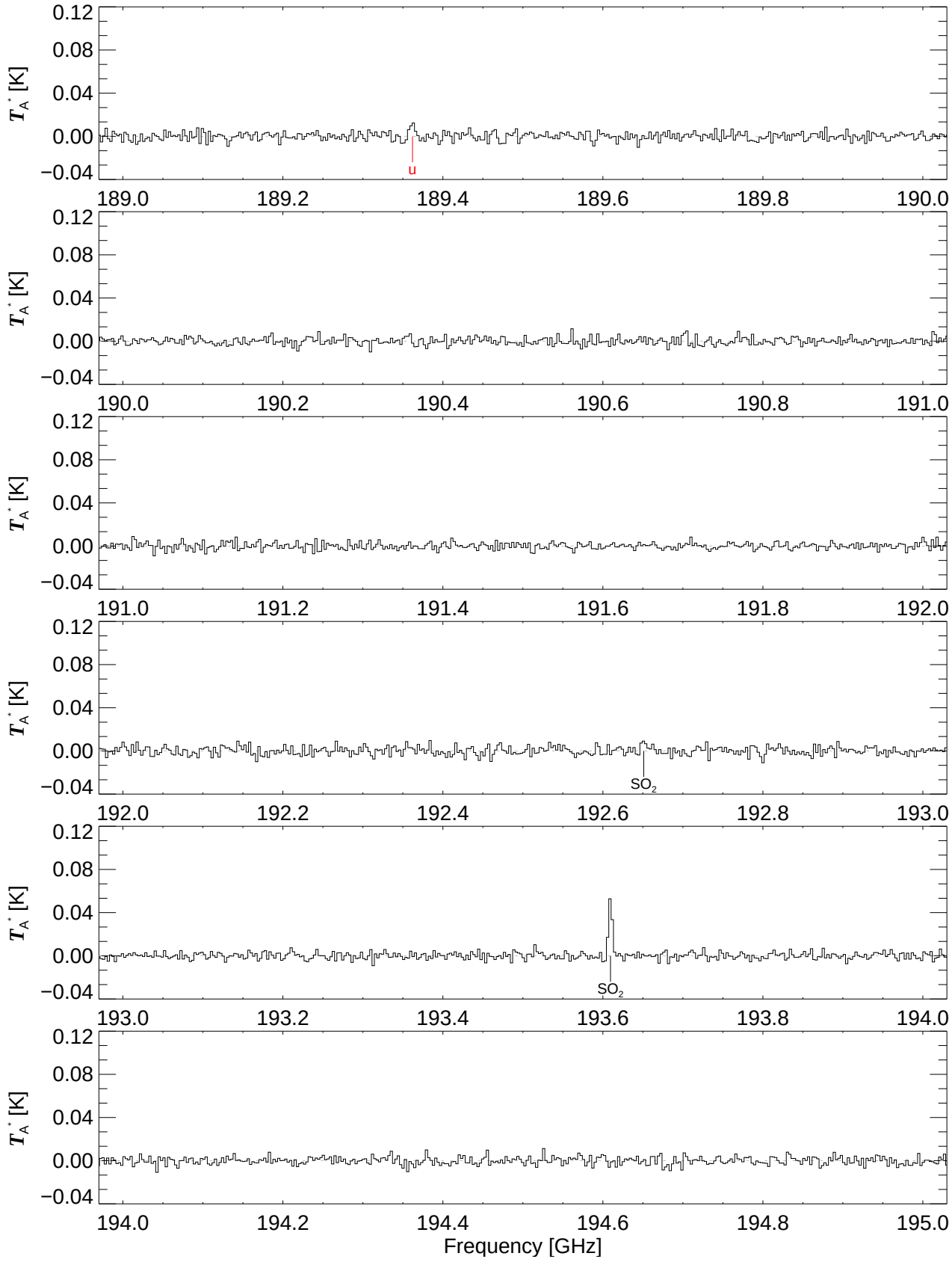

Fig. C.1. continued.

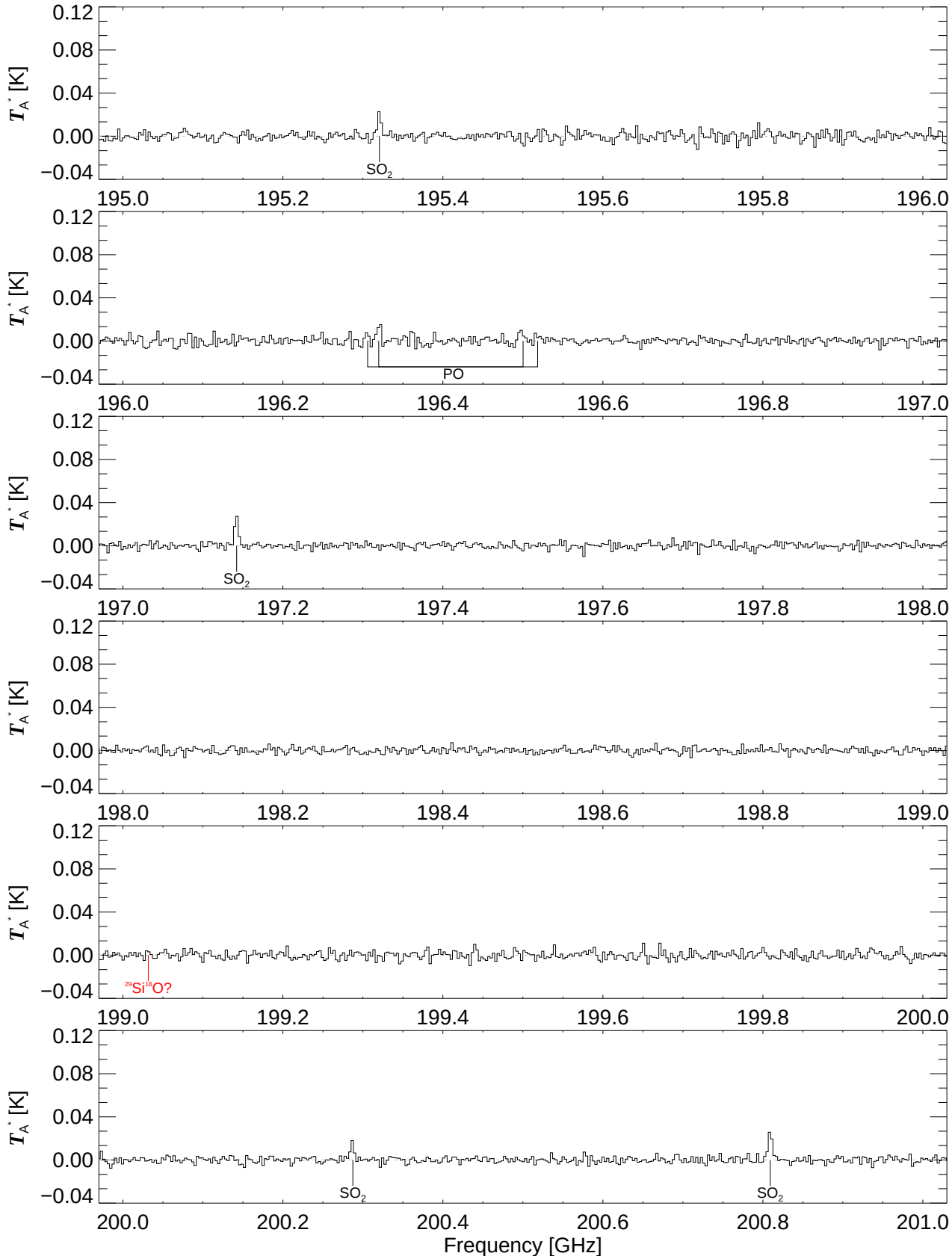

Fig. C.1. continued.

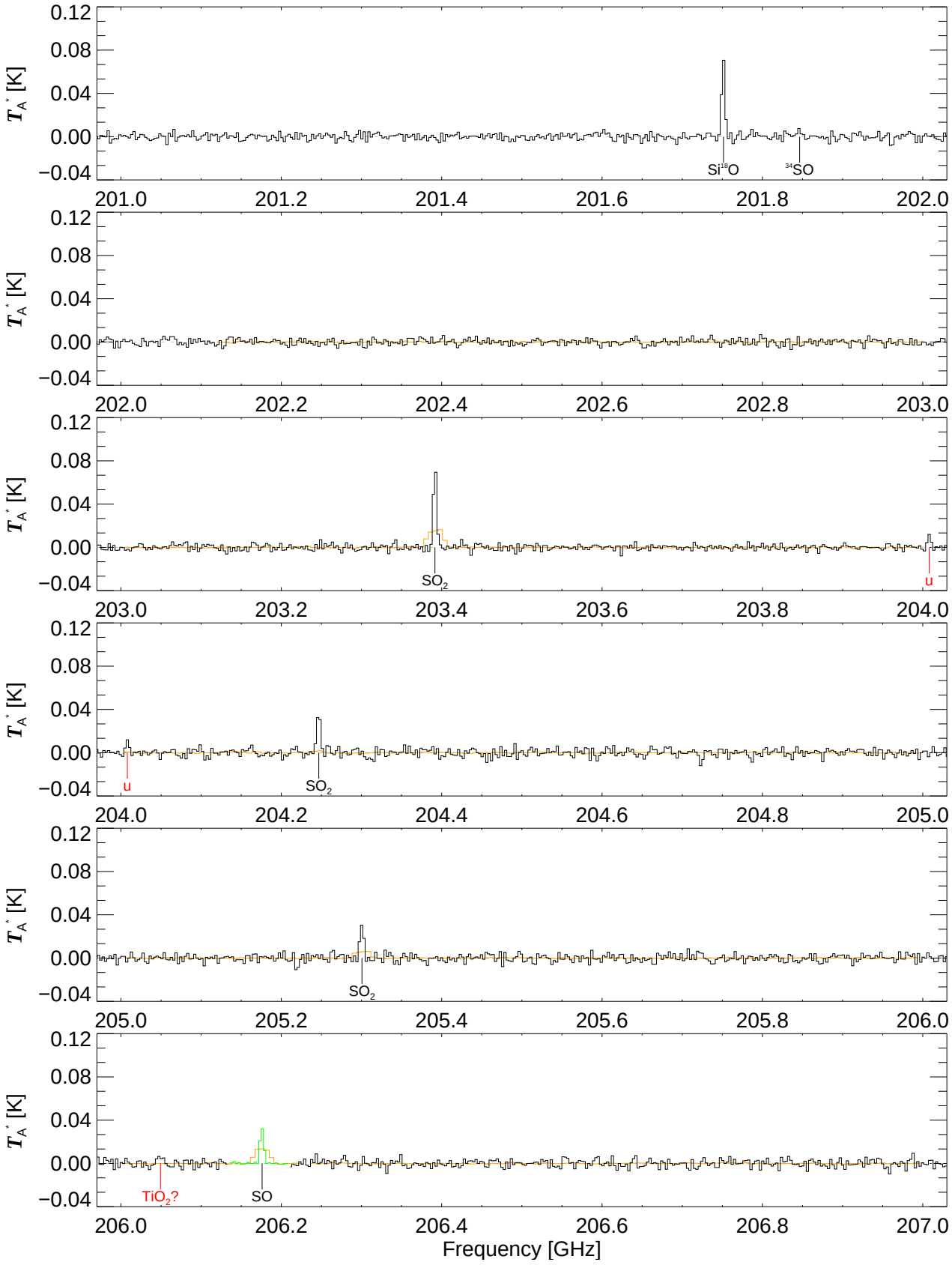

Fig. C.1. continued.

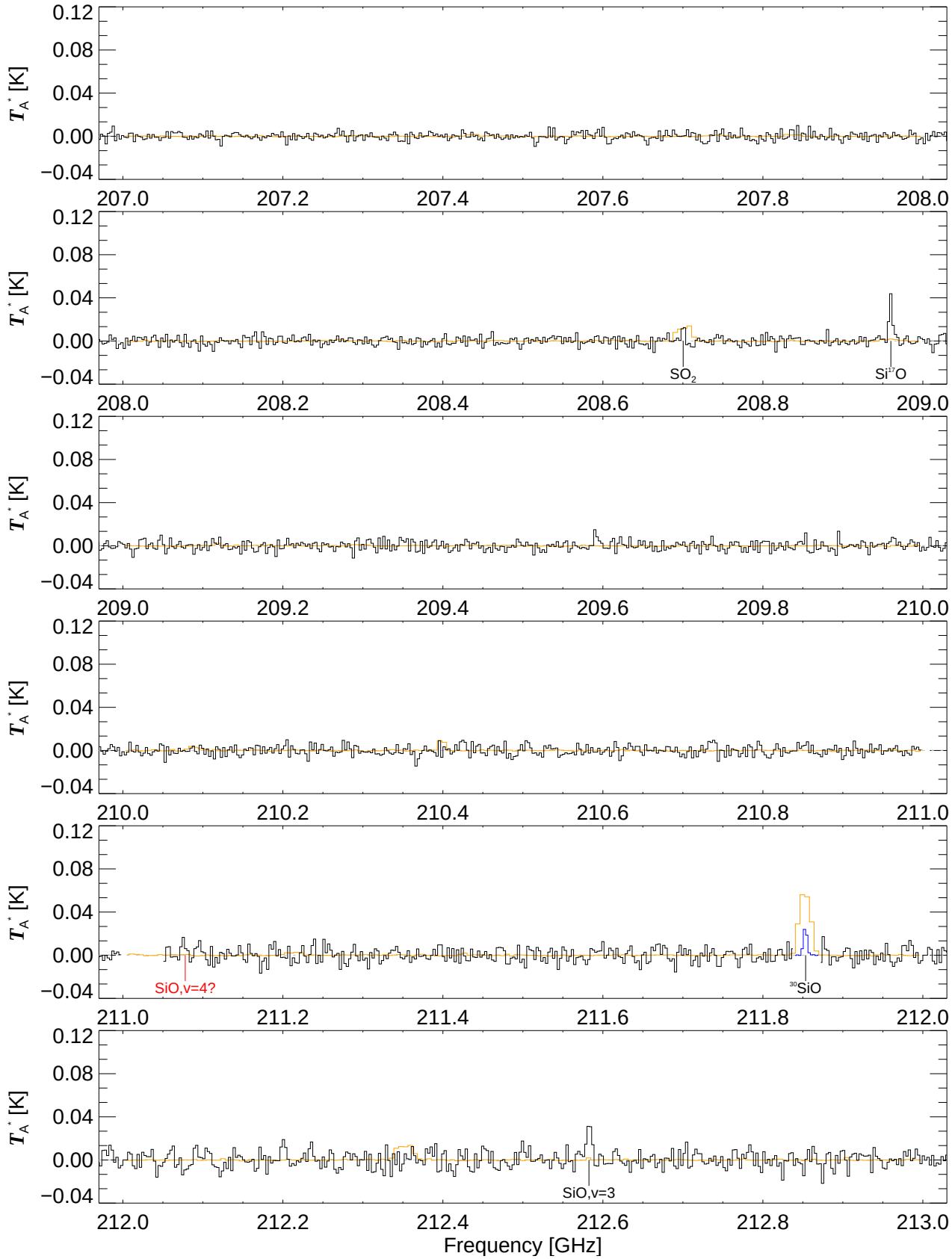

Fig. C.1. continued.

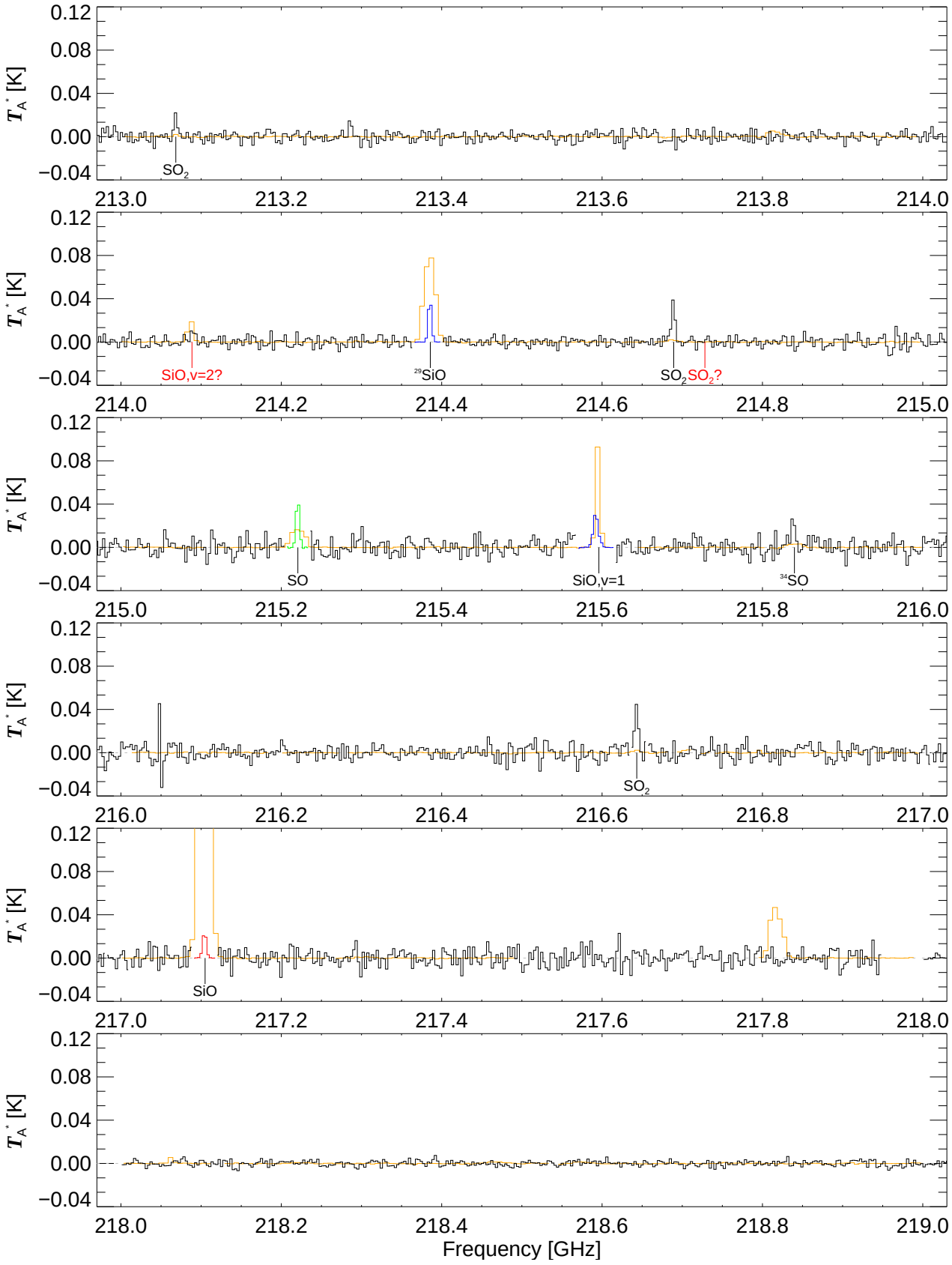

Fig. C.1. continued.

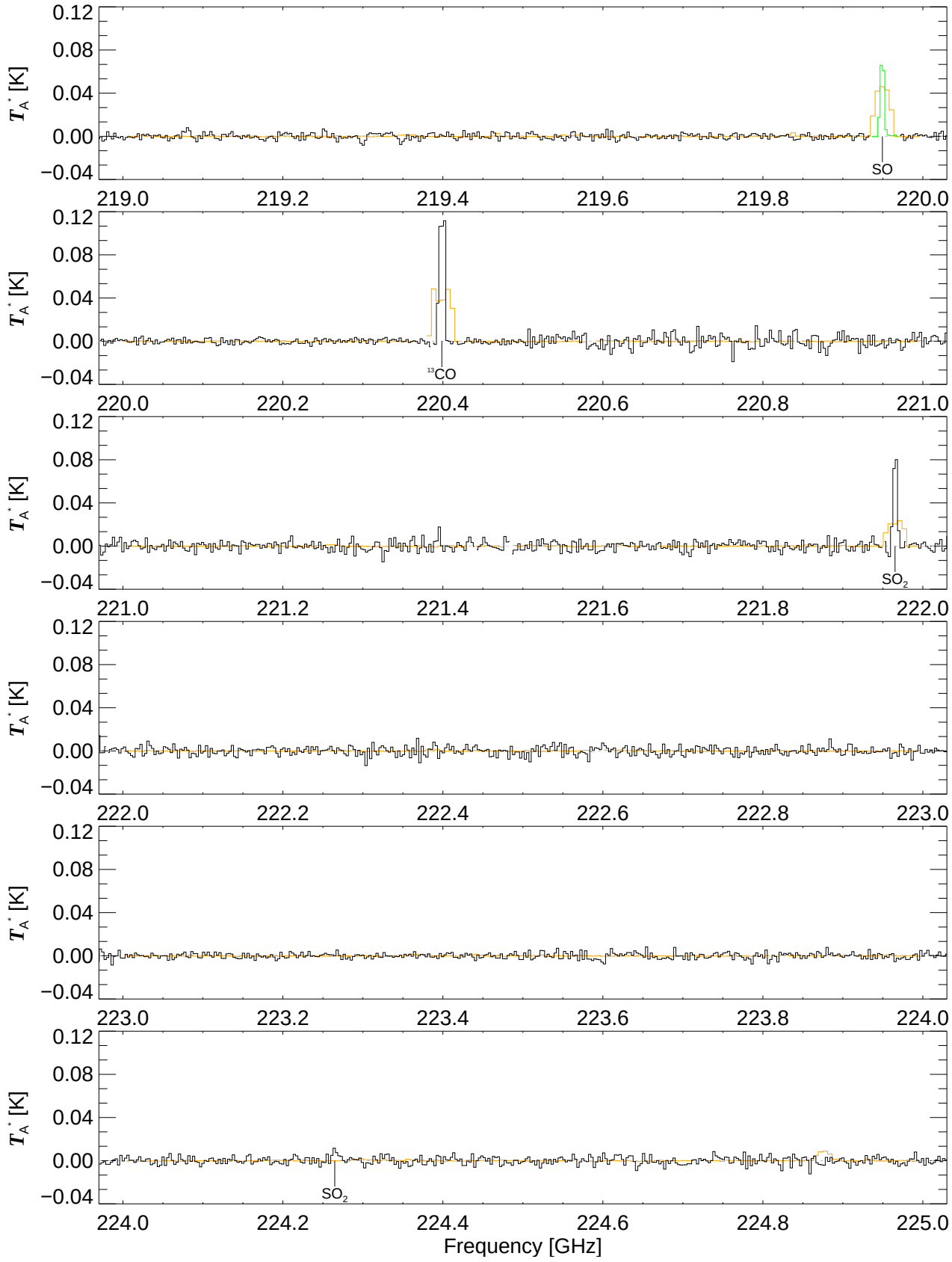

Fig. C.1. continued.

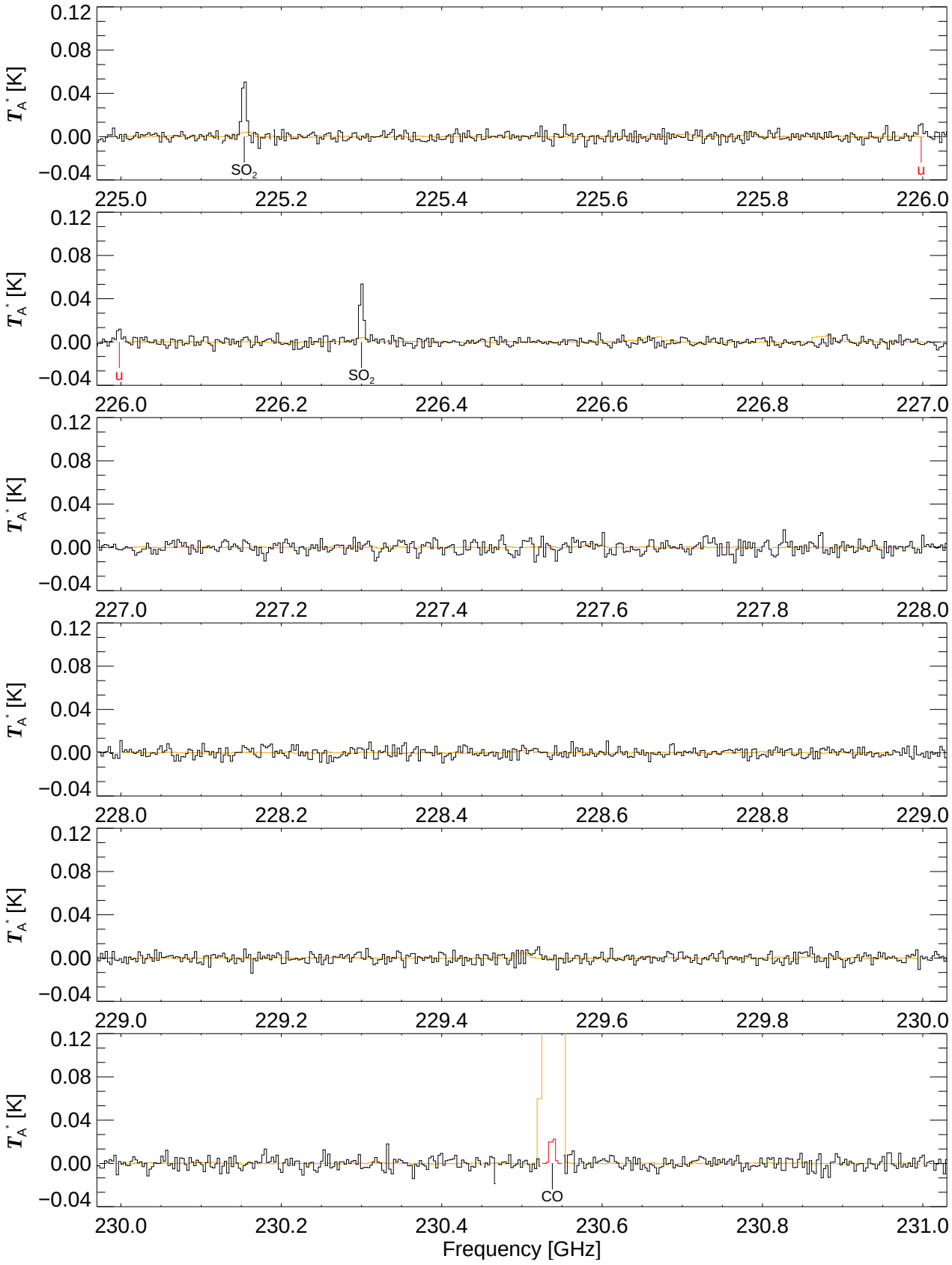

Fig. C.1. continued.

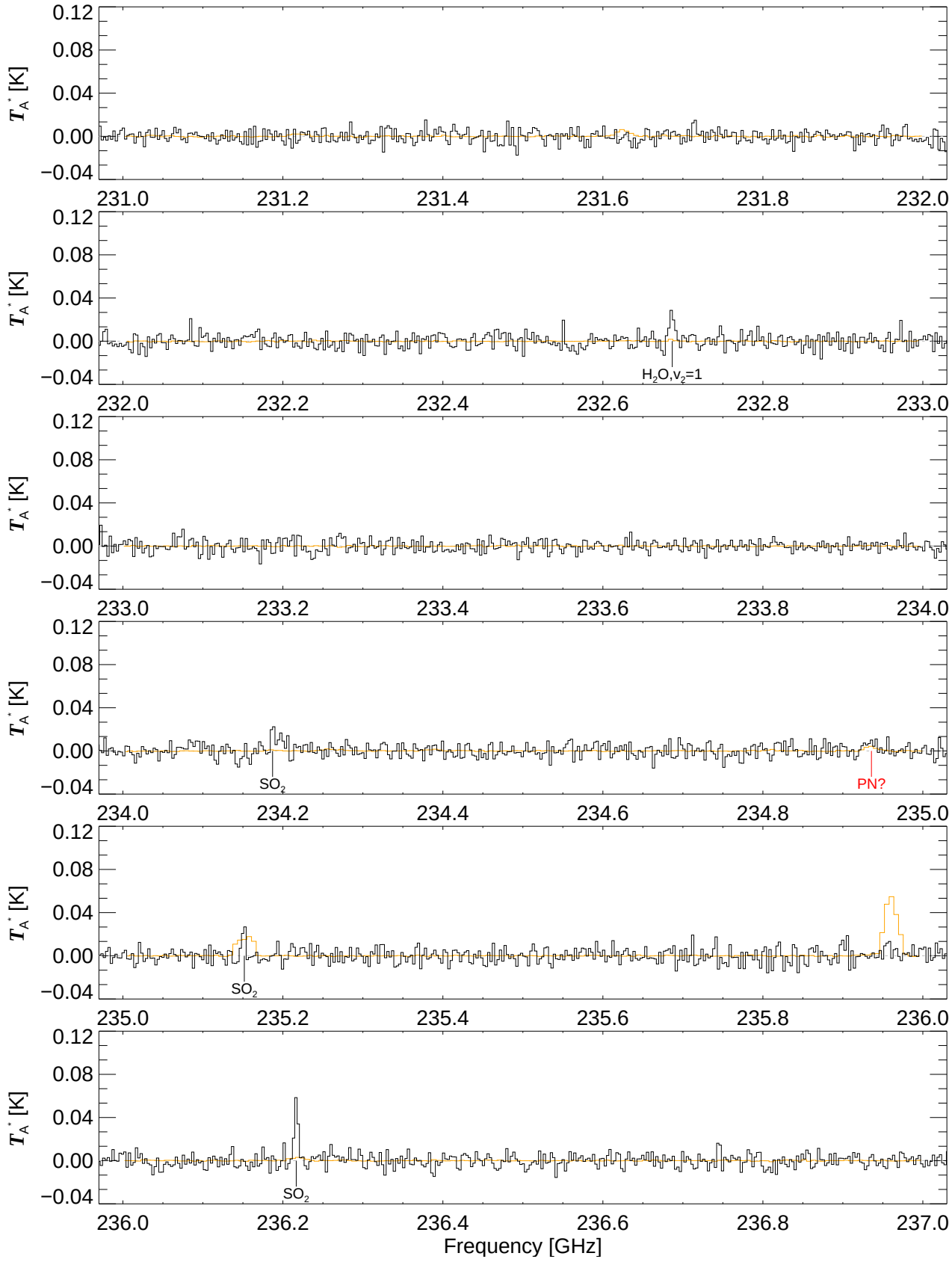

Fig. C.1. continued.

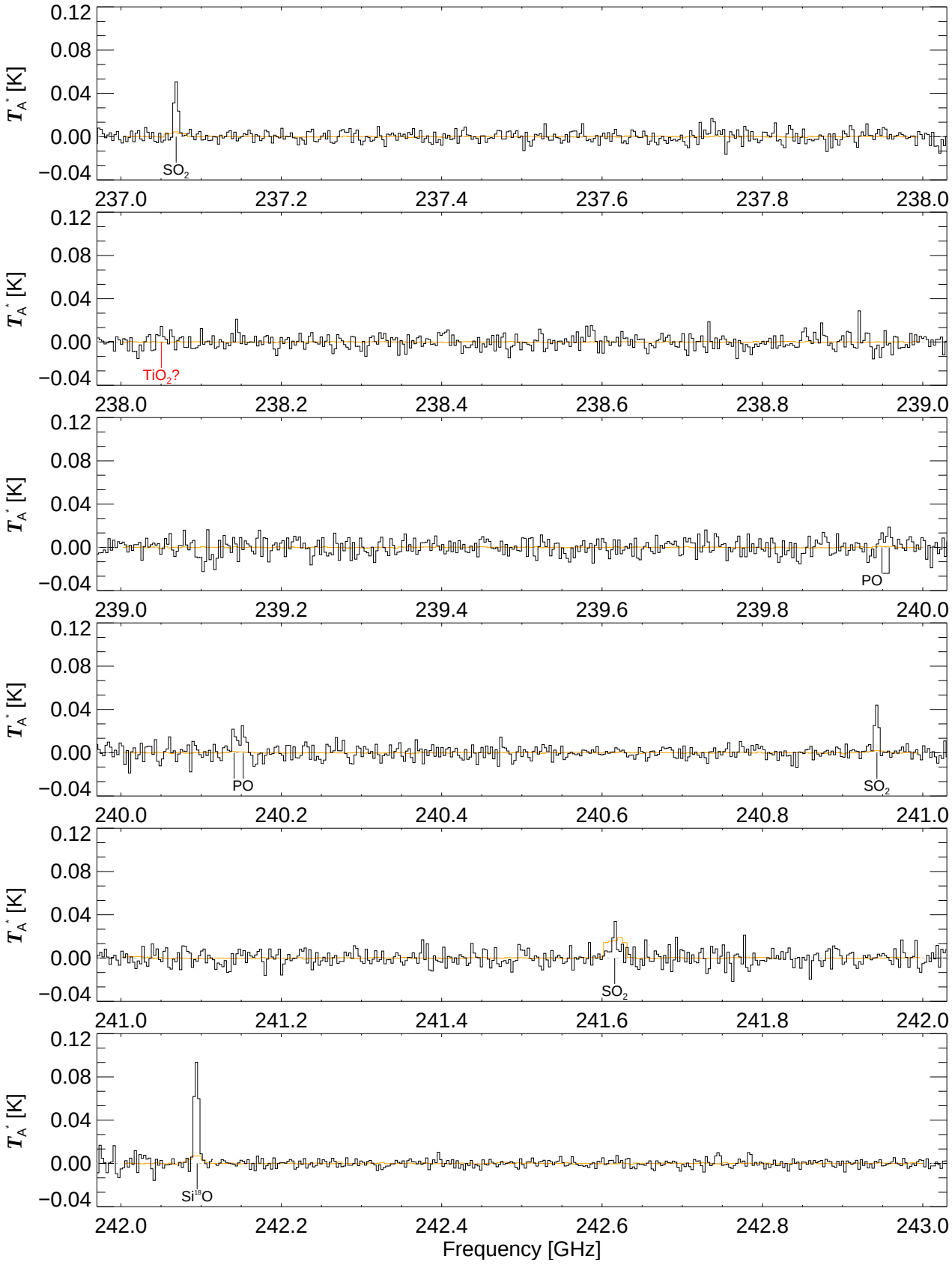

Fig. C.1. continued.

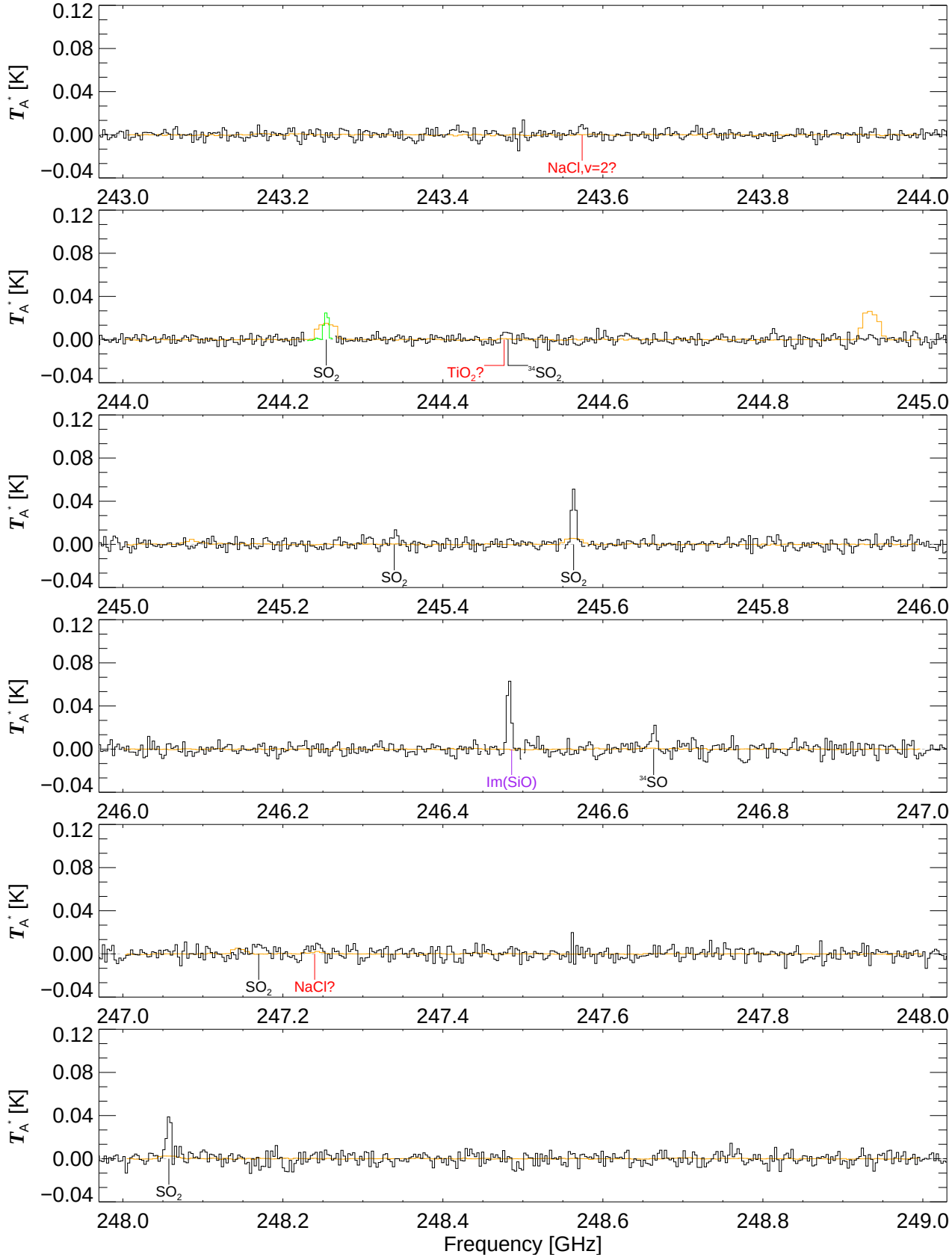

Fig. C.1. continued.

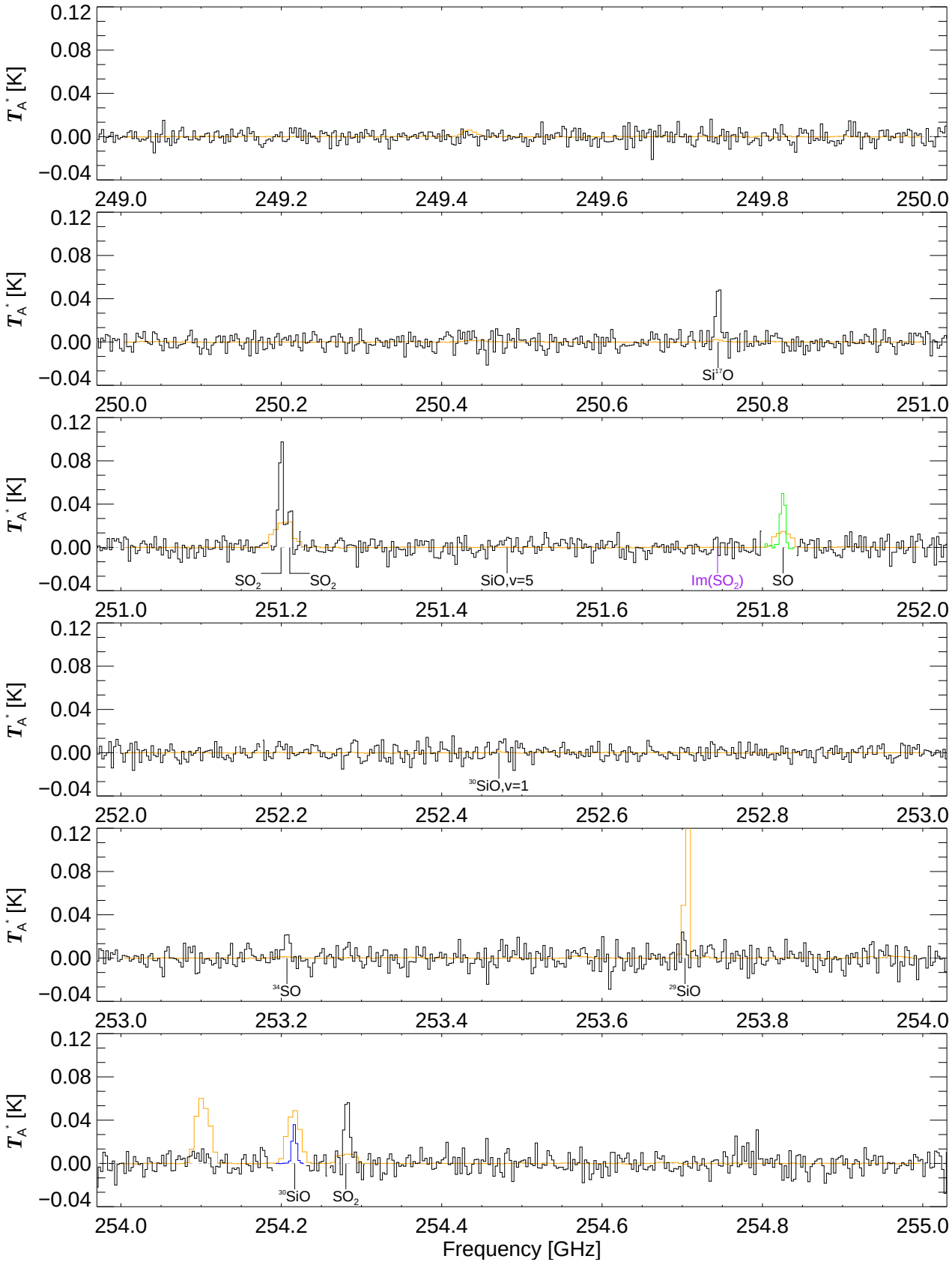

Fig. C.1. continued.

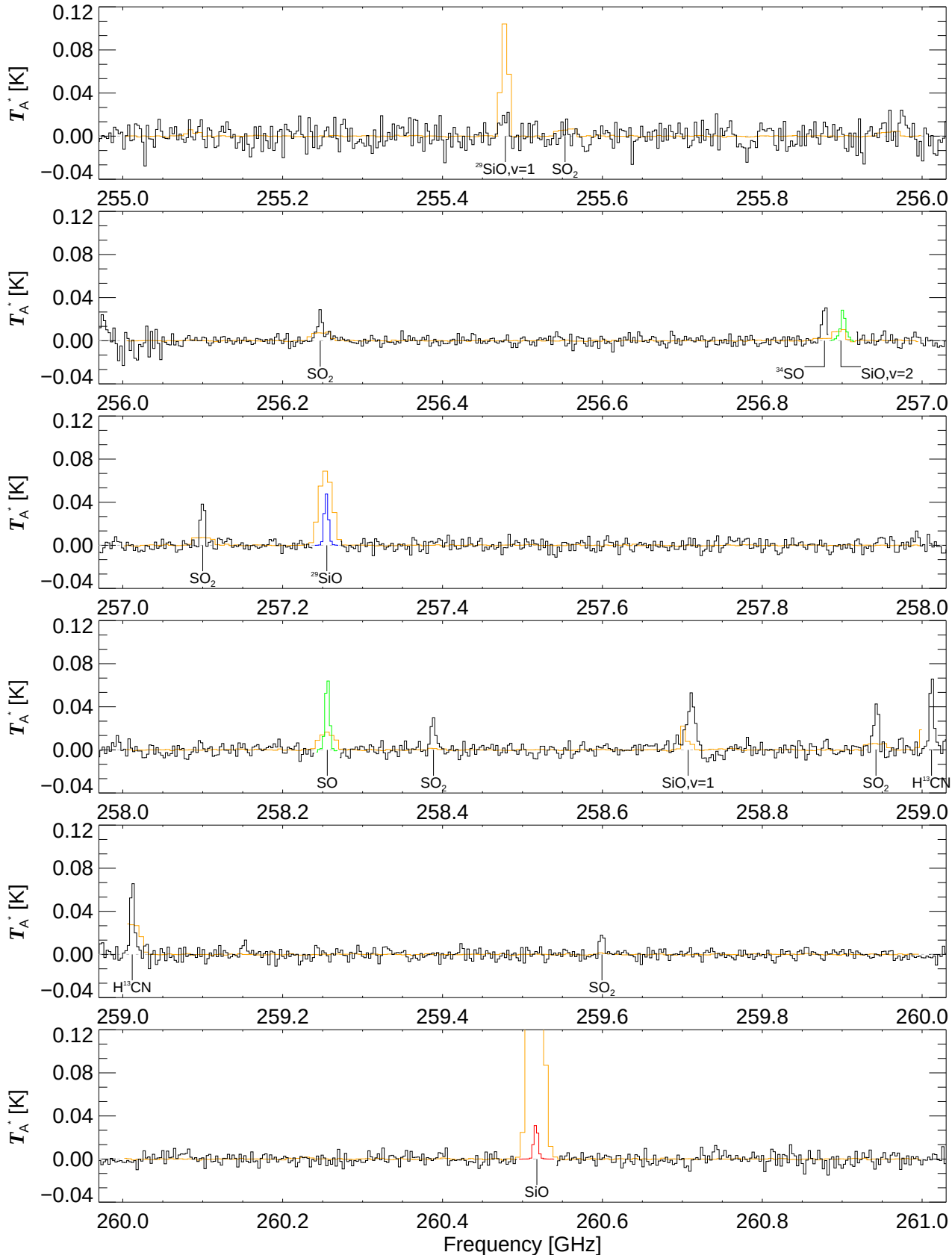

Fig. C.1. continued.

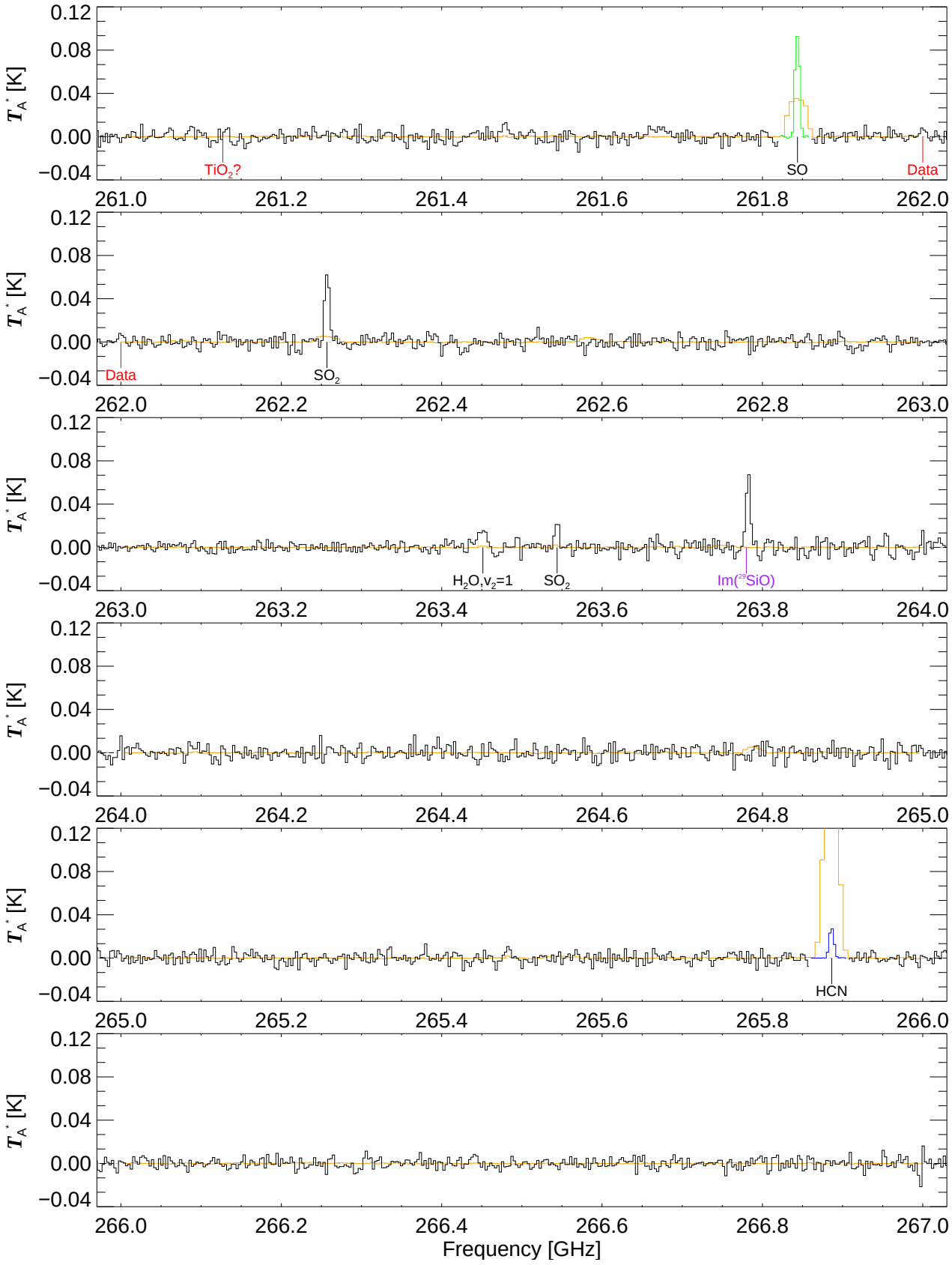

Fig. C.1. continued.

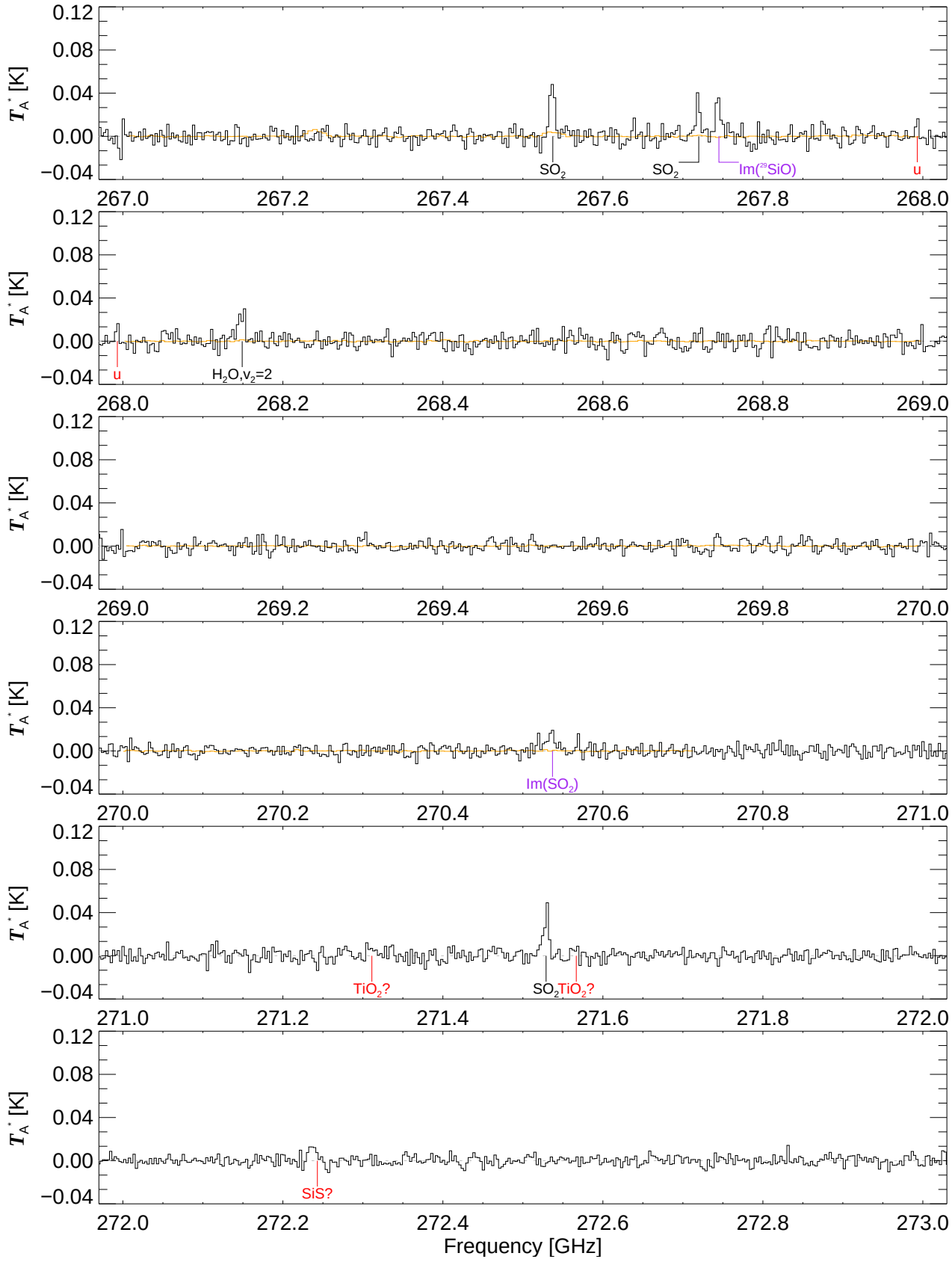

Fig. C.1. continued.

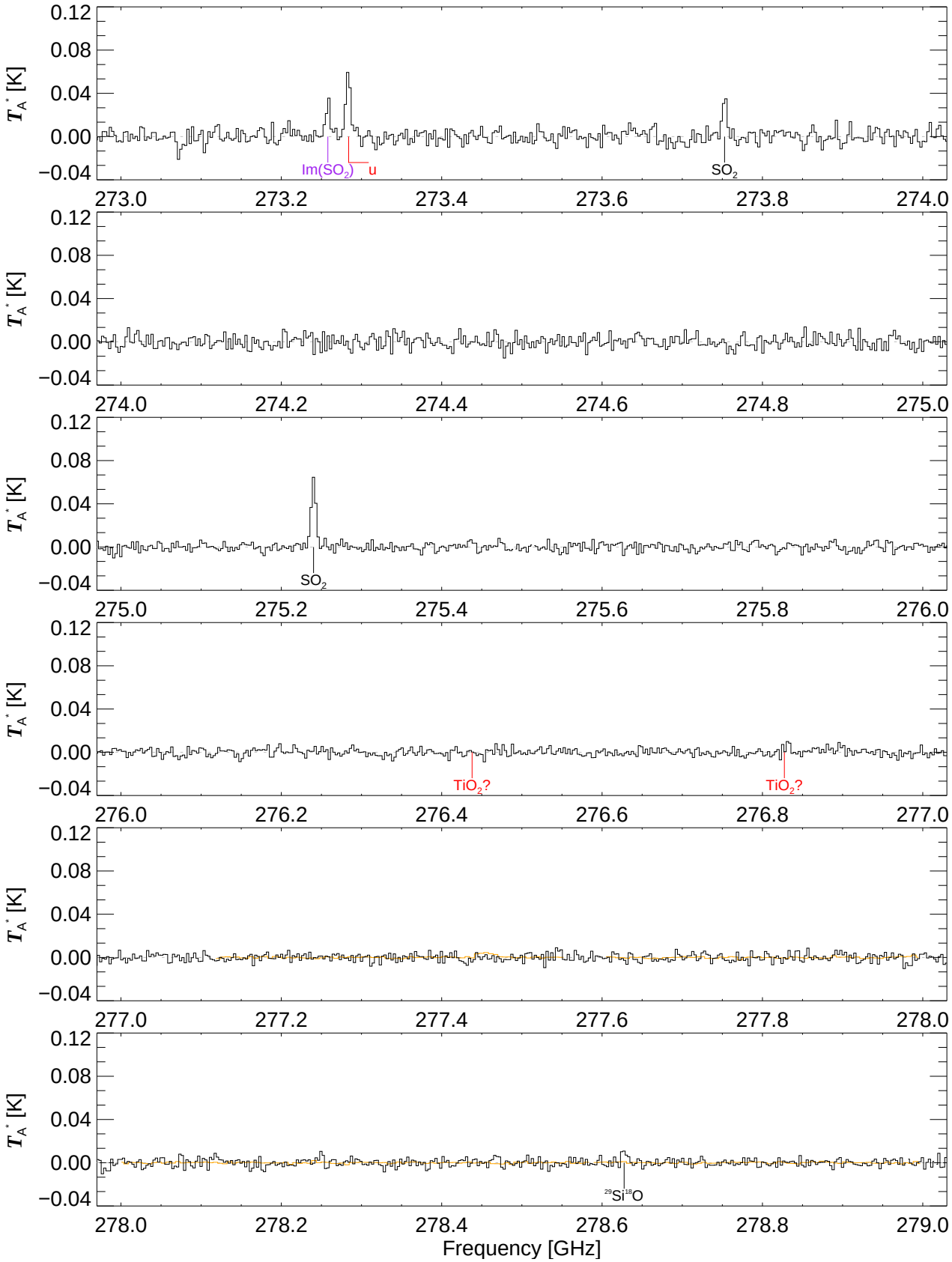

Fig. C.1. continued.

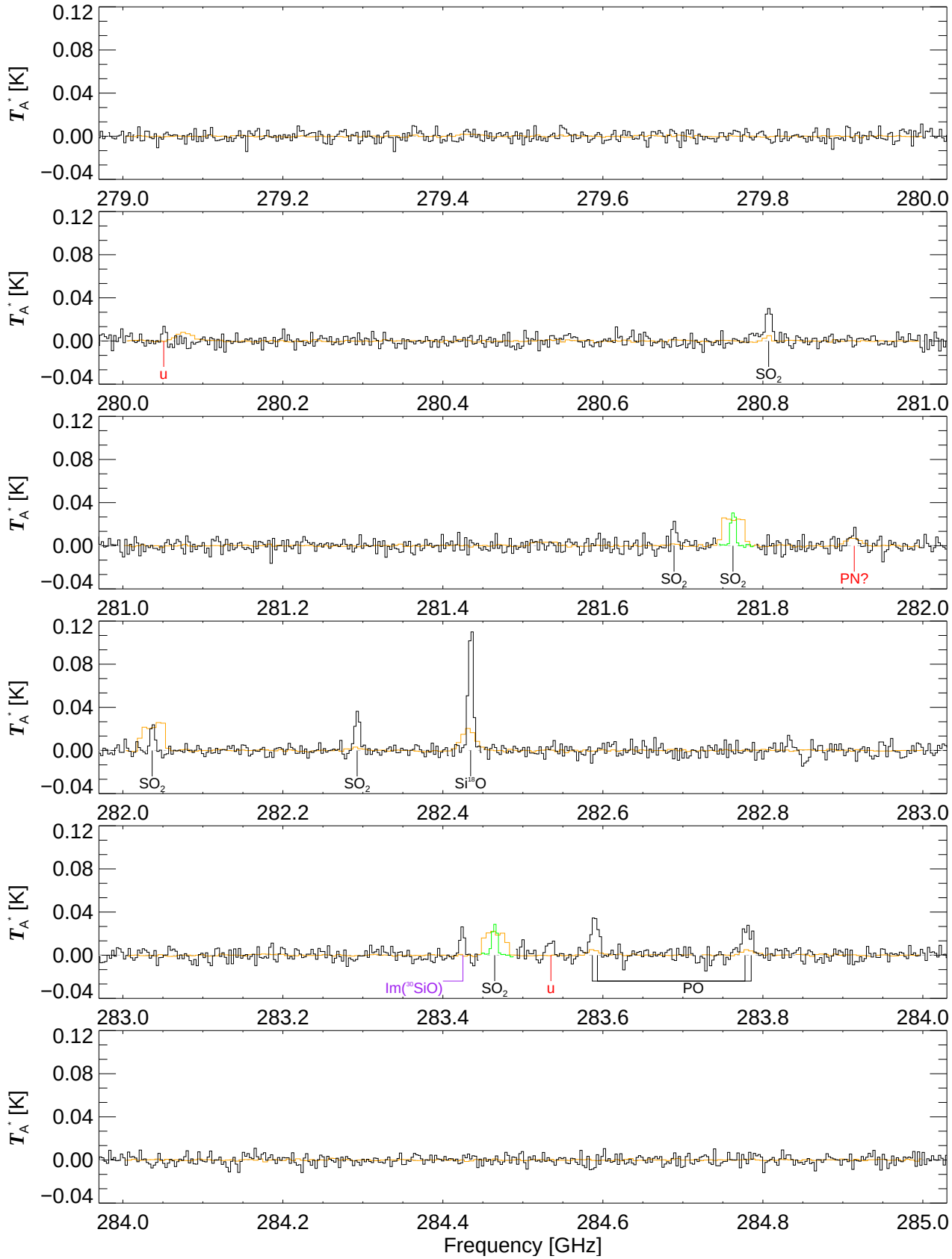

Fig. C.1. continued.

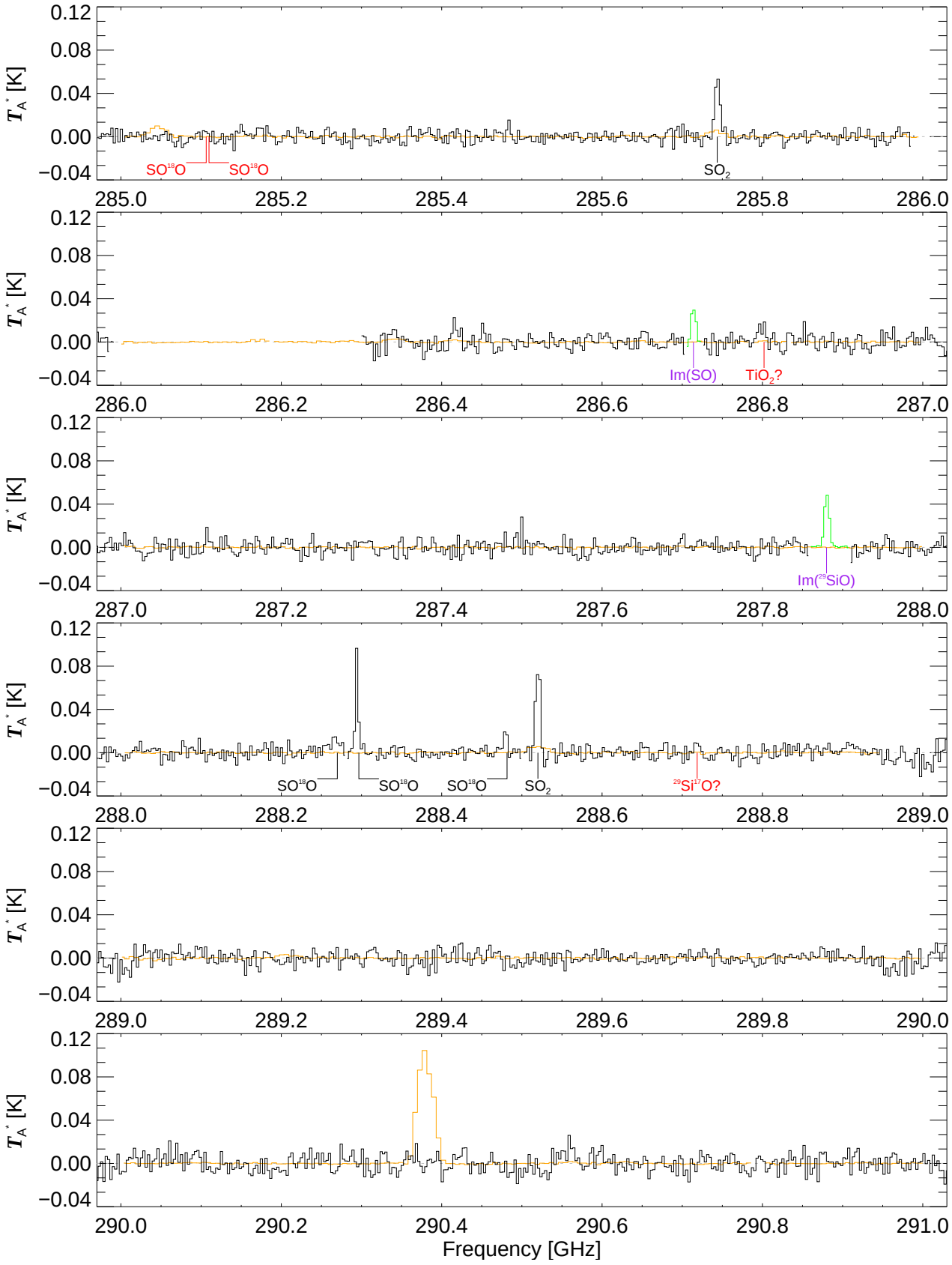

Fig. C.1. continued.

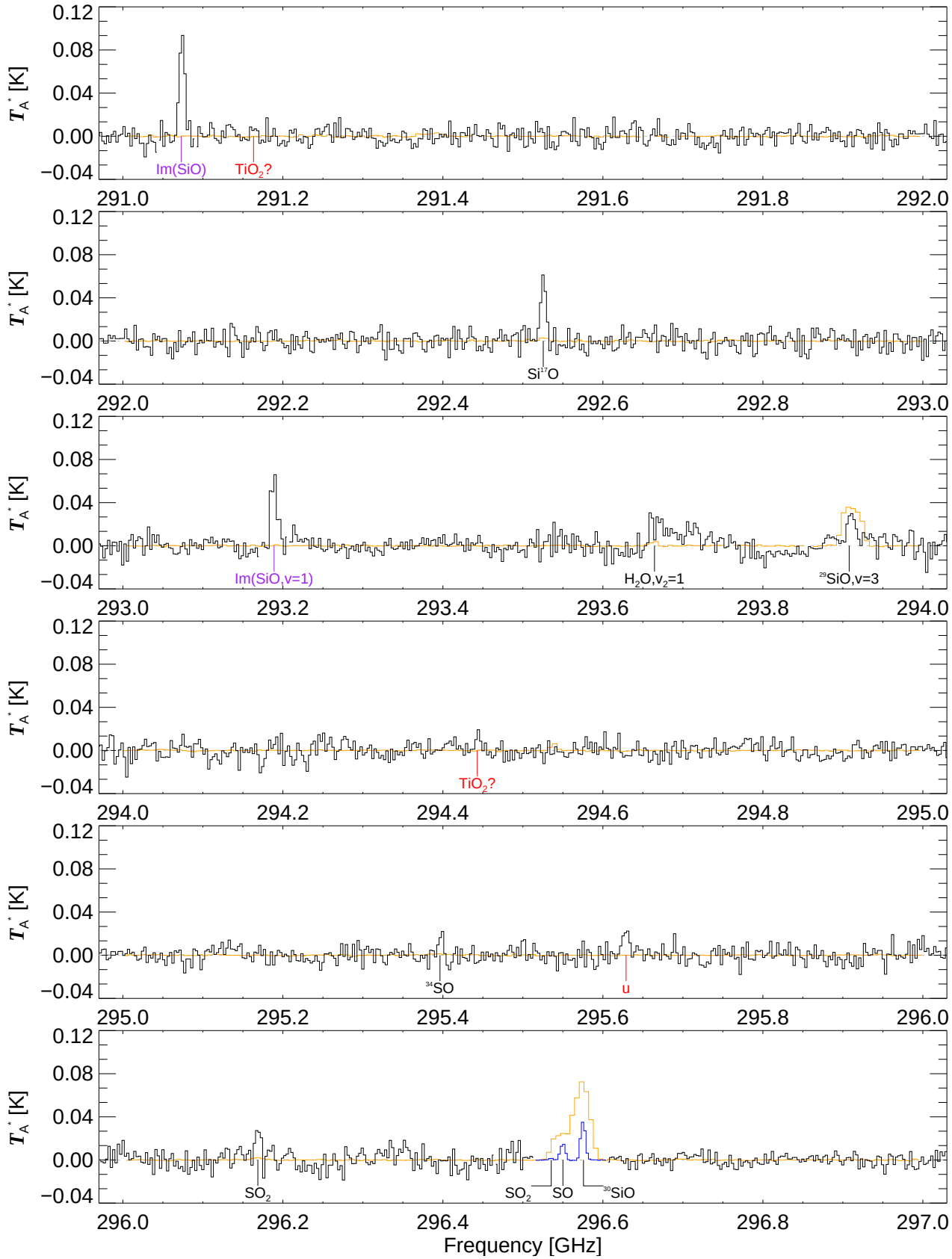

Fig. C.1. continued.

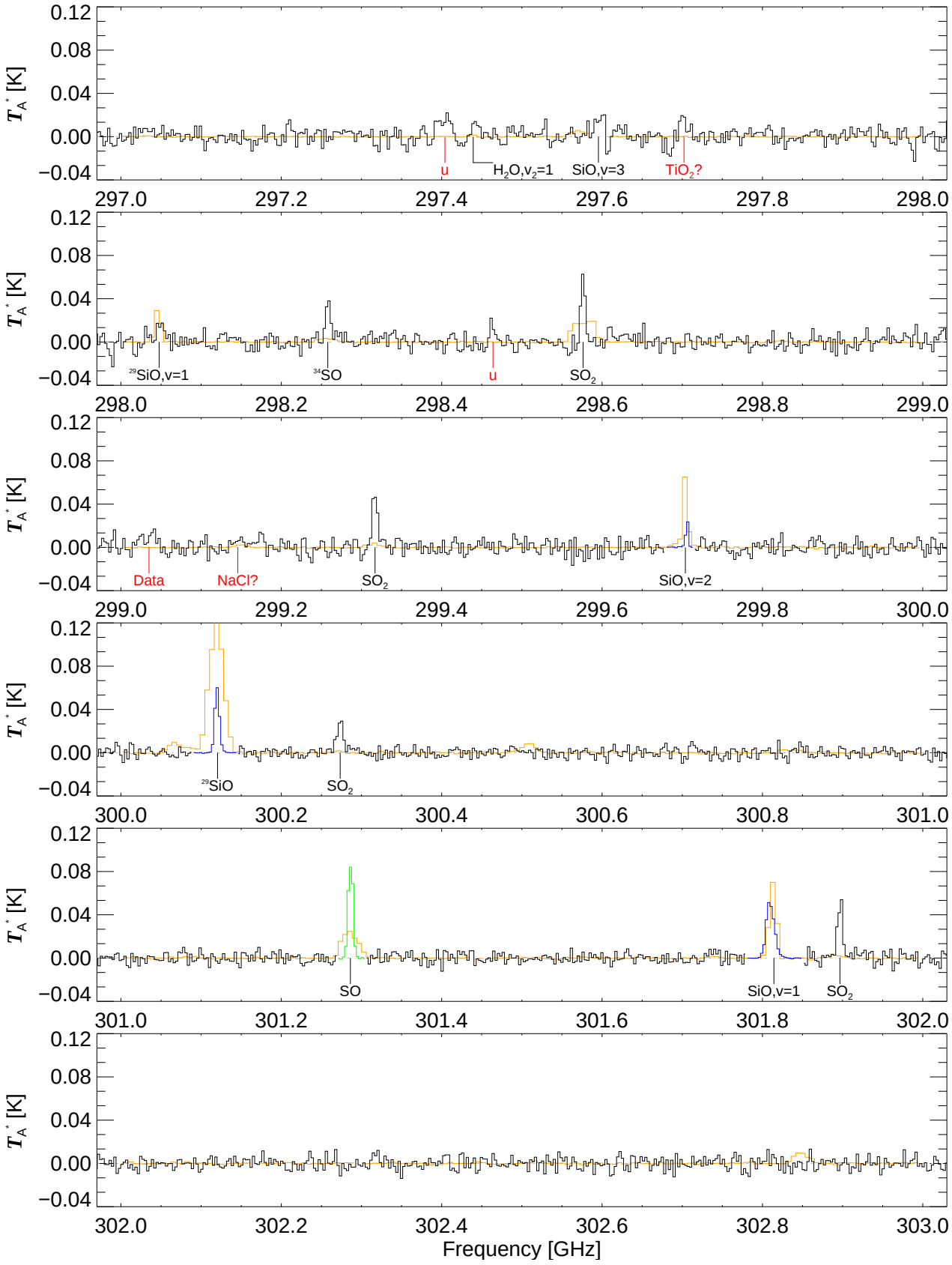

Fig. C.1. continued.

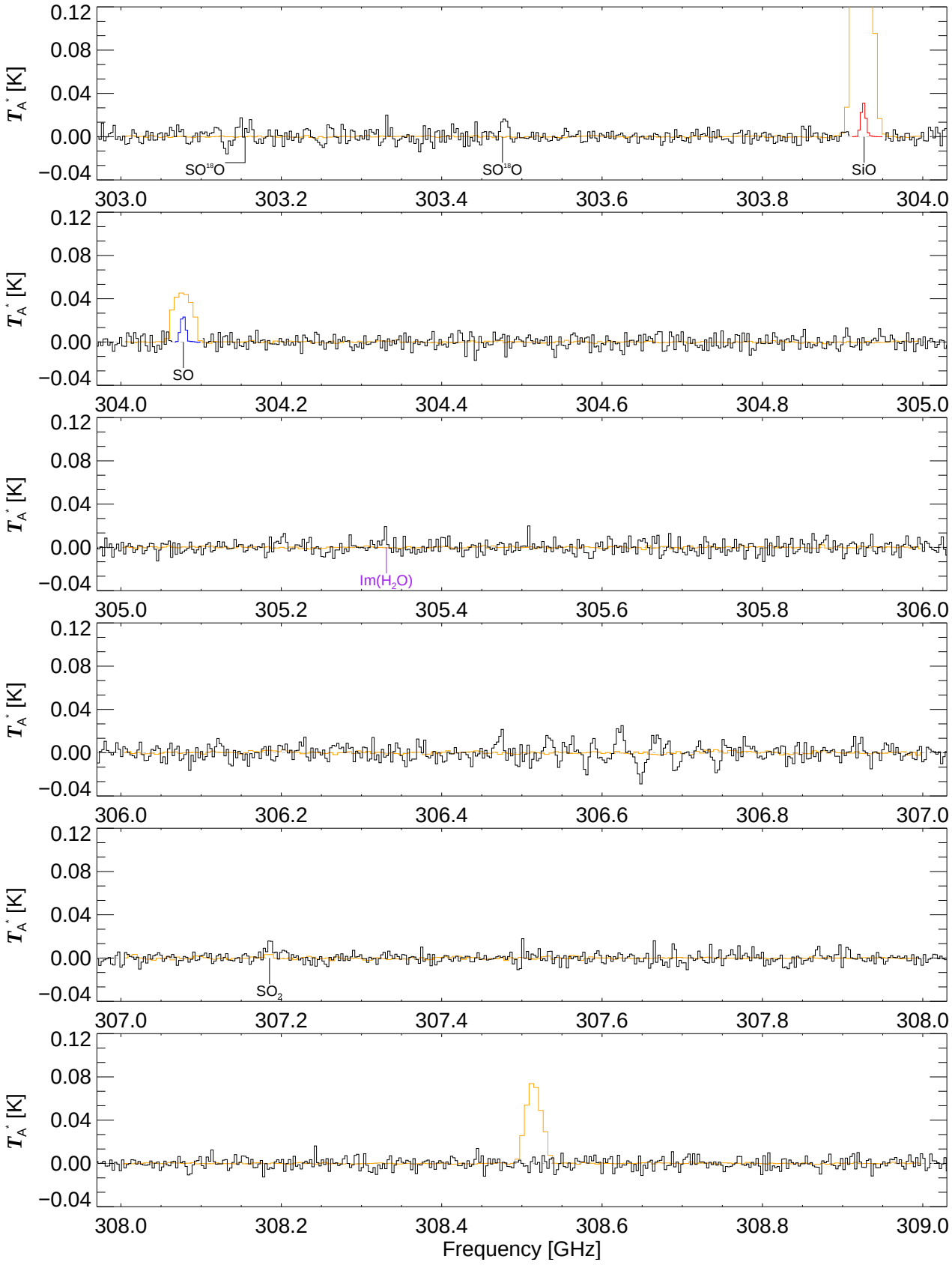

Fig. C.1. continued.

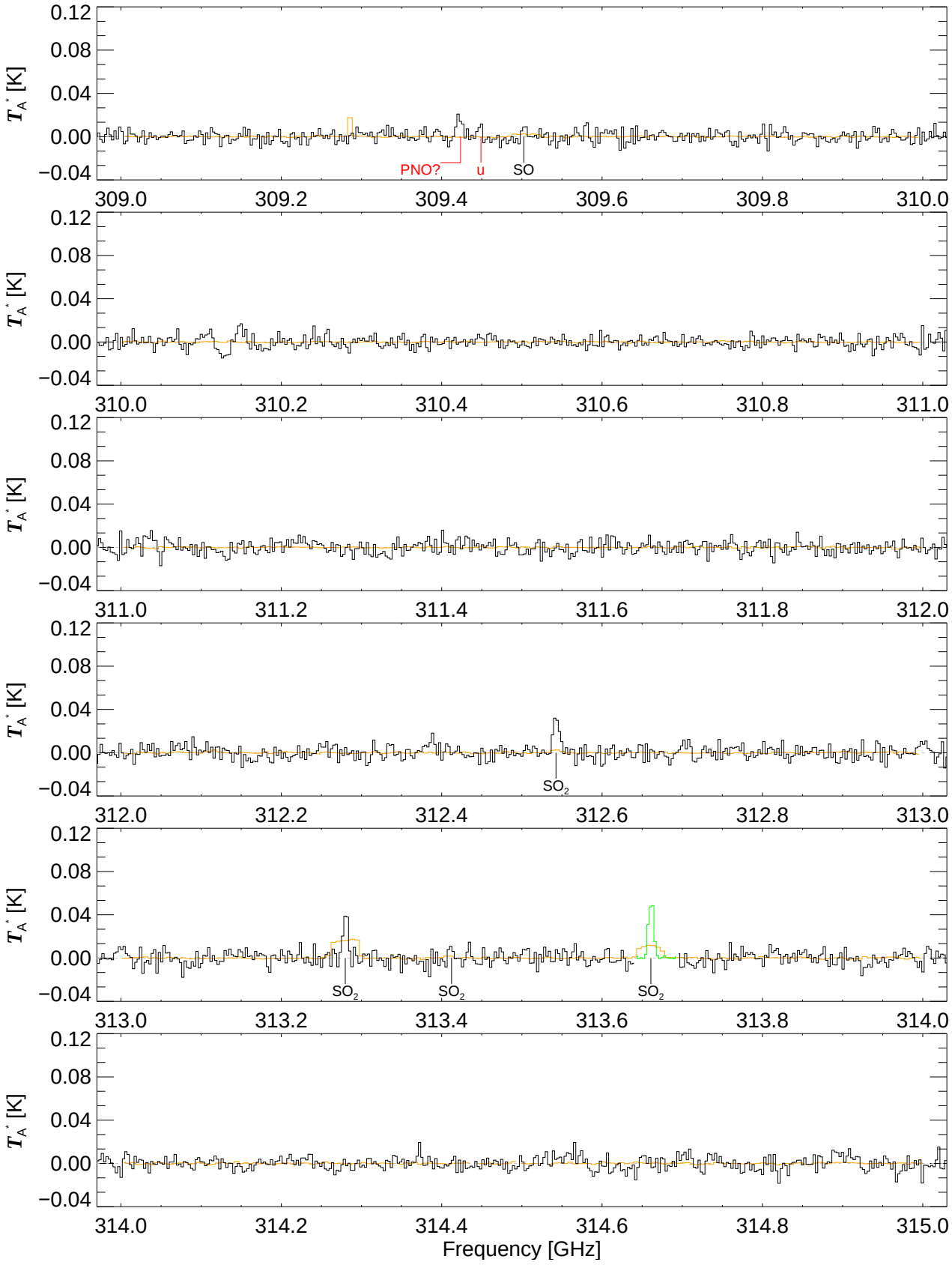

Fig. C.1. continued.

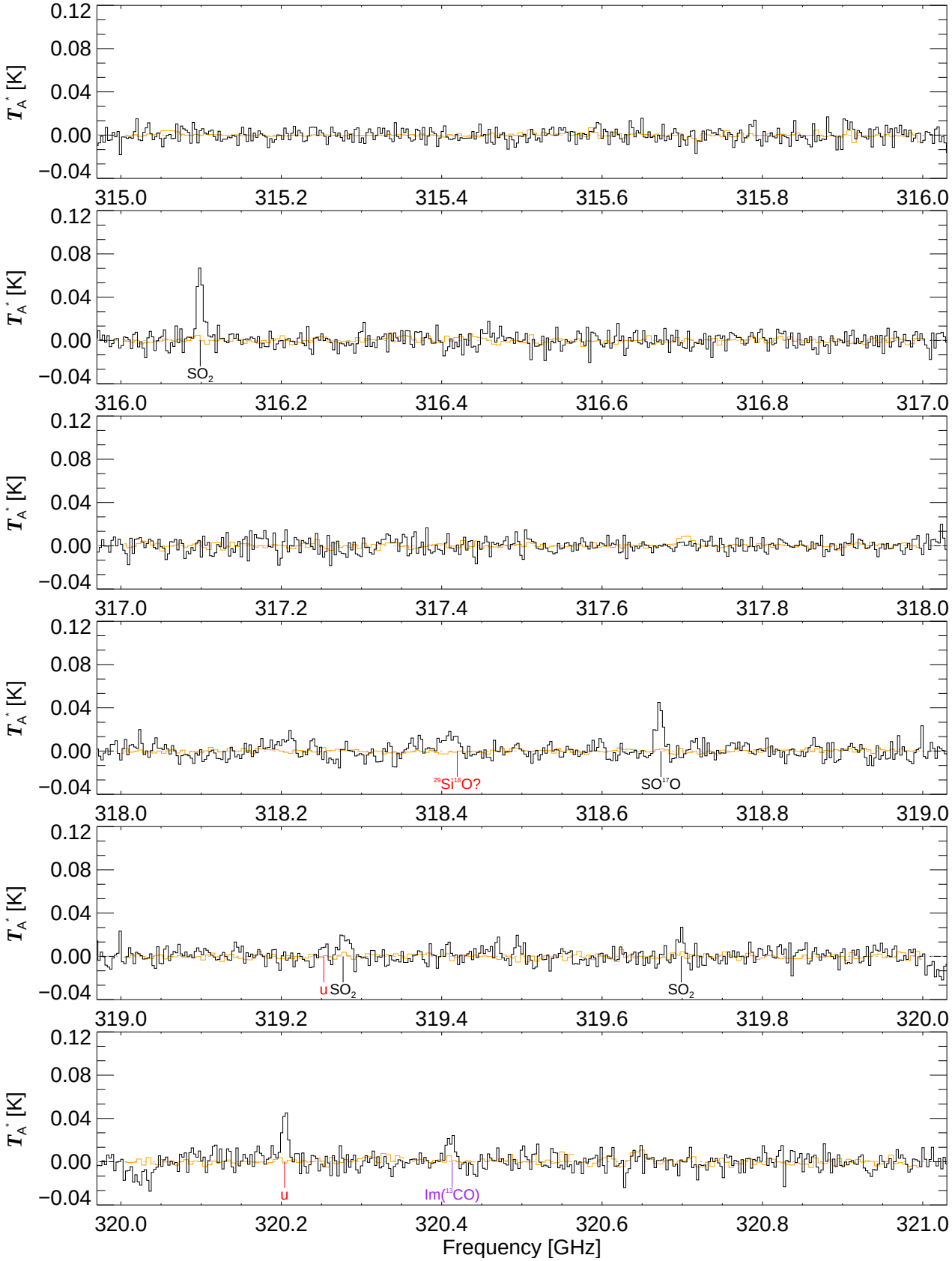

Fig. C.1. continued.

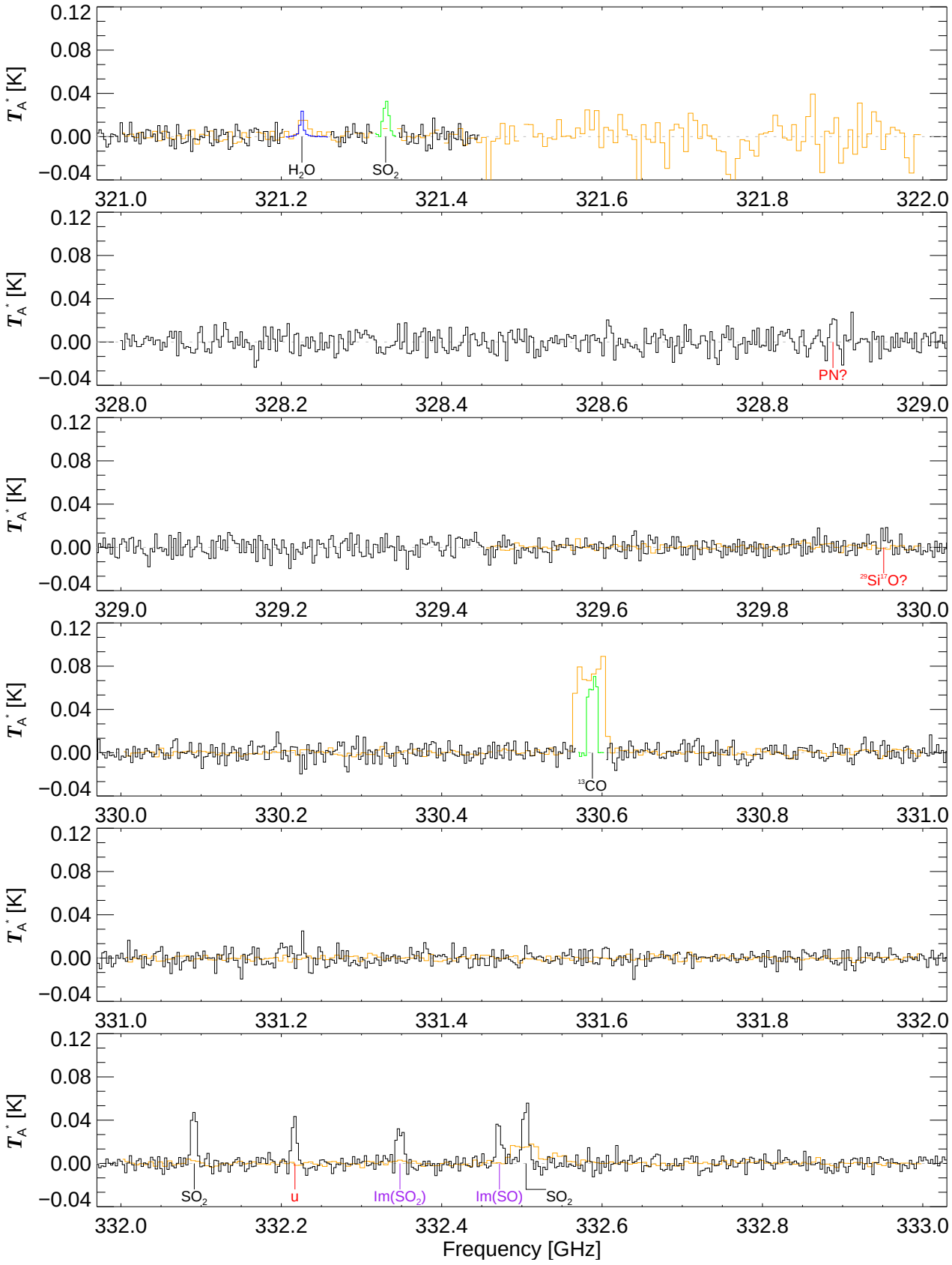

Fig. C.1. continued.

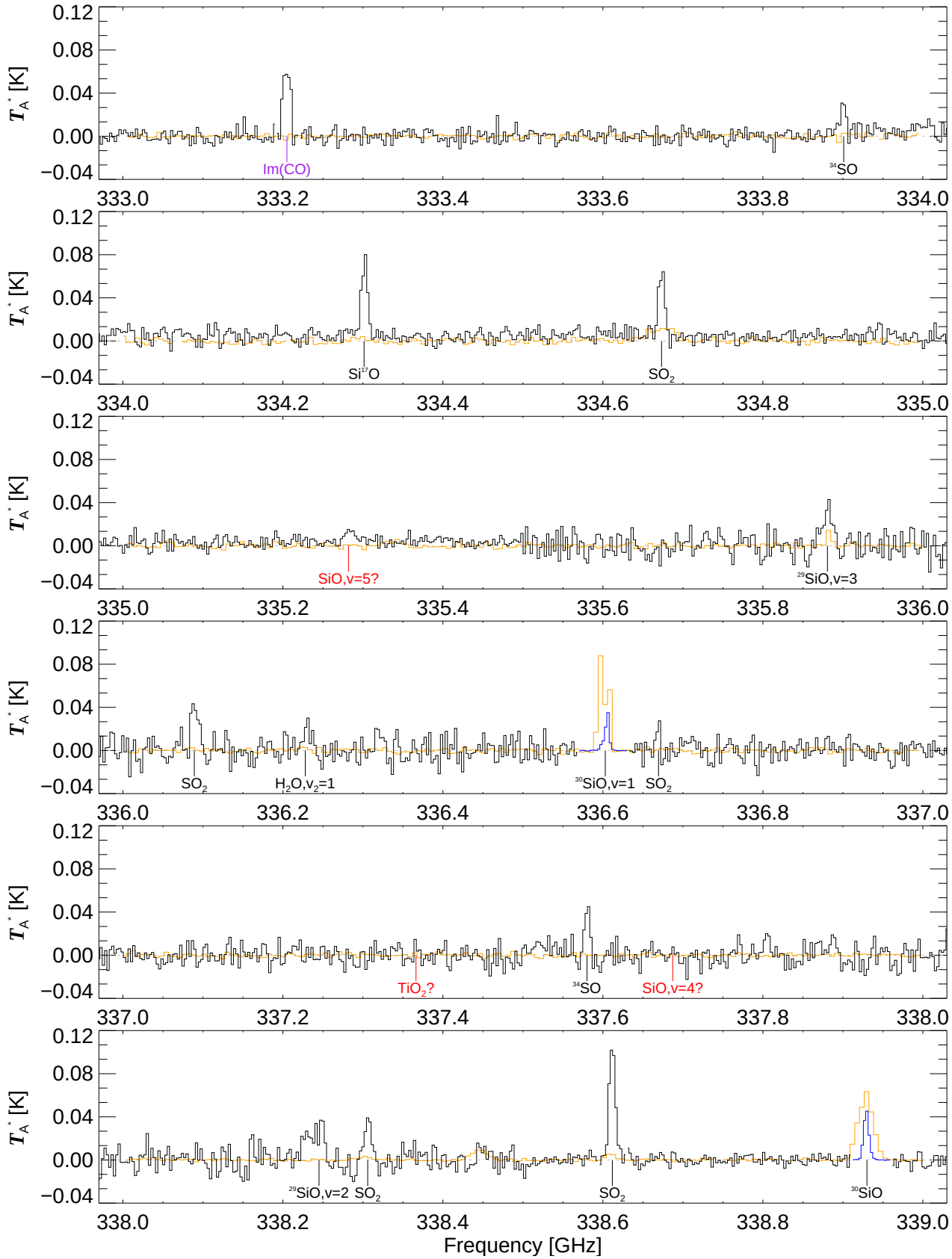

Fig. C.1. continued.

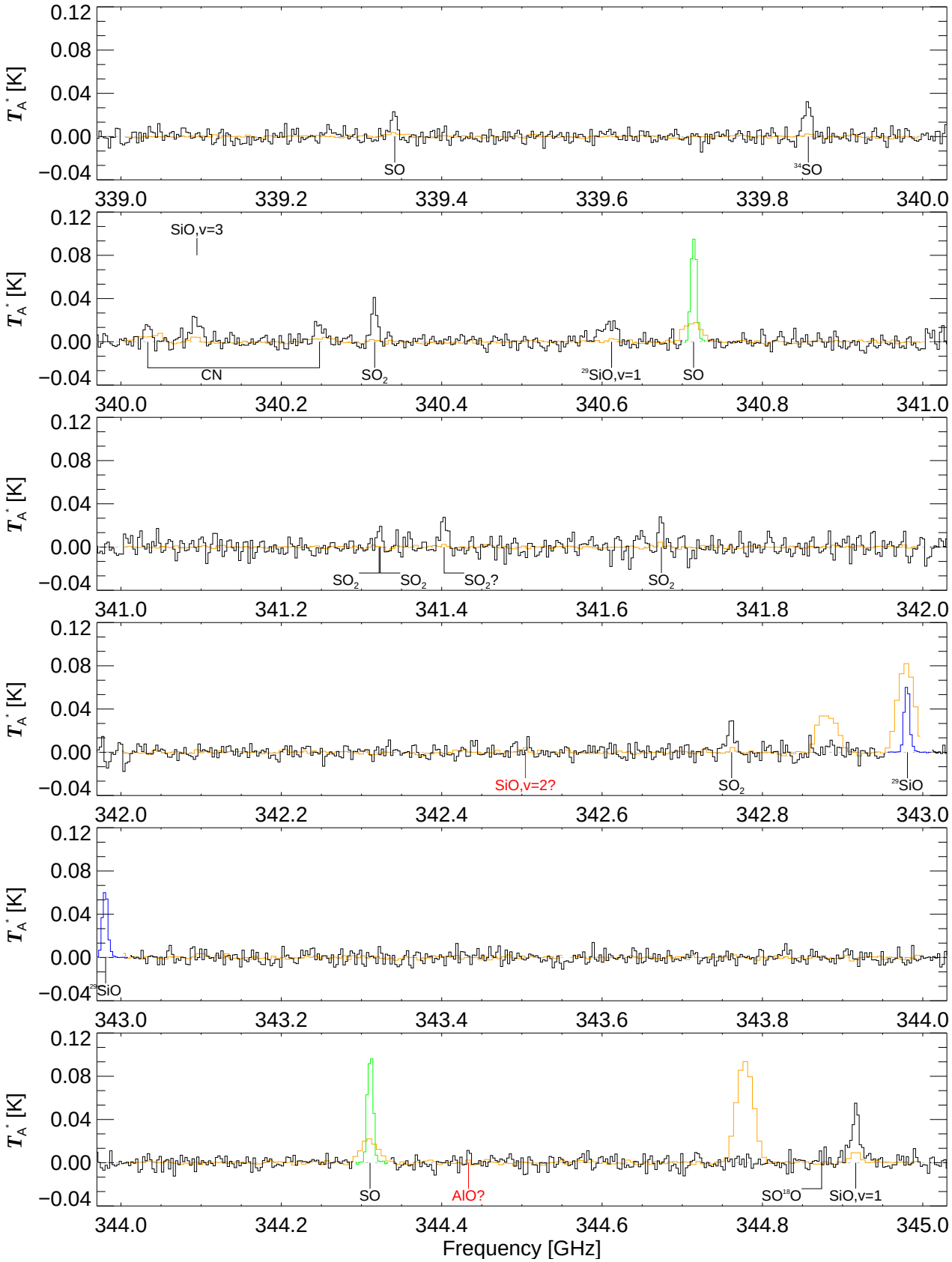

Fig. C.1. continued.

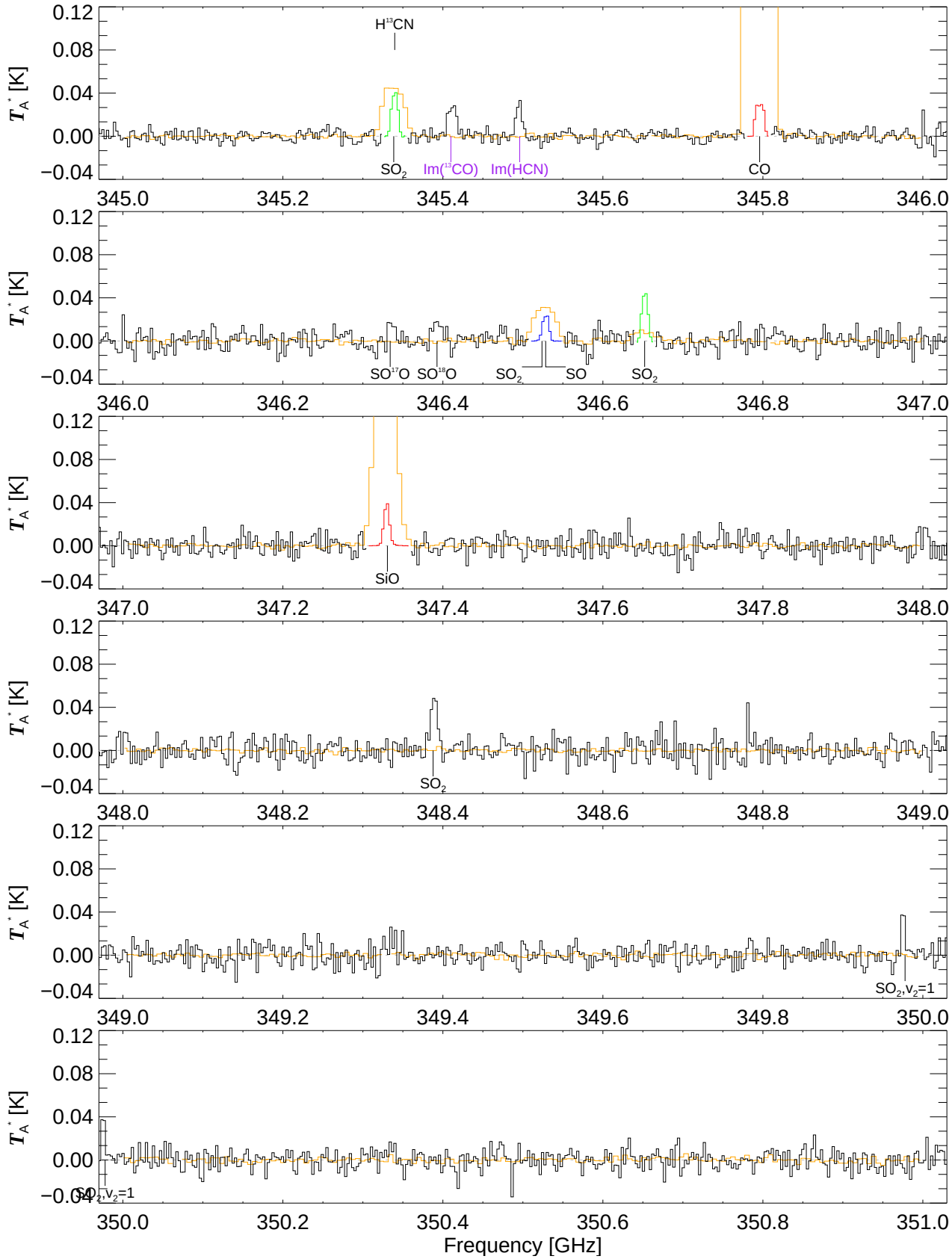

Fig. C.1. continued.

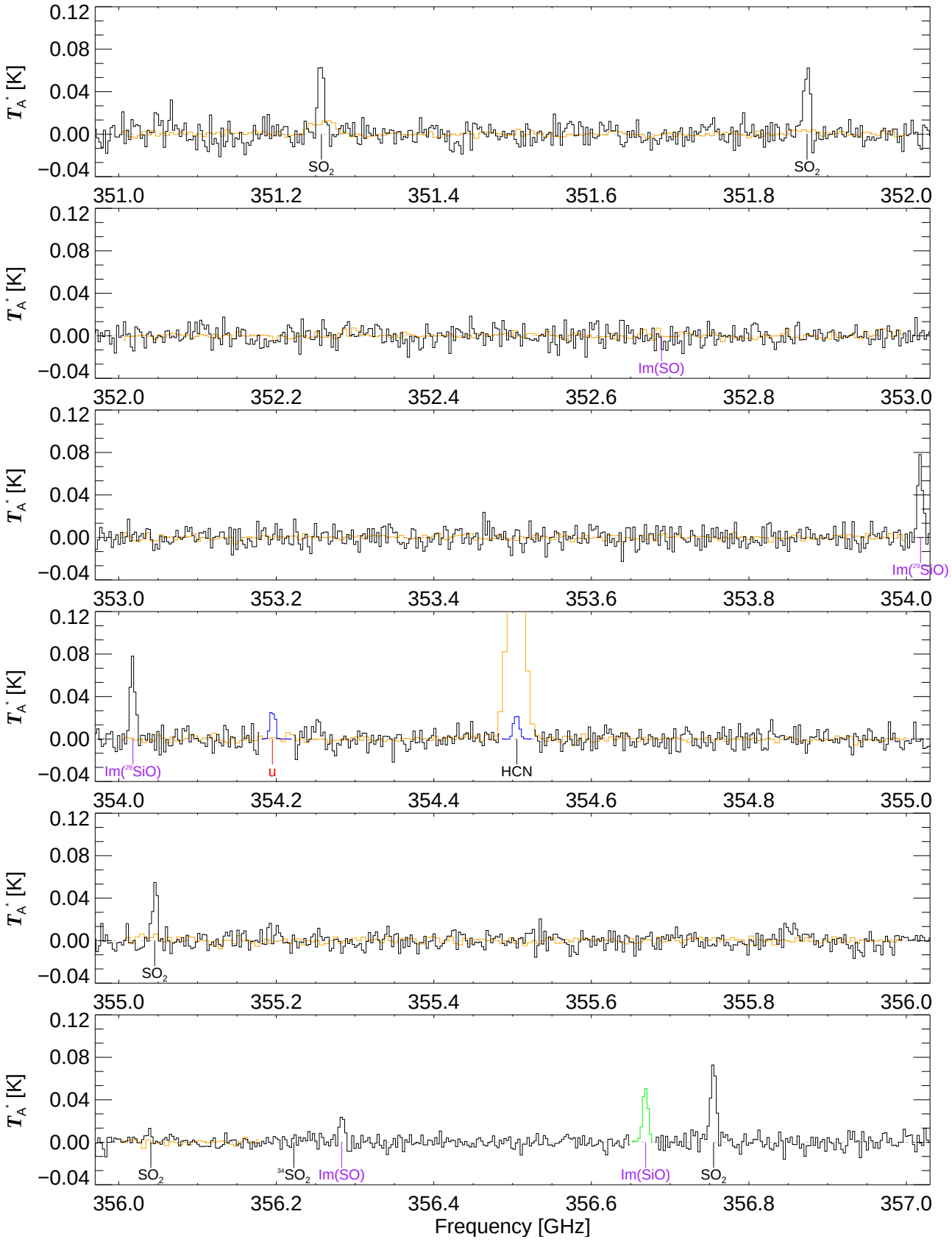

Fig. C.1. continued.

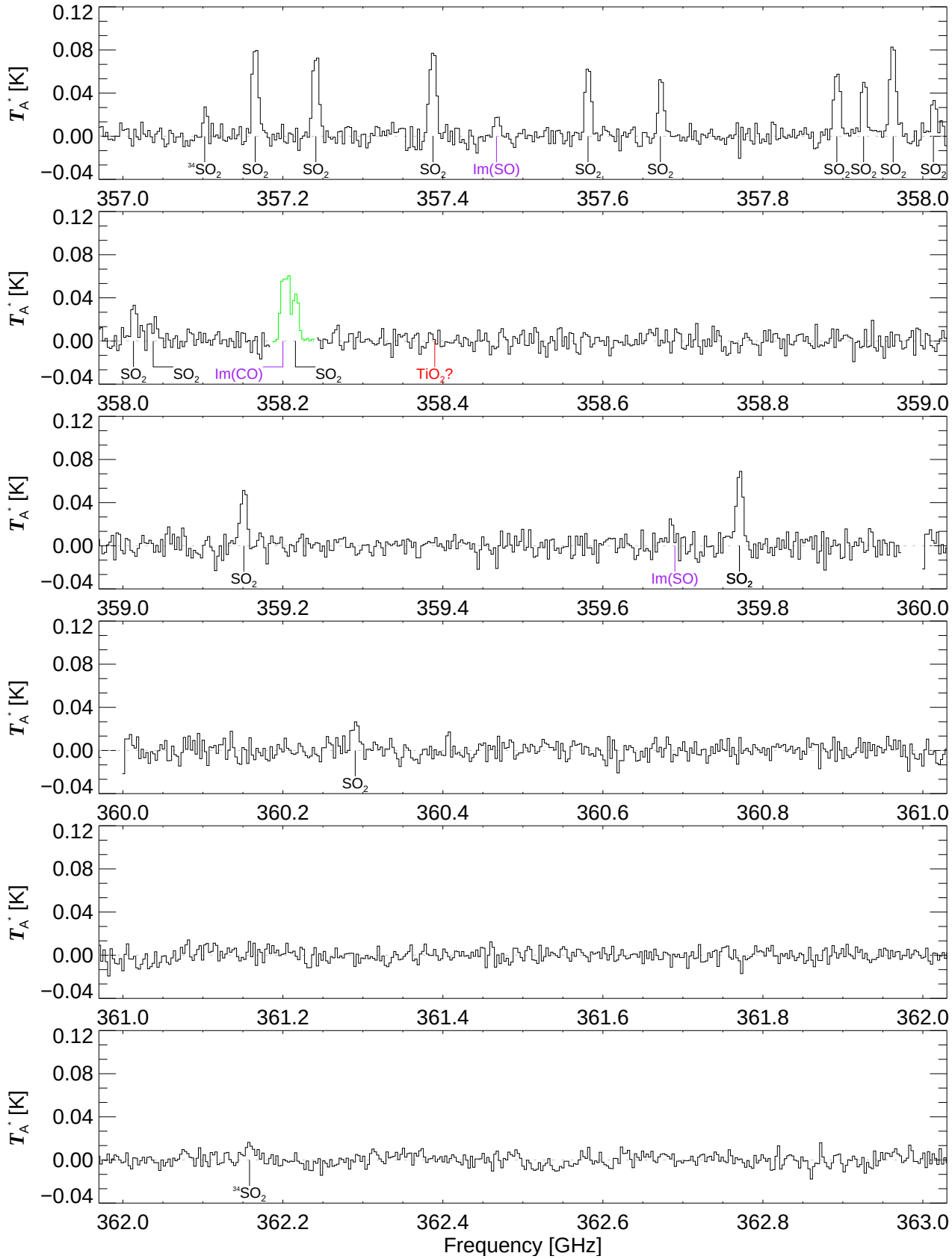

Fig. C.1. continued.

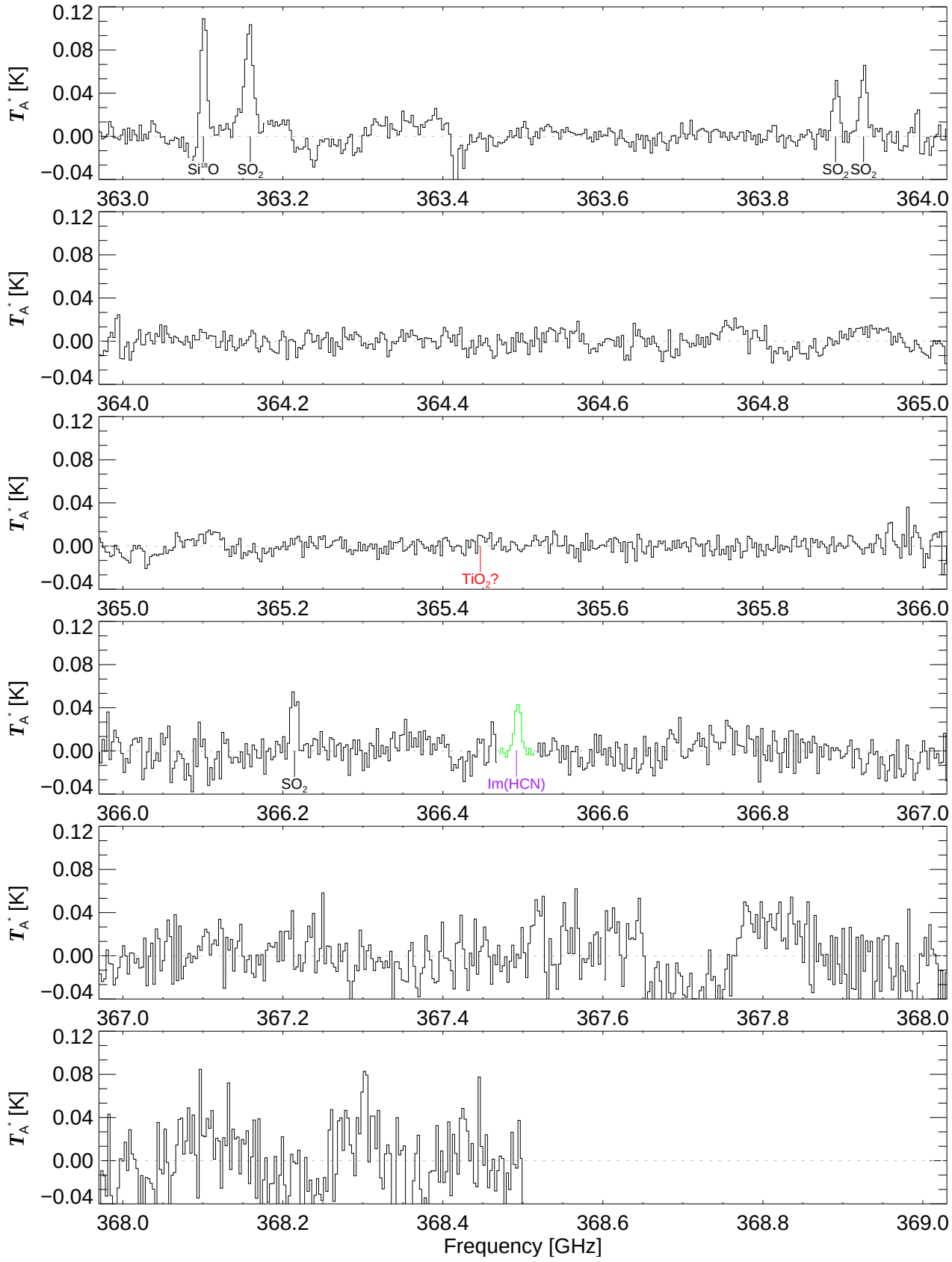

Fig. C.1. continued.

Table C.1. Overview of lines in the APEX survey of R Dor.

N_{line}	Molecule	Transition	ν_{lab} (MHz)	E_{up}/k (K)	Cat.	Δv	v_{min} (km s^{-1})	v_{max}	Peak (K)	I (K km s^{-1})	Remarks
1	SO_2	$18_{2,16}$–$18_{1,17}$	160 342.990	170.8	1	2.24	−6.9	5.8	0.02	0.19	
2	Im(SiO)	4–3	160 513.000	170.5	1	2.24	−24.8	15.5	0.04	0.31	Intensity at 2% of signal intensity.
3	TiO_2?	$14_{9,5}$–$15_{8,8}$	160 600.033	165.3	1	2.24	−7.0	11.6	0.01	0.03	Tentative.
4	SO_2	$10_{0,10}$–$9_{1,9}$	160 827.880	49.7	1	2.24	−5.8	8.4	0.03	0.25	
5	$Si^{18}O$	4–3	161 404.881	19.4	1	2.23	−9.1	10.0	0.04	0.38	
6	Im(SiO, v = 1)	4–3	161 719.900			2.22	−20.9	16.5	0.01	0.12	Intensity at 2% of signal intensity.
7	$^{34}SO_2$	$10_{0,10}$–$9_{1,9}$	162 020.376	49.5	1	2.22	−13.6	13.6	0.01	0.07	
8	Im(SiO,v = 2)	4–3	162 926.500			2.21	−11.2	11.8	0.06	0.42	Intensity at 2% of signal intensity.
9	SO_2	$18_{2,16}$–$17_{3,15}$	163 119.379	170.8	1	2.21	−6.5	7.3	0.01	0.08	
10	SiS?	9–8	163 376.785	39.2	1	2.20	−8.1	18.9	0.01	0.05	Tentative.
11	SO_2	$14_{1,13}$–$14_{0,14}$	163 605.533	101.8	1	2.20	−16.4	6.5	0.02	0.18	
12	SO_2?	$9_{4,6}$–$10_{3,7}$	165 123.635	80.6	1	2.18	−6.8	8.1	0.01	0.02	Tentative.
13	SO_2	$5_{2,4}$–$5_{1,5}$	165 144.651	23.6	1	2.18	−14.1	3.9	0.01	0.05	
14	SO_2	$7_{1,7}$–$6_{0,6}$	165 225.451	27.1	1	2.18	−6.1	11.3	0.02	0.19	
15	^{30}SiO, v = 2	4–3	167 160.943	3498.9	1	2.15	−8.4	10.5	0.01	0.11	Possible blend with $Si^{17}O$.
16	$Si^{17}O$	4–3	167 171.984	20.1	1	2.15	−8.1	11.4	0.03	0.21	Possible blend with ^{30}SiO, v = 2.
17	$SO^{18}O$?	$9_{4,6}$–$10_{3,7}$	168 012.745	77.5	1	2.14	−4.4	12.0	0.01	0.05	Tentative.
18	^{30}SiO, v = 1	4–3	168 323.353	1768.0	1	2.14	−9.5	8.5	0.04	0.32	
19	^{30}SiO	4–3	169 486.872	20.3	1	2.12	−10.8	10.4	0.48	3.95	
20	SiO, v = 3	4–3	170 070.348	5276.5	1	2.12	−8.9	8.5	0.79	4.59	
21	^{29}SiO, v = 1	4–3	170 328.321	1778.5	1	2.11	−10.3	7.3	0.10	0.69	
22	SiO, v = 2	4–3	171 275.165	3541.0	1	2.10	−11.8	17.1	7.75	49.30	
23	^{29}SiO	4–3	171 512.796	20.6	1	2.10	−12.8	8.7	0.92	7.33	
24	Im(H_2O)	$3_{1,2}$–$2_{2,0}$	171 690.000			2.10	−11.3	8.0	0.01	0.09	Intensity at 0.3% of signal intensity.
25	SO	4_4–3_3	172 181.403	33.8	1	2.09	−6.1	4.4	0.11	0.79	
26	SiO, v = 1	4–3	172 481.117	1789.8	1	2.09	−23.8	13.8	0.26	2.66	
27	$H^{13}CN$	2–1	172 677.851	12.4	1	2.08	−8.8	10.5	0.03	0.29	
28	u	?	173 514.000			2.07	−6.6	6.7	0.06	0.42	
29	SiO	4–3	173 688.238	20.8	1	2.07	−10.8	13.7	2.25	16.93	
30	$^{34}SO_2$	$18_{2,16}$–$17_{3,15}$	174 850.249	170.3	1	2.06	−5.4	9.9	0.01	0.06	
31	SO_2	$7_{2,6}$–$7_{1,7}$	175 275.721	35.5	1	2.05	−9.2	8.9	0.03	0.19	
32	^{34}SO	4_5–3_4	175 352.766	24.0	1	2.05	−21.4	13.4	0.02	0.14	
33	HCN, v_2 = 1?	2_{-1}–1_1	177 238.656	1037.1	1	2.03	−15.1	6.4	0.01	0.07	Tentative.
34	HCN	2–1	177 261.111	12.8	1	2.03	−13.2	13.4	0.27	2.52	
35	Im(^{30}SiO)	4–3	178 518.000			2.02	−4.4	18.6	0.03	0.21	Intensity at 5% of signal intensity.
36	SO	4_5–3_4	178 605.403	24.4	1	2.01	−8.7	9.9	0.22	1.79	
37	H_2O	$3_{1,2}$–$2_{2,0}$	183 310.087	204.7	2	1.96	−8.4	6.2	8.56	56.78	Maser.
38	Im(^{29}SiO)	4–3	183 488.000			2.45	−9.6	12.9	0.25	1.99	Intensity at 20% of signal intensity.
39	Im(SiO,v = 2)	4–3	183 727.000			1.96	−7.5	10.0	0.69	3.08	Intensity at 7% of signal intensity.

Notes. The columns list the line number N_{line}, the molecule, the transition, the theoretical rest frequency, the energy of the upper level of the transition, a reference to the catalogue used for the identification, the velocity resolution at which the identification was made, the minimum and maximum velocities of the line, v_{min} and v_{max} (w.r.t. the line center), the peak flux value, the integrated flux value over thelisted v-range, and remarks.Catalogues are (1) CDMS and (2) JPL.

Table C.1. continued.

$N_{\rm line}$	Molecule	Transition	$\nu_{\rm lab}$ (MHz)	$E_{\rm up}/k$ (K)	Cat.	Δv	$v_{\rm min}$ (km s^{-1})	$v_{\rm max}$	Peak (K)	I (K km s^{-1})	Remarks
40	TiO_2?	$26_{4,22}$–$26_{3,23}$	184 254.593	281.5	1	5.86	−1.3	18.9	0.08	0.38	Tentative.
41	TiO_2?	$30_{5,25}$–$30_{4,26}$	185 887.601	375.8	1	5.81	−7.3	10.2	0.02	0.23	Tentative.
42	PN?	4–3	187 953.263	22.6	1	3.83	−31.5	11.7	0.02	0.31	Tentative. Detection claimed from stacked spectrum.
43	SO_2	$9_{2,8}$–$9_{1,9}$	188 654.973	51.0	1	2.38	−8.5	8.4	0.03	0.22	
44	u	?	189 362.000			1.90	−12.5	10.3	0.02	0.16	
45	SO_2	$2_{2,0}$–$1_{1,1}$	192 651.020	12.6	1	1.87	−6.2	8.0	0.02	0.11	
46	SO_2	$9_{1,9}$–$8_{0,8}$	193 609.490	42.0	1	1.86	−5.3	7.6	0.06	0.42	
47	SO_2	$22_{3,19}$–$22_{2,20}$	195 320.700	257.8	1	1.84	−5.7	5.5	0.02	0.16	
48	PO	$5_{1,5,5}$–$4_{1,4,4}$	196 305.920	25.1	1	1.83	−5.6	9.5	0.01	0.06	
49	PO	$5_{1,5,4}$–$4_{1,4,3}$	196 319.816	25.2	1	1.83	−6.4	8.7	0.02	0.15	
50	PO	$5_{1,5,5}$–$4_{1,4,4}$	196 500.222	25.2	1	1.83	−4.1	12.4	0.02	0.08	
51	PO	$5_{1,5,4}$–$4_{1,4,3}$	196 518.400	25.2	1	1.83	−11.4	6.1	0.01	0.05	
52	SO_2	$20_{3,17}$–$20_{2,18}$	197 142.180	217.2	1	1.82	−9.3	5.9	0.03	0.23	
53	$^{29}Si^{18}O$?	5–4	199 031.722	28.7	1	3.62	−11.3	3.3	0.01	0.02	Tentative.
54	SO_2	$24_{3,21}$–$24_{2,22}$	200 287.421	302.4	1	1.80	−7.8	9.0	0.02	0.14	
55	SO_2	$16_{1,15}$–$16_{0,16}$	200 809.180	130.7	1	1.79	−14.5	11.8	0.03	0.27	
56	$Si^{18}O$	5–4	201 751.489	29.0	1	1.78	−5.7	5.3	0.07	0.51	
57	^{34}SO	5_4–4_3	201 846.480	38.1	1	2.23	−9.2	14.1	0.01	0.07	
58	SO_2	$12_{0,12}$–$11_{1,11}$	203 391.550	70.1	1	1.77	−15.8	10.5	0.07	0.59	
59	u	?	204 008.000			2.20	−8.8	5.6	0.01	0.09	
60	SO_2	$18_{3,15}$–$18_{2,16}$	204 246.761	180.6	1	1.76	−12.2	7.7	0.04	0.31	
61	SO_2	$11_{2,10}$–$11_{1,11}$	205 300.570	70.2	1	1.75	−6.3	6.4	0.04	0.25	
62	TiO_2?	$19_{5,15}$–$19_{4,16}$	206 049.296	166.5	1	1.75	−10.5	9.2	0.01	0.09	Tentative.
63	SO	5_4–4_3	206 176.005	38.6	1	1.74	−6.0	6.6	0.17	1.33	
64	SO_2	$3_{2,2}$–$2_{1,1}$	208 700.336	15.3	1	1.72	−9.4	5.4	0.01	0.09	
65	$Si^{17}O$	5–4	208 960.000	30.1	1	1.72	−11.6	7.9	0.04	0.35	
66	SiO, $v = 4$?	5–4	211 077.906	7004.5	1	3.41	−6.1	11.1	0.02	0.11	Tentative.
67	^{30}SiO	5–4	211 853.471	30.5	1	0.99	−19.7	15.2	0.70	5.34	
68	SiO, $v = 3$	5–4	212 582.550	5286.7	1	3.38	−10.1	22.8	0.04	0.43	
69	SO_2	$26_{3,23}$–$26_{2,24}$	213 068.427	350.8	1	2.11	−25.7	10.6	0.02	0.14	
70	SiO, $v = 2$?	5–4	214 088.575	3552.0	1	3.36	−12.8	21.2	0.01	0.15	Tentative.
71	^{29}SiO	5–4	214 385.752	30.9	1	2.10	−12.7	11.7	1.02	7.60	
72	SO_2	$16_{3,13}$–$16_{2,14}$	214 689.394	147.8	1	2.09	−9.5	19.0	0.04	0.33	
73	SO_2?	$17_{6,12}$–$18_{5,13}$	214 728.285	229.0	1	2.09	−15.5	15.5	0.01	0.02	Tentative.
74	SO	5_5–4_4	215 220.653	44.1	1	2.09	−12.0	13.0	0.21	1.67	
75	SiO, $v = 1$	5–4	215 596.018	1800.2	1	2.09	−13.2	25.9	1.10	8.53	
76	^{34}SO	5_6–4_5	215 839.920	34.4	1	2.08	−10.0	14.6	0.03	0.26	
77	SO_2	$22_{2,20}$–$22_{1,21}$	216 643.304	248.4	1	2.08	−6.4	19.5	0.05	0.40	
78	SiO	5–4	217 104.919	31.3	1	2.07	−26.3	29.3	3.04	24.54	
79	SO	5_6–4_5	219 949.442	35.0	1	2.04	−29.9	8.5	0.36	3.07	
80	^{13}CO	2–1	220 398.684	15.9	1	2.04	−24.0	18.6	0.16	1.41	

Table C.1. continued.

N_{line}	Molecule	Transition	ν_{lab} (MHz)	E_{up}/k (K)	Cat.	Δv	v_{min} (km s^{-1})	v_{max}	Peak (K)	I (K km s^{-1})	Remarks
81	SO_2	$11_{1,11}$–$10_{0,10}$	221 965.220	60.4	1	2.03	−23.3	8.3	0.09	0.72	
82	SO_2	$20_{2,18}$–$19_{3,17}$	224 264.814	207.8	1	2.01	−20.7	15.7	0.02	0.14	
83	SO_2	$13_{2,12}$–$13_{1,13}$	225 153.704	93.0	1	2.00	−23.8	14.7	0.06	0.49	
84	u	?	225 998.000			3.18	−8.0	13.9	0.01	0.12	
85	SO_2	$14_{3,11}$–$14_{2,12}$	226 300.027	119.0	1	1.99	−17.7	11.7	0.06	0.46	
86	CO	2–1	230 538.000	16.6	1	1.95	−38.4	9.4	2.90	30.98	
87	H_2O, $v_2 = 1$	$5_{5,0}$–$6_{4,3}$	232 686.700	3461.9	2	1.93	−16.2	13.9	0.04	0.25	
88	SO_2	$28_{3,25}$–$28_{2,26}$	234 187.057	403.0	1	3.07	−27.7	4.6	0.03	0.35	
89	PN?	5–4	234 935.695	33.8	1	3.06	−30.2	24.5	0.02	0.12	Tentative. Detection claimed from stacked spectrum.
90	SO_2	$4_{2,2}$–$3_{1,3}$	235 151.720	19.0	1	1.91	−10.7	11.5	0.04	0.18	
91	SO_2	$16_{1,15}$–$15_{2,14}$	236 216.687	130.7	1	1.90	−16.0	13.7	0.07	0.45	
92	SO_2	$12_{3,9}$–$12_{2,10}$	237 068.833	94.0	1	1.90	−25.5	12.6	0.06	0.46	
93	TiO_2?	$30_{7,23}$–$30_{6,24}$	238 050.296	395.3	1	4.53	−7.6	11.3	0.01	0.08	Tentative.
94	PO	$6_{-1,6,6}$–$5_{1,5,5}$	239 948.982	36.7	1	1.87	−25.4	15.1	0.03	0.23	
95	PO	$6_{-1,6,5}$–$5_{1,5,4}$	239 958.101	36.7	1	1.87	−14.0	26.5	0.03	0.23	
96	PO	$6_{1,6,6}$–$5_{-1,5,5}$	240 141.059	36.7	1	1.87	−32.9	16.9	0.03	0.36	
97	PO	$6_{1,6,5}$–$5_{-1,5,4}$	240 152.528	36.7	1	1.87	−18.6	31.2	0.03	0.36	
98	SO_2	$18_{1,17}$–$18_{0,18}$	240 942.792	163.1	1	1.87	−20.7	21.1	0.05	0.40	
99	SO_2	$5_{2,4}$–$4_{1,3}$	241 615.797	23.6	1	1.86	−19.1	15.3	0.04	0.33	
100	$Si^{18}O$	6–5	242 094.982	40.7	1	1.86	−20.5	9.3	0.10	0.83	
101	NaCl, $v = 2$?	19–18	243 574.069	1151.2	1	2.95	−33.6	30.6	0.01	0.12	Tentative. Variability seen between two observing dates.
102	SO_2	$14_{0,14}$–$13_{1,13}$	244 254.218	93.9	1	1.84	−13.8	17.8	0.13	1.13	
103	TiO_2?	$23_{6,18}$–$23_{5,19}$	244 476.538	241.6	1	4.41	−14.7	9.2	0.01	0.10	Tentative.
104	$^{34}SO_2$	$14_{0,14}$–$13_{1,13}$	244 481.517	93.5	1	1.84	−9.4	14.6	0.01	0.09	
105	SO_2	$26_{3,23}$–$25_{4,22}$	245 339.233	350.8	1	1.83	−11.3	13.6	0.02	0.11	
106	SO_2	$10_{3,7}$–$10_{2,8}$	245 563.422	72.7	1	1.83	−15.4	14.7	0.05	0.45	
107	Im(SiO)	6–5	246 486.000			1.82	−17.6	16.7	0.07	0.47	Intensity at 2% of signal intensity.
108	^{34}SO	6_5–5_4	246 663.470	49.9	1	1.82	−22.3	14.3	0.02	0.18	
109	SO_2	$31_{9,23}$–$32_{8,24}$	247 169.768	654.5	1	1.82	−20.2	32.0	0.01	0.19	
110	NaCl?	19–18	247 239.733	118.7	1	2.91	−17.2	26.5	0.01	0.17	Tentative.
111	SO_2	$15_{2,14}$–$15_{1,15}$	248 057.402	119.3	1	1.81	−15.1	9.6	0.05	0.37	
112	$Si^{17}O$	6–5	250 744.695	42.1	1	1.79	−19.0	24.7	0.06	0.49	
113	SO_2	$13_{1,13}$–$12_{0,12}$	251 199.675	82.2	1	1.79	−7.0	18.2	0.10	0.81	
114	SO_2	$8_{3,5}$–$8_{2,6}$	251 210.585	55.2	1	1.79	−7.5	6.1	0.04	0.26	
115	SiO, $v = 5$	6–5	251 481.622	8717.3	1	1.43	−7.2	11.5	0.02	0.10	
116	Im(SO_2)	$11_{3,9}$–$11_{2,10}$	251 744.000			1.43	−9.2	6.8	0.02	0.05	Intensity at 23% of signal intensity.
117	SO	6_5–5_4	251 825.770	50.7	1	1.79	−17.7	10.9	0.27	2.21	
118	^{30}SiO, $v = 1$	6–5	252 471.372	1790.2	1	1.42	−14.0	5.8	0.03	0.11	
119	^{34}SO	6_6–5_5	253 207.017	55.7	1	1.78	−14.9	8.5	0.03	0.23	
120	^{29}SiO, $v = 2$	6–5	253 703.479	3541.9	1	1.77	−17.0	12.7	0.03	0.18	

Table C.1. continued.

$N_{\rm line}$	Molecule	Transition	$\nu_{\rm lab}$ (MHz)	$E_{\rm up}/k$ (K)	Cat.	Δv	$v_{\rm min}$ (km s^{-1})	$v_{\rm max}$	Peak (K)	I (K km s^{-1})	Remarks
121	^{30}SiO	6–5	254 216.656	42.7	1	1.77	−17.2	12.7	0.95	6.98	
122	SO_2	$6_{3,3}$–$6_{2,4}$	254 280.536	41.4	1	1.77	−21.8	12.9	0.07	0.60	
123	^{29}SiO, $v = 1$	6–5	255 478.495	1801.0	1	1.76	−24.2	16.0	0.05	0.18	
124	SO_2	$4_{3,1}$–$4_{2,2}$	255 553.302	31.3	1	1.76	−11.0	10.8	0.02	0.03	
125	SO_2	$5_{3,3}$–$5_{2,4}$	256 246.945	35.9	1	1.75	−19.1	11.8	0.03	0.31	
126	^{34}SO	6_7–5_6	256 877.809	46.7	1	1.75	−12.2	11.6	0.04	0.28	
127	SiO, $v = 2$	6–5	256 898.396	3564.3	1	1.75	−20.9	11.8	0.19	1.36	
128	SO_2	$7_{3,5}$–$7_{2,6}$	257 099.966	47.8	1	1.75	−16.4	9.5	0.04	0.34	
129	^{29}SiO	6–5	257 255.213	43.2	1	1.75	−28.2	20.6	1.21	9.31	
130	SO	6_6–5_5	258 255.826	56.5	1	1.74	−25.9	14.5	0.33	2.57	
131	SO_2	$32_{4,28}$–$32_{3,29}$	258 388.716	531.1	1	1.74	−17.8	12.8	0.03	0.25	
132	SiO, $v = 1$	6–5	258 707.324	1812.6	1	1.74	−21.5	21.6	0.05	0.78	
133	SO_2	$9_{3,7}$–$9_{2,8}$	258 942.199	63.5	1	1.74	−13.1	9.8	0.04	0.39	
134	H^{13}CN	3–2	259 011.798	24.9	1	1.74	−24.9	7.8	0.07	0.57	
135	SO_2	$30_{4,26}$–$30_{3,27}$	259 599.448	471.5	1	1.73	−9.3	6.5	0.02	0.16	
136	SiO	6–5	260 518.009	43.8	1	1.73	−13.8	14.3	4.26	31.72	
137	TiO_2?	$34_{5,29}$–$34_{4,30}$	261 127.076	474.3	1	4.13	−13.9	9.0	0.01	0.07	Tentative.
138	SO	6_7–5_6	261 843.721	47.6	1	1.72	−10.7	11.2	0.50	3.87	
139	Data	?	262 000.000			2.75	−22.9	22.9	0.01	0.04	Data issue.
140	SO_2	$11_{3,9}$–$11_{2,10}$	262 256.906	82.8	1	1.71	−9.9	20.4	0.07	0.54	
141	H_2O, $v_2 = 1$	$7_{7,0}$–$8_{6,3}$	263 451.357	4474.5	2	1.71	−18.4	23.4	0.02	0.26	
142	SO_2	$30_{3,27}$–$30_{2,28}$	263 543.953	459.0	1	1.71	−9.6	12.0	0.03	0.17	
143	Im(^{29}SiO)	6–5	263 780.000			1.70	−20.1	15.5	0.07	0.47	Intensity at 4% of signal intensity.
144	HCN	3–2	265 886.400	25.5	1	1.69	−20.9	9.7	0.71	5.82	
145	SO_2	$13_{3,11}$–$13_{2,12}$	267 537.451	105.8	1	1.68	−13.2	15.1	0.05	0.43	
146	SO_2	$28_{4,24}$–$28_{3,25}$	267 719.840	415.9	1	1.68	−15.3	17.0	0.06	0.35	
147	Im(^{29}SiO)	6–5	267 745.000			1.68	−10.1	10.0	0.04	0.33	Intensity at 5% of signal intensity.
148	u	?	267 993.000			1.68	−4.0	6.0	0.02	0.09	
149	H_2O, $v_2 = 2$	$6_{5,2}$–$7_{4,3}$	268 149.117	6039.0	2	1.68	−12.5	21.7	0.04	0.33	
150	Im(SO_2)	$16_{0,16}$–$15_{1,15}$	270 537.000			1.66	−18.5	26.2	0.03	0.34	Intensity at 15% of signal intensity.
151	TiO_2?	$26_{7,19}$–$26_{6,20}$	271 311.202	310.7	1	3.98	−10.5	13.4	0.01	0.11	Tentative.
152	SO_2	$7_{2,6}$–$6_{1,5}$	271 529.014	35.5	1	1.32	−13.9	19.2	0.05	0.40	
153	TiO_2?	$22_{1,21}$–$22_{0,22}$	271 566.716	180.5	1	3.97	−3.5	12.8	0.01	0.06	Tentative.
154	SiS?	15–14	272 243.052	104.5	1	2.64	−16.4	26.7	0.02	0.16	Tentative.
155	Im(SO_2)	$17_{3,15}$–$17_{2,16}$	273 258.000			1.32	−14.3	12.1	0.04	0.27	Intensity at 54% of signal intensity.
156	u	?	273 284.000			1.32	−18.6	12.1	0.07	0.51	
157	SO_2	$17_{2,16}$–$17_{1,17}$	273 752.822	149.2	1	1.31	−9.1	9.7	0.04	0.28	
158	SO_2	$15_{3,13}$–$15_{2,14}$	275 240.184	132.5	1	1.31	−13.5	15.4	0.06	0.53	
159	TiO_2?	$27_{4,24}$–$27_{3,25}$	276 437.905	292.7	1	3.90	−16.5	8.0	0.00	−0.01	Tentative.
160	TiO_2?	$27_{16,12}$–$28_{15,13}$	276 827.330	555.0	1	3.90	−10.5	13.2	0.01	0.06	Tentative.
161	^{29}Si^{18}O	7–6	278 627.547	53.3	1	2.58	−7.7	5.4	0.01	0.07	
162	u	?	280 051.000			1.50	−5.5	6.3	0.02	0.08	

Table C.1. continued.

N_{line}	Molecule	Transition	ν_{lab} (MHz)	E_{up}/k (K)	Cat.	Δv	v_{min} (km s^{-1})	v_{max}	Peak (K)	I (K km s^{-1})	Remarks
163	SO_2	$26_{4,22}$–$26_{3,23}$	280 807.246	364.3	1	1.28	−22.3	19.9	0.04	0.40	
164	SO_2	$36_{4,32}$–$36_{3,33}$	281 688.931	662.1	1	1.28	−12.0	14.4	0.03	0.17	
165	SO_2	$15_{1,15}$–$14_{0,14}$	281 762.600	107.4	1	1.28	−23.1	15.2	0.16	1.32	
166	PN?	6–5	281 914.205	47.4	1	2.55	−6.1	5.6	0.02	0.09	Tentative. Detection claimed from stacked spectrum.
167	SO_2	$6_{2,4}$–$5_{1,5}$	282 036.566	29.2	1	1.28	−9.8	18.5	0.03	0.16	
168	SO_2	$20_{1,19}$–$20_{0,20}$	282 292.806	198.9	1	1.27	−12.8	22.7	0.04	0.28	
169	$Si^{18}O$	7–6	282 434.716	54.2	1	1.27	−9.7	19.4	0.12	0.95	
170	Im(^{30}SiO)	7–6	283 425.000			1.48	−9.6	11.4	0.03	0.19	Intensity at 3% of signal intensity.
171	SO_2	$16_{0,16}$–$15_{1,15}$	283 464.769	121.0	1	1.27	−26.9	11.2	0.15	1.23	
172	u	?	283 535.000			1.27	−6.6	11.6	0.02	0.14	
173	PO	$7_{1,7,7}$–$6_{-1,6,6}$	283 586.835	50.3	1	2.54	−22.9	14.3	0.04	0.44	
174	PO	$7_{1,7,6}$–$6_{-1,6,5}$	283 593.186	50.3	1	2.54	−16.2	21.0	0.04	0.44	
175	PO	$7_{-1,7,7}$–$6_{1,6,6}$	283 777.610	50.3	1	2.54	−50.6	27.4	0.03	0.45	
176	PO	$7_{-1,7,6}$–$6_{1,6,5}$	283 785.419	50.3	1	2.54	−42.3	35.6	0.03	0.45	
177	$SO^{18}O$	$19_{7,13}$–$20_{6,14}$	285 106.318	282.4	1	2.42	−13.2	22.2	0.01	0.03	Weak.
178	$SO^{18}O$	$19_{7,12}$–$20_{6,15}$	285 109.824	282.4	1	2.42	−9.5	25.9	0.01	0.03	Weak.
179	SO_2	$17_{3,15}$–$17_{2,16}$	285 743.600	162.9	1	1.26	−31.1	12.2	0.06	0.41	
180	Im(SO)	7_7–6_6	286 714.000			1.25	−32.3	9.0	0.16	1.08	Intensity at 21% of signal intensity.
181	TiO_2?	$34_{8,26}$–$34_{7,27}$	286 802.035	506.8	1	3.76	−4.9	14.5	0.02	0.15	Tentative.
182	Im(^{29}SiO)	7–6	287 880.000			1.25	−30.8	15.6	0.25	2.09	Intensity at 12% of signal intensity.
183	$SO^{18}O$	$19_{3,17}$–$19_{2,18}$	288 269.800	186.8	1	1.25	−11.5	19.7	0.02	0.21	
184	$SO^{18}O$	$25_{4,21}$–$25_{3,22}$	288 296.707	322.1	1	1.25	−16.5	13.7	0.10	0.51	
185	$SO^{18}O$	$35_{10,26}$–$36_{9,27}$	288 481.517	786.3	1	1.25	−4.1	15.1	0.02	0.15	
186	SO_2	$18_{1,17}$–$17_{2,16}$	288 519.996	163.1	1	1.25	−13.8	20.9	0.09	0.54	
187	$^{29}Si^{17}O$?	7–6	288 718.636	55.4	1	1.25	−8.5	11.1	0.02	0.08	Tentative.
188	Im(SiO)	7–6	291 073.000			1.24	−17.9	28.8	0.10	0.76	Intensity at 3% of signal intensity.
189	TiO_2?	$20_{7,13}$–$20_{6,14}$	291 163.340	207.0	1	2.47	−7.3	5.9	0.01	0.05	Tentative.
190	$Si^{17}O$	7–6	292 525.407	56.2	1	1.23	−7.7	8.8	0.06	0.49	
191	Im(SiO, v = 1)	7–6	293 189.000			1.23	−12.3	15.7	0.08	0.64	Intensity at 12% of signal intensity.
192	H_2O, v_2 = 1	$6_{6,1}$–$7_{5,2}$	293 664.491	3933.6	2	1.23	−26.0	13.4	0.04	0.55	
193	^{29}SiO, v = 3	7–6	293 907.859	5280.1	1	1.22	−15.8	9.6	0.04	0.40	
194	TiO_2?	$33_{6,28}$–$33_{5,29}$	294 442.979	451.9	1	3.67	−15.5	14.4	0.02	0.13	Tentative.
195	^{34}SO	7_7–6_6	295 396.334	69.9	1	1.22	−13.5	16.2	0.03	0.06	
196	u	?	295 629.000			2.33	−8.2	7.1	0.03	0.20	
197	SO_2	$26_{2,24}$–$26_{1,25}$	296 168.675	340.6	1	1.21	−6.8	16.7	0.03	0.27	
198	SO_2	$24_{4,20}$–$24_{3,21}$	296 535.422	316.6	1	1.21	−6.3	19.1	0.04	0.23	Possible blend with SO.
199	SO	7_6–6_5	296 550.064	64.9	1	1.21	−12.3	8.5	0.38	2.85	Possible blend with SO_2.
200	^{30}SiO	7–6	296 575.730	56.9	1	1.21	−29.7	13.7	0.94	6.72	
201	u	?	297 404.000			1.51	−16.0	13.7	0.03	0.34	Tentative: TiN at 297 401.8 MHz.
202	H_2O, v_2 = 1	$6_{6,0}$–$7_{5,3}$	297 439.276	3933.6	2	1.21	−34.0	14.4	0.02	0.12	
203	SiO, v = 3	7–6	297 595.467	5313.3	1	1.21	−13.1	23.2	0.03	0.26	

Table C.1. continued.

$N_{\rm line}$	Molecule	Transition	$\nu_{\rm lab}$ (MHz)	$E_{\rm up}/k$ (K)	Cat.	Δv	$v_{\rm min}$ (km s^{-1})	$v_{\rm max}$	Peak (K)	I (K km s^{-1})	Remarks
204	TiO_2?	$32_{6,26}$–$31_{7,25}$	297 702.188	432.1	1	3.63	−12.3	13.3	0.02	0.19	Tentative.
205	^{29}SiO, $v = 1$	7–6	298 047.637	1815.3	1	1.21	−18.9	26.0	0.02	0.23	
206	^{34}SO	7_8–6_7	298 257.982	61.0	1	1.21	−31.7	23.5	0.04	0.46	
207	u	?	298 464.000			1.21	−13.2	11.6	0.03	0.12	
208	SO_2	$9_{2,8}$–$8_{1,7}$	298 576.307	51.0	1	1.20	−12.4	14.3	0.07	0.41	
209	Data	/	299 035.000			2.31	−13.4	14.4	0.02	0.22	Data issue.
210	NaCl?	23–22	299 145.700	172.4	1	2.41	−15.9	12.1	0.01	0.13	Tentative.
211	SO_2	$19_{3,17}$–$19_{2,18}$	299 316.818	197.0	1	1.20	−20.3	11.9	0.05	0.45	
212	SiO, $v = 2$	7–6	299 703.909	3578.7	1	1.20	−12.6	12.2	0.73	2.84	
213	^{29}SiO	7–6	300 120.480	57.6	1	1.20	−18.8	18.9	1.57	11.13	
214	SO_2	$32_{3,29}$–$32_{2,30}$	300 273.418	518.7	1	1.20	−8.4	19.1	0.03	0.31	
215	SO	7_7–6_6	301 286.124	71.0	1	1.19	−17.0	13.8	0.44	3.46	
216	SiO, $v = 1$	7–6	301 814.332	1827.1	1	1.19	−15.4	21.3	1.32	16.33	
217	SO_2	$19_{2,18}$–$19_{1,19}$	301 896.629	182.6	1	1.19	−8.6	16.1	0.06	0.42	
218	$SO^{18}O$	$17_{2,16}$–$16_{2,15}$	303 154.811	141.3	2	2.37	−11.0	13.6	0.02	0.19	
219	$SO^{18}O$	$18_{0,18}$–$17_{1,17}$	303 475.791	143.4	2	2.37	−15.9	18.0	0.02	0.18	
220	SiO	7–6	303 926.812	58.3	1	1.18	−21.9	14.5	4.01	29.39	
221	SO	7_8–6_7	304 077.844	62.1	1	1.18	−29.3	29.0	0.61	4.74	
222	Im(H_2O, $v_2 = 1$)	$6_{6,1}$–$7_{5,2}$	305 331.000			2.26	−3.2	10.5	0.02	0.10	Intensity at 50% of signal intensity.
223	SO_2	$38_{4,34}$–$38_{3,35}$	307 185.305	733.4	1	1.17	−9.7	7.7	0.02	0.16	
224	PNO?	25–24	309 423.503	193.1	1	2.33	−11.5	13.5	0.02	0.18	Tentative. No other transitions of PNO detected, but feature is real.
225	u	?	309 449.000			1.16	−5.6	11.6	0.01	0.06	
226	SO	2_2–1_2	309 502.444	19.3	1	1.16	−17.5	9.4	0.02	0.05	
227	SO_2	$22_{4,18}$–$22_{3,19}$	312 542.519	272.8	1	1.15	−23.8	13.3	0.05	0.32	
228	SO_2	$3_{3,1}$–$2_{2,0}$	313 279.718	27.6	1	1.15	−11.0	9.6	0.05	0.27	
229	SO_2	$28_{3,25}$–$27_{4,24}$	313 412.285	403.0	1	2.30	−14.6	10.0	0.02	0.03	
230	SO_2	$17_{1,17}$–$16_{0,16}$	313 660.852	136.1	1	1.15	−19.6	9.9	0.26	2.12	
231	SO_2	$21_{3,19}$–$21_{2,20}$	316 098.874	234.7	1	1.14	−18.0	17.8	0.07	0.66	
232	$^{29}Si^{18}O$?	8–7	318 419.436	68.8	1	1.41	−5.6	11.5	0.02	0.19	Tentative.
233	$SO^{17}O$	$28_{3,26}$–$29_{0,29}$	318 673.384	383.9	1	1.13	−13.2	16.7	0.05	0.39	
234	u	?	319 253.000			1.41	−9.4	13.1	0.02	0.08	
235	SO_2	$40_{5,35}$–$40_{4,36}$	319 277.053	823.7	1	2.25	−12.2	10.8	0.03	0.27	
236	SO_2	$42_{5,37}$–$42_{4,38}$	319 698.702	902.3	1	2.16	−6.7	12.9	0.03	0.25	
237	u	?	320 204.000			2.25	−21.3	18.8	0.06	0.52	
238	Im(^{13}CO)	3–2	320 413.000			2.25	−13.7	16.1	0.04	0.26	Intensity at 7% of signal intensity.
239	H_2O	$10_{2,9}$–$9_{3,6}$	321 225.677	1861.2	2	1.12	−21.9	15.8	0.64	3.35	Maser.
240	SO_2	$18_{0,18}$–$17_{1,17}$	321 330.166	151.5	1	1.12	−15.6	22.0	0.17	1.48	
241	PN?	7–6	328 888.006	63.1	1	1.09	−6.3	6.3	0.03	0.17	Tentative. Detection claimed from stacked spectrum.
242	$^{29}Si^{17}O$?	8–7	329.951.219	71.3	1	2.18	−11.3	3.9	0.02	0.12	Tentative.
243	^{13}CO	3–2	330 587.965	31.7	1	1.09	−7.5	7.1	0.42	3.91	

Table C.1. continued.

N_{line}	Molecule	Transition	ν_{lab} (MHz)	E_{up}/k (K)	Cat.	Δv	v_{min} (km s^{-1})	v_{max}	Peak (K)	I (K km s^{-1})	Remarks
244	SO_2	$21_{2,20}$–$21_{1,21}$	332 091.431	219.5	1	1.35	−4.6	3.7	0.05	0.32	
245	u	?	332 217.000			1.35	−16.9	8.6	0.05	0.21	
246	Im(SO_2)	$19_{1,19}$–$18_{0,18}$	332 348.000			1.35	−9.3	5.3	0.04	0.29	Intensity at 18% of signal intensity.
247	Im(SO)	8_9–7_8	332 472.000			1.35	−11.7	14.2	0.05	0.27	Intensity at 17% of signal intensity.
248	SO_2	$4_{3,1}$–$3_{2,2}$	332 505.242	31.3	1	1.35	−7.1	6.6	0.06	0.43	
249	Im(CO)	3–2	333 205.000			1.35	−11.2	8.7	0.07	0.63	Intensity at 5% of signal intensity.
250	^{34}SO	8_7–7_6	333 900.983	79.9	1	1.35	−17.9	18.7	0.04	0.38	
251	$Si^{17}O$	8–7	334 301.470	72.2	1	1.35	−5.2	10.1	0.09	0.65	
252	SO_2	$8_{2,6}$–$7_{1,7}$	334 673.353	43.1	1	1.34	−6.7	5.6	0.07	0.55	
253	SiO, $v = 5$?	8–7	335 281.980	8747.0	1	2.15	−20.1	10.3	0.02	0.28	Tentative.
254	^{29}SiO, $v = 3$	8–7	335 880.695	5296.2	1	1.34	−10.8	19.8	0.05	0.45	
255	SO_2	$23_{3,21}$–$23_{2,22}$	336 089.228	276.0	1	1.34	−14.9	7.7	0.06	0.47	
256	H_2O, $v_2 = 1$	$5_{2,3}$–$6_{1,6}$	336 227.941	2955.2	1	1.07	−17.6	9.3	0.05	0.25	
257	^{30}SiO, $v = 1$	8–7	336 603.002	1820.5	1	1.07	−12.6	10.7	1.03	5.27	
258	SO_2	$16_{7,9}$–$17_{6,12}$	336 669.581	245.1	1	1.34	−2.9	4.7	0.03	0.11	
259	TiO_2?	$38_{5,33}$–$38_{4,34}$	337 366.365	582.5	1	3.20	−7.4	3.6	0.02	0.06	Tentative.
260	^{34}SO	8_8–7_7	337 580.147	86.1	1	1.33	−7.0	6.8	0.05	0.33	
261	SiO, $v = 4$?	8–7	337 687.290	7047.0	1	2.13	−8.8	5.2	0.01	0.04	Tentative.
262	^{29}SiO, $v = 2$	8–7	338 245.183	3572.4	1	1.33	−10.2	20.5	0.05	0.70	
263	SO_2	$18_{4,14}$–$18_{3,15}$	338 305.993	196.8	1	1.33	−15.3	17.5	0.05	0.25	
264	SO_2	$20_{1,19}$–$19_{2,18}$	338 611.810	198.9	1	1.33	−20.2	15.8	0.11	0.98	
265	^{30}SiO	8–7	338 930.058	73.2	1	1.06	−26.8	16.4	1.15	8.44	
266	SO	3_3–2_3	339 341.459	25.5		2.12	−9.4	14.1	0.02	0.17	
267	^{34}SO	8_9–7_8	339 857.269	77.3		2.12	−6.8	11.4	0.03	0.31	
268	CN	3–2 (A)	340 033.400	32.6	1	1.06	−8.0	29.6	0.02	0.15	Hyperfine structure. Frequency chosen for peak.
269	SiO, $v = 3$	8–7	340 094.734	5329.6	1	1.06	−9.4	25.8	0.04	0.36	
270	CN	3–2 (B)	340 247.600	32.7	1	1.06	−38.5	10.1	0.03	0.29	Hyperfine structure. Frequency chosen for peak.
271	SO_2	$28_{2,26}$–$28_{1,27}$	340 316.406	391.8	1	2.11	−16.3	7.8	0.04	0.28	
272	^{29}SiO, $v = 1$	8–7	340 611.884	1831.7	1	2.11	−15.1	18.9	0.02	0.35	
273	SO	8_7–7_6	340 714.155	81.2	1	2.11	−11.9	16.8	0.46	3.86	
274	SO_2	$52_{14,38}$–$53_{13,41}$	341 321.948	1744.9	1	2.02	−6.6	−75.9	0.00	0.00	Blend.
275	SO_2	$53_{6,48}$–$52_{7,45}$	341 323.306	1411.6	1	2.02	−5.4	−74.7	0.00	0.00	Blend.
276	SO_2	$40_{4,36}$–$40_{3,37}$	341 403.068	808.4	1	2.11	−11.0	7.9	0.03	0.22	
277	SO_2	$36_{5,31}$–$36_{4,32}$	341 673.961	678.5	1	2.11	−3.3	5.1	0.03	0.15	
278	SiO, $v = 2$?	8–7	342 504.383	3593.1	1	2.01	−11.6	17.7	0.02	0.11	Tentative.
279	SO_2	$34_{3,31}$–$34_{2,32}$	342 761.625	581.9	1	2.10	−12.3	27.4	0.03	0.28	
280	^{29}SiO	8–7	342 980.847	74.1	1	2.10	−20.2	25.6	1.54	11.46	
281	SO	8_8–7_7	344 310.612	87.5	1	2.09	−19.0	13.9	0.49	4.05	
282	AlO?	9–8 (components)	344 433.400	82.7	2	2.09	−15.1	9.6	0.01	0.05	Tentative.
283	$SO^{18}O$	$14_{4,10}$–$14_{3,11}$	344 873.823	129.6	1	2.09	−17.6	15.1	0.02	0.07	

Table C.1. continued.

$N_{\rm line}$	Molecule	Transition	$\nu_{\rm lab}$ (MHz)	$E_{\rm up}/k$ (K)	Cat.	Δv	$v_{\rm min}$ (km s^{-1})	$v_{\rm max}$	Peak (K)	I (K km s^{-1})	Remarks
284	SiO, $v = 1$	8–7	344 916.332	1843.6	1	2.09	−17.3	18.5	0.05	0.69	
285	SO_2	$13_{2,12}$–$12_{1,11}$	345 338.538	93.0	1	2.08	−13.2	13.6	0.20	1.75	Blend with $H^{13}CN$.
286	$H^{13}CN$	4–3	345 339.769	41.4	1	2.08	−12.2	14.6	0.20	1.75	Blend with SO_2.
287	Im(^{13}CO)	3–2	345 410.000			2.08	−8.6	5.1	0.03	0.29	Intensity at 8% of signal intensity.
288	Im(HCN)	4–3	345 496.000			1.30	−14.6	13.2	0.04	0.23	Intensity at 7% of signal intensity.
289	CO	3–2	345 795.990	33.2	1	2.08	−22.9	14.9	3.64	41.55	
290	$SO^{17}O$	$30_{3,28}$–$31_{0,31}$	346 334.091	436.1	1	1.04	−10.7	5.8	0.03	0.12	
291	$SO^{18}O$	$13_{4,9}$–$13_{3,10}$	346 392.655	117.4	1	2.08	−13.9	8.9	0.02	0.25	
292	SO_2	$16_{4,12}$–$16_{3,13}$	346 523.878	164.5	1	2.08	−16.0	17.4	0.61	5.10	Blend with SO.
293	SO	8_9–7_8	346 528.481	78.8	1	2.08	−12.0	21.4	0.61	5.10	Blend with SO_2.
294	SO_2	$19_{1,19}$–$18_{0,18}$	346 652.169	168.1	1	2.08	−7.5	11.8	0.22	1.76	
295	SiO	8–7	347 330.581	75.0	1	2.07	−20.8	26.6	4.79	36.91	
296	SO_2	$24_{2,22}$–$23_{3,21}$	348 387.800	292.7	1	1.46	−8.8	15.3	0.06	0.44	
297	SO_2, $v_2 = 1$	$69_{9,61}$–$70_{6,64}$	349 977.759	3176.9	1	1.28	−6.9	10.6	0.07	0.22	
298	SO_2	$5_{3,3}$–$4_{2,2}$	351 257.223	35.9	1	2.05	−12.9	21.5	0.06	0.54	
299	SO_2	$14_{4,10}$–$14_{3,11}$	351 873.873	135.9	1	2.04	−6.3	23.0	0.07	0.56	
300	Im(SO)	8_8–7_7	352 689.000			2.04	−14.5	11.7	0.01	−0.11	Intensity at 8% of signal intensity.
301	Im(^{29}SiO)	8–7	354 018.000	34.0	1	2.03	−8.3	12.8	0.09	0.50	Intensity at 5 % of signal intensity.
302	u	?	354 195.000			2.03	−5.6	6.2	0.82	4.73	Unknown maser. Tentatively identified as H_2SiO.
303	HCN	4–3	354 505.477	42.5	1	2.03	−21.8	9.7	0.56	4.41	
304	SO_2	$12_{4,8}$–$12_{3,9}$	355 045.517	111.0	1	2.03	−17.6	10.6	0.05	0.31	
305	SO_2	$15_{7,9}$–$16_{6,10}$	356 040.644	230.4	1	2.02	−3.9	9.8	0.02	0.07	
306	^{34}SO	$25_{3,23}$–$25_{2,24}$	356 222.250	319.5	1	2.02	−19.3	19.9	0.01	0.08	
307	Im(SO)	8_7–7_6	356 283.000			2.02	−7.9	9.0	0.03	0.18	Intensity at 15% of signal intensity.
308	Im(SiO)	8–7	356 669.000			2.02	−7.9	25.2	0.27	1.93	Intensity at 10% of signal intensity.
309	SO_2	$10_{4,6}$–$10_{3,7}$	356 755.190	89.8	1	2.02	−29.5	8.1	0.07	0.57	
310	$^{34}SO_2$	$20_{0,20}$–$19_{1,19}$	357 102.182	184.6	1	2.01	−4.8	3.3	0.03	0.11	
311	SO_2	$13_{4,10}$–$13_{3,11}$	357 165.390	123.0	1	2.01	−10.5	9.6	0.08	0.67	
312	SO_2	$15_{4,12}$–$15_{3,13}$	357 241.193	149.7	1	2.01	−7.4	8.5	0.08	0.62	
313	SO_2	$11_{4,8}$–$11_{3,9}$	357 387.579	100.0	1	2.01	−9.1	9.6	0.08	0.72	
314	Im(SO)	8_9–7_8	357 467.000			2.01	−14.4	45.7	0.03	0.03	Intensity at 12% of signal intensity.
315	SO_2	$8_{4,4}$–$8_{3,5}$	357 581.449	72.4	1	2.01	−7.8	17.2	0.06	0.52	
316	SO_2	$9_{4,6}$–$9_{3,7}$	357 671.821	80.6	1	2.01	−15.7	15.3	0.05	0.38	
317	SO_2	$7_{4,4}$–$7_{3,5}$	357 892.442	65.0	1	2.01	−7.8	13.0	0.06	0.52	
318	SO_2	$6_{4,2}$–$6_{3,3}$	357 925.848	58.6	1	2.01	−7.4	19.3	0.05	0.42	
319	SO_2	$17_{4,14}$–$17_{3,15}$	357 962.905	180.1	1	2.01	−15.7	21.9	0.09	0.78	
320	SO_2	$5_{4,2}$–$5_{3,3}$	358 013.154	53.1	1	2.01	−7.9	13.1	0.03	0.27	
321	SO_2	$4_{4,0}$–$4_{3,1}$	358 037.887	48.5	1	2.01	−9.0	12.0	0.03	0.20	
322	Im(CO)	3–2	358 200.000			1.26	−8.9	8.8	0.31	3.28	Intensity at 1% of signal intensity.
323	SO_2	$20_{0,20}$–$19_{1,19}$	358 215.633	185.3	1	2.01	−23.4	21.6	0.31	5.14	
324	TiO_2?	$36_{4,32}$–$36_{3,33}$	358 389.868	512.8	1	3.01	−7.3	11.6	0.01	0.03	Tentative.

Table C.1. continued.

N_{line}	Molecule	Transition	ν_{lab} (MHz)	E_{up}/k (K)	Cat.	Δv	v_{min} (km s^{-1})	v_{max}	Peak (K)	I (K km s^{-1})	Remarks
325	SO_2	$25_{3,23}$–$25_{2,24}$	359 151.158	320.9	1	2.00	−8.0	24.2	0.05	0.41	
326	Im(SO)	8_8–7_7	359 690.000			2.00	−2.9	6.5	0.02	0.08	Intensity at 5% of signal intensity.
327	SO_2	$19_{4,16}$–$19_{3,17}$	359 770.685	214.3	1	2.00	−16.0	7.5	0.07	0.55	
328	SO_2	$19_{4,16}$–$19_{3,17}$	359 770.685	214.3	1	2.00	−16.0	7.5	0.07	0.55	
329	SO_2	$34_{5,29}$–$34_{4,30}$	360 290.404	612.0	1	2.00	−11.3	10.7	0.04	0.25	
330	$^{34}SO_2$	$6_{3,3}$–$5_{2,4}$	362 158.233	40.6	1	1.99	−15.0	10.8	0.02	0.21	
331	$Si^{18}O$	9–8	363 100.652	87.1	1	1.98	−15.0	10.5	0.11	0.79	
332	SO_2	$21_{4,18}$–$21_{3,19}$	363 159.262	252.1	1	1.98	−11.2	19.3	0.10	1.26	
333	SO_2	$24_{1,23}$–$24_{0,24}$	363 890.896	280.5	1	1.98	−10.9	13.9	0.05	0.39	
334	SO_2	$23_{2,22}$–$23_{1,23}$	363 925.838	259.9	1	1.98	−10.3	10.0	0.06	0.56	
335	TiO_2?	$29_{2,28}$–$29_{1,29}$	365 446.816	302.7	1	2.95	−22.9	14.2	0.01	0.11	Tentative.
336	SO_2	$15_{2,14}$–$14_{1,13}$	366 214.470	119.3	1	1.96	−8.7	7.4	0.06	0.44	
337	Im(HCN)	4–3	366 492.000			1.96	−12.1	10.3	0.22	1.70	Intensity at 41% of signal intensity.